SCUOLA NORMALE SUPERIORE

Ph. D. Thesis

Quantum information, entanglement and critical phenomena

Candidate

Gabriele De Chiara

Supervisor

Prof. Rosario Fazio

Contents

Acknowledgments

This PhD Thesis is a great opportunity for me to thank many people that helped, taught, influenced, discussed, had fun with me during these three years in Pisa.

First of all, deepest thanks to Saro Fazio, who with so many discussions and a constant scientific criticism gave a fundamental influence to my scientific career. My profound thank to Simone Montangero, who, during this years, taught me how to do physics with professionality and especially how to make excellent computer programs. It was a great pleasure to work with him. This is a good occasion to thank Massimo Palma, who since my undergraduate studies in Palermo gave me many advices and taught me a lot of physics.

My grateful thanks to Chiara Macchiavello, Vlatko Vedral and Časlav Brukner for their hospitality during my visits in Pavia, Leeds and Vienna and for many fruitful and exciting discussions.

I would like to thank Alessandro Romito who has been an elder brother since I arrived in Pisa. Thanks for all discussions, advices, trips and the good time spent together. I will miss all the every-day incursions in Matteo Rizzi and Davide Rossini's office that were fundamental for the development of the DMRG code. But we had a lot of fun too! Thanks a lot.

I would like also to acknowledge all the components of the "Quantum Transport and Information" group in Scuola Normale for the pleasant and lively atmosphere: V. Brosco, F. Caruso, R. Ferone, D. Frustaglia, V. Giovannetti, M. Governale, M. Rizzi, A. Romito, D. Rossini, J. Splettstösser, F.

Taddei

Many thanks to Federica Banfi who taught me how to prepare excellent *risotti* and many other unbelievable specialties.

I also thank G.L.G. Sleijpen for furnishing the routine JDQZ used to find the ground state in our DMRG program,
(http://www.math.ruu.nl/people/sleijpen/).

Finally there are many other people that I like to thank for different reasons: L. Amico, S. Benvenuti, D. Burgarth, P. Calabrese, F. Capurro, A. Carollo, R. Catena, R. Demkowicz-Dobrzanski, G. Falci, G. Felici, A. Ferreira, M. T. Galletto, J. J. Garcia-Ripoll, B. C. Hiesmayr, J. Kofler, G. Marandella, K. Maruyama, A. Osterloh, E. Paladino, A. Rastelli, A. Sportiello, G. Vidal, M. Wiesniak.

Un caloroso e affettuoso ringraziamento va ai miei genitori che da sempre hanno creduto in me e alle mie scelte. Grazie!

Introduction

"*Information is physical*". With this simple logo Rolf Landauer in 1961 [Lan61] gave rise to a revolution in information science. Digital computers are thermodynamic machines that dissipate energy and produce "mathematical" work [BL85]. Physicists, computer scientists and even biologists wondered wether there exists a fundamental thermodynamic limit on the efficiency of these machines. It turned out, after the reversible model of computation by Fredkin and Toffoli [FT82], that in principle a computer can work at finite velocity with zero energy dissipation and zero error. Nevertheless Landauer showed that erasing information is an intrinsic dissipative process and produces entropy.

Since the birth of digital computers, progress in technology permitted to increase the power and the memory of a calculator. This miniaturization process has been well represented in the last forty years by the Moore's law [Moo65]. Moore's law states that the number of transistors in a computer should double every 18 months. However it seems that there is a natural limit to the miniaturization of integrated circuits: a transistor is not expected to be constituted by less than one single atom! Furthermore even when transistors will be built with some hundreds of atoms the fundamental laws of physics at this nanoscopic level are inherently quantistic and will be very different from the physics of semiconductors at the macroscopic level. Based on these arguments, many people believe in the breakdown of Moore's law.

An alternative to the "classical" model of computation is represented by "quantum computation". This is a natural, and maybe necessary, extension

of classical computation when dealing with quantum systems. The first pioneering idea about the use of quantum systems for information tasks came from Richard Feynman in 1982 [Fey82]. He considered the issue of numerical simulations of quantum systems. With traditional computers, the computational resources needed (time, memory) grow in general exponentially increasing the size of the quantum system. Feynman argued that simulating quantum systems using other quantum systems could have been in principle more efficient. The *universal quantum computer*, described by David Deutsch in 1985 [Deu85], was the quantum generalization of the concept of the universal Turing machine. A quantum computer is intrinsically more powerful than its classical counterpart because of some extraordinary features like superpositions and entanglement which are peculiar of quantum mechanics.

Quantum computation could have stayed as an academic curiosity without the discovery by Peter Shor in 1994 [Sho94] of an efficient algorithm for the prime factoring problem. The best classical algorithm for solving this problem uses a time that grows exponentially with the size of the problem. The security of public key cryptographic protocols, such as RSA, is based on this difficulty (see for example [Sin00]). Thus Shor's algorithm became immediately famous and gave a thrust to the newborn quantum information theory (QIT) [NC00, Pre98, BCS04, BEZ00].

Apart from quantum computation, also quantum cryptography and quantum communication are other applications of QIT. Quantum cryptography [BB84], proposed in 1984, solves the problem of key distribution necessary for private key cryptography [GRTZ02]. The most striking example of quantum communication is quantum teleportation [BBC$^+$93] discovered in 1993. Quantum teleportation is the reconstruction over arbitrary distances of the state of a quantum system.

It is important to stress that entanglement plays a fundamental role in all these applications of quantum information: the "spooky action at distance" becomes a necessary and useful resource for exploiting the computational

power of quantum mechanics.

Besides the great interest in the development of the theoretical framework of quantum information science (the software) a lot of efforts have been devoted to the physical realization of a quantum computer (the hardware). Many systems have been proposed for the physical implementation of the "hardware" of a quantum computer: solid state systems (superconducting circuits [MSS01], nanotechnology devices based on semiconductors [Kan98]), atoms and photons in a cavity [RBH01], trapped ions [LBMW03], trapped neutral atoms [JZ05, MST$^+$04], NMR systems [VC04].

At present, only applications with few qubits, less than ten, have been realized. The main obstacle to the realization of a many-qubit quantum computer is the loss of coherence due to the interaction of the quantum system under control with the environment. This interaction destroys the quantum coherence of superpositions thus reducing the power of quantum computation. The process of decoherence [Zur91] has been long discussed and there have been many attempts to fight its destructive influence on information. For this reason studying the protection of quantum information is important for making quantum computation feasible.

Quantum information is not only applications: it is a well established theoretical framework for studying physics from a modern perspective. In this context recent interest in aspects common to quantum information and condensed matter physics [Pre00] has prompted a flourishing activity at the border of these, until few years ago, well separated disciplines. Among all the problems addressed so far we mention the recent advances in the Density Matrix Renormalization Group (DMRG) [Whi92]. A quantum information analysis of the DMRG algorithm in terms of matrix product states by Vidal [Vid04, Vid03] leaded to the development of a time dependent version of DMRG [DKSV04, WF04].

In this thesis we focus on two points: the analysis and development of methods for protecting quantum information; the study of the ground state

properties and of the evolution of critical systems by means of the DMRG algorithm.

Protecting quantum information

Methods to protect quantum information can be distinguished depending on the control being active or passive.

The best example of an active method is probably Quantum Error Correction (QEC) [Sho95, Ste96]. QEC is the quantum generalization of the classical theory of correcting codes (see for example [MS77a]). Usually a classical error correcting encoding strategy consists in copying in several bits the information stored in a single bit. This redundancy helps in correcting errors by a majority criterion. QEC uses a similar procedure but using quantum bits. It is necessary however that the noise effect is low enough for this protocol to be efficient. By means of fault tolerant quantum computation [Sho96] it is also possible to set a threshold for the level of noise below which the computation is sufficiently protected. The *threshold theorem* states that if noise is below a certain constant then it is possible to reliably perform an arbitrary long quantum computation using QEC. This statement implies that small errors do not accumulate during the computation. Other examples of active control on decoherence consist in the repeated application of quantum operations on the qubits. Quantum Zeno effect [MS77b] can be exploited to preserve the state of a qubit over time. This is achieved measuring many times the qubit thus preventing it to decay. Recently this concept has been generalized also for computation with quantum Zeno subspaces [FP02]. Bang-bang methods [VL02] have been borrowed from NMR and adapted for defeating decoherence.

In the framework of QEC we consider in chapter 2 the evolution of a quantum memory, i.e. a register of qubits, protected by a QEC procedure interacting with a spatial correlated bosonic bath. This particular environ-

ment, inducing an effective interaction between the qubits, is capable of creating entanglement between them [Bra02]. As usual in QEC protocols one repeatedly measures and corrects the state of the qubits. While in certain conditions QEC protects the quantum information stored in the register, in others the protocol fails to protect information and the qubits can become entangled. We show that the entanglement creation rate can be amplified using QEC comparing to the case in which no such protocol is used.

There are also "static" methods in which the computation takes place in a subspace of the Hilbert space not affected by decoherence. The existence of decoherence free subspace [ZR97] is guaranteed by symmetry properties of the environment. When dealing with solid state implementation of a quantum computer, the issue of actively controlling interactions between different qubits arises. Although it is possible to apply active control schemes to solid state qubits it would be desirable to avoid external control. Active control indeed means that the system under consideration is coupled through external gates to the environment thus leading to the loss of coherence. This requirement can be addressed using a spin network, i.e. an array of spins, with time independent couplings. The desired protocol is achieved through the free time evolution of the network and so any external control on the system is unnecessary. As a consequence the system is more efficiently isolated from the environment. Recently the possibility to implement quantum communication protocols in spin networks has been put forward (see for example [Bos03]). In this proposal the network is a simple 1D Heisenberg spin chain. This quantum channel allows to transmit a quantum state with high fidelity. Later Christandl et al. [CDEL04] show how to achieve perfect state transfer using a modulated linear chain or more complicated graphs. When implementing this protocol in solid state systems its perfect quality is degraded by static disorder in the parameters of the system. We thus make a careful analysis in chapter 3 of the robustness of the protocol in the presence of static imperfections. We also find that the output signal of the channel in time shows a transition from a periodic to a fractal behavior when increasing

the strength of disorder. It is possible to connect the performance of the protocol with quantum chaos through the analysis of the level spacing statistics of the disordered Hamiltonian.

We also use this idea of using spin networks for implementing quantum cloning (chapter 4). Quantum cloning consists in the imperfect copy of an unknown quantum state. Wootters and Zurek [WZ82] showed that perfect quantum cloning is forbidden by the laws of quantum mechanics. It is however interesting to consider bounds on imperfect quantum cloning because of its connection with quantum state estimation and the security of quantum cryptography. Using a spin star network, we find that phase covariant cloning (PCC), in which input states are restricted to the equator of Bloch sphere, can be realized with fidelities comparable to the optimal bound. Furthermore for the $1 \rightarrow 2$ PCC, that produces two copies of a single input state, our protocol saturates the optimal bound. We provide a careful analysis of noise influence in this system and compared it with the case of quantum gates. For the model of environment considered our method outperforms the quantum gates method. We study also the effect of static disorder in the system.

Quantum spin networks, and in particular spin chains represent useful tools for QIT. However it turns out they are more than that. It is well known fact that there exists entanglement in the ground state of spin chains described by common models (Heisenberg, XY). In chapter 7 we make a proposal to extract this entanglement by scattering probe particles off the spin chain. The entanglement extracted can then be used as a resource for QIT. We discuss several cases (bipartite, multipartite entanglement), we make a quantitative analysis of the phenomenon and we also propose a scheme to simulate the process using optical lattices.

Yet another example of strategy to protect information in quantum computation is to use the adiabatic geometric phase (Berry's phase [Ber84]) instead of the "traditional" dynamic phase. Berry's phase arises during the evolu-

tion of a quantum system whose Hamiltonian is adiabatically changed in a periodic fashion changing a set of parameters. If the state of the system is prepared in an eigenstate of the initial Hamiltonian then after a period the final state differs from the initial one only for a phase factor. This phase contains the dynamical phase, proportional to the time integral of the energy eigenvalue, and a geometrical phase that depends on the loop traversed by the parameters of the Hamiltonian. The use of geometric adiabatic phase seems to lead to noise tolerant quantum computation because of its intrinsically geometrical and adiabatical features. It is thus relevant to analyze the behavior of Berry's phase under the effect of environmental noise. This analysis has been already carried out in various contexts such as classical noise [DCP03], quantum noise with quantum jumps [CFGSV02] and the master equation approach [WG03]. In chapter 5 we approach this problem using the Langevin equations for qubit operators. We analyze the effect of adiabatical evolution on decay rates and energy shifts. This approach appears to be particularly transparent and the results are amenable of a geometrical interpretation.

Critical systems

Critical behavior is widespread in physics ranging from low to high energy physics. In this Thesis we are interested in quantum phase transitions (QPT) [Sac99]. The transition, occurring at zero temperature, takes place by changing a parameter of the system Hamiltonian. Close to a QPT correlation functions diverge showing a universal scaling behavior. The term "universal" refers to the fact that the properties of the system depend only on its dimensionality and on the symmetry broken in the ordered phase. Different systems with the same critical exponents are said to belong to the same class of universality.

In chapter 6 we study the phase diagram of the 1D spin-1 Bose-Hubbard model. This consists of a 1D array of potential wells containing spin-1 bosonic atoms. These are allowed to hop from one site to a neighboring site. Atoms

on the same site interact with a contact potential and with an antiferromagnetic interaction. In the plane $t - \mu$, t being the hopping amplitude and μ being the chemical potential, this system exhibits a rich phase diagram made of lobes inside which the system is a Mott insulator and outside is a superfluid. Until now, due to difficulty in the analytical calculations involved, a detailed characterization of the phase diagram has been lacking.

We address these problems by means of intensive numerical simulation. To this end during my PhD I developed a time dependent density matrix renormalization group (t-DMRG) code.

From the quantum information perspective, it is important to study how entanglement behave close to a QPT and especially for a critical system. In critical spin chain models it was found [HLW94] that the entanglement, measured by the Von Neumann entropy, of a block of spins with the rest of the chain diverges logarithmically with the size of the block. The prefactor is proportional to the "central charge" of the underlying conformal field theory (CFT). This has been confirmed for analytically solvable systems (Ising, XY see for example [VLRK03, JK04, CC04]). For other models, such as the Heisenberg or the more general critical XXZ, this has been confirmed only for very small chains [LRV04]. We thus use in chapter 8 the DMRG algorithm to calculate the von Neumann entropy as function of the length for chains up to 10^3 sites long. We also consider the case of disordered spin chains. In this case we confirm the prediction that the effective central charge is reduced by a factor $\ln 2$ with respect to the case without disorder. In chapter 8 we also study the evolution of a XXZ spin chain after a quench of the anisotropy from a non-critical to a critical value. The result, anticipated for the Ising model in [CC05], is that the entanglement grows linearly in time until a saturation value is reached. As for the ground state entanglement we consider the effect of coupling disorder in the evolution. In this case the behavior of entanglement is completely different: it grows very slowly in time, as a logarithmic function. Since analytically results for the XXZ model are very demanding, we use the extension to the DMRG algorithm for the time

evolution of long chains [WF04, Vid04].

In Appendix B we review the DMRG algorithm and its extension to t-DMRG for the evolution of quantum systems.

In chapter 1 we give a brief introduction to Quantum Information theory highlighting the aspects we consider in this Thesis.

Publications

- Regular Articles

1. G. De Chiara, S. Montangero, P. Calabrese and R. Fazio:
   Entanglement Entropy dynamics in Heisenberg chains
   J. Stat. Mech.: Theor. Exp. (2006) P03001.
2. M. Rizzi, D. Rossini, G. De Chiara, S. Montangero and R. Fazio:
   Phase diagram of spin-1 bosons on one-dimensional lattices
   Phys. Rev. Lett. **95**, 240404 (2005).
3. G. De Chiara, D. Rossini, S. Montangero, and R. Fazio:
   From perfect to fractal transmission in spin chains.
   Phys. Rev. A **72**, 012323 (2005).
4. G. De Chiara, R. Fazio, C. Macchiavello, S. Montangero
   and G. M. Palma:
   Cloning transformations in spin networks without external control
   Phys. Rev. A **72**, 012328 (2005).
5. G. De Chiara, R. Fazio, C. Macchiavello, S. Montangero and G. M. Palma
   Quantum cloning in spin networks,
   Phys. Rev. A **70**, 062308 (2004).
6. G. De Chiara, R. Fazio, C. Macchiavello and G. M. Palma
   Entanglement production by quantum error correction in the presence of correlated environment,
   Europhys. Lett. **67**, 714 (2004).

7. G. De Chiara and G. M. Palma
   Berry phase for a spin 1/2 particle in a classical fluctuating field,
   Phys. Rev. Lett. **91**, 090404 (2003).

- Preprints

8. G. De Chiara, A. Łoziński and G. M. Palma:
   Berry phase in open quantum systems: a quantum Langevin equation approach
   Eprint: quant-ph/0410183.
9. G. De Chiara, C. Brukner, R. Fazio, G. M. Palma and V. Vedral:
   A scheme for entanglement extraction from a solid
   Eprint: quant-ph/0505107.
10. G. De Chiara, M. Rizzi, D. Rossini and S. Montangero:
    Density Matrix Renormalization Group for dummies
    Eprint: cond-mat/0603842

- Referred Conference Proceedings

11. M. Rizzi, D. Rossini, G. De Chiara, S. Montangero and R. Fazio:
    Phase diagram of spin-1 bosons on one-dimensional lattices
    J. Phys. B (in press).
12. G. De Chiara, R. Fazio, C. Macchiavello, S. Montangero and G. M. Palma
    Cloning transformations in spin networks without external control
    Int. J. of Quant. Inf. (in press)
13. A. Romito, G. De Chiara, D. Rossini, S.Montangero:
    Implementation of quantum communication protocols in Josephson junction arrays .
    Int. J. of Quant. Inf. (in press)
14. G. De Chiara, R. Fazio, C. Macchiavello and G. M. Palma:
    Quantum error correction driven entanglement dynamics in the

presence of correlated noise,
Int. J. Quant. Inf.

Chapter 1

Quantum Information Theory

Since most of this Thesis is about quantum information theory (QIT) we provide a short introduction to the main concepts of quantum information used in the Thesis. For introductions on this topics we refer to the textbooks [NC00, Pre98, BCS04, BEZ00]. We will start in Sec. 1.1 from the basic concepts, the qubit, quantum gates; then in Sec. 1.2 we will talk about entanglement and how to measure it. Finally in Sec. 1.3 we review the concept of geometric quantum computation based on the Berry phase.

1.1 Basics of quantum computing

Let us start by defining the basic element of quantum information and computation: the *qubit*. It is a two level system (the name was coined by B. Shumacher). A qubit is the quantum generalization of the bit, the unit of information in the classical information theory. To represent the state of a qubit there are various ways. Each state of a qubit can be written as a superoposition of the two computational states $|0\rangle$ and $|1\rangle$:

$$|\psi\rangle = \alpha|0\rangle + \beta|1\rangle; \tag{1.1}$$

where the complex numbers α and β satisfies $|\alpha|^2 + |\beta|^2 = 1$.

Since a qubit is isomorphic to a spin 1/2 particle we can define a very

useful representation that helps to visualize the qubit state. Let us define two polar angles ϑ and φ such that:

$$\alpha = \cos\frac{\vartheta}{2} \tag{1.2}$$

$$\beta = e^{i\varphi}\sin\frac{\vartheta}{2} \tag{1.3}$$

then state (1.1) can be represented as a unit vector, called Bloch vector, with polar angle $(\vartheta;\varphi)$.

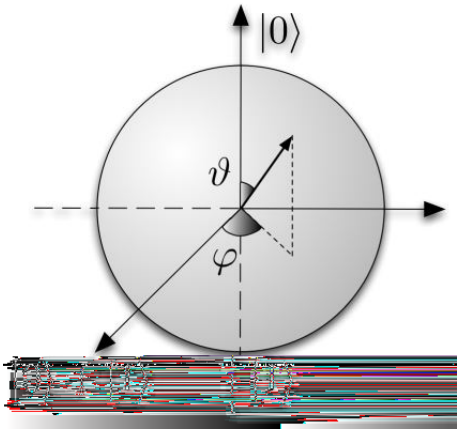

Figure 1.1: The Bloch sphere representation of a quantum state. The vector represented is the Bloch vector with polar angles $(\vartheta;\varphi)$.

This representation is extremely useful when dealing with mixed states. In this case, given the density matrix of a qubit ρ the Bloch vector $\vec{P}$ has components:

$$P_x = \langle\sigma_x\rangle_\rho = \mathrm{Tr}\rho\sigma_x \tag{1.4}$$

$$P_y = \langle\sigma_y\rangle_\rho = \mathrm{Tr}\rho\sigma_y \tag{1.5}$$

$$P_z = \langle\sigma_z\rangle_\rho = \mathrm{Tr}\rho\sigma_z \tag{1.6}$$

and ρ can be rewritten as:

$$\rho = \frac{1}{2}\left(\mathbb{1} + \vec{P}\cdot\vec{\sigma}\right) \tag{1.7}$$

The length of the Bloch vector gives information on the "purity" of the state: if $|\vec{P}| = 1$ the state is pure while for $0 \leq |\vec{P}| < 1$ the state is mixed.

We have seen how to represent the state of a qubit. Now we consider the basic operations on one or more qubits. Let us start with one-qubit quantum gates, i.e. unitary operations acting on one qubit. The simplest example is the NOT gate which flips the state of the qubit. This is equivalent to the Pauli matrix σ_x:

$$\sigma_x|0\rangle = |1\rangle \tag{1.8}$$

$$\sigma_x|1\rangle = |0\rangle \tag{1.9}$$

When dealing with quantum circuits it is useful to consider a graphical representation of the circuit analogously to classical circuits: a qubit is represented by a wire and a one-qubit gate by a box with a label representing the corresponding operation. In Fig. 1.2a. it is shown a NOT gate.

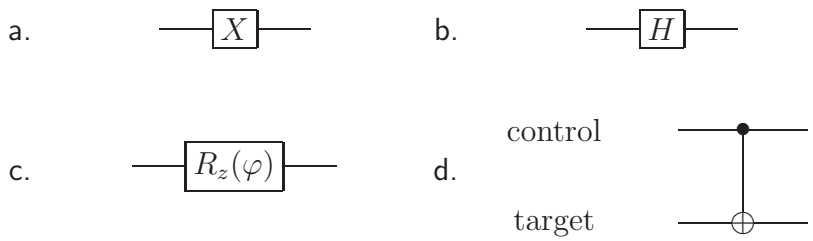

Figure 1.2: Examples of circuit representation: a. NOT gate; b. Hadamard gate; c. Phase gate $R_z(\varphi) = e^{i\sigma_z\varphi/2}$; d. $CNOT$ gate.

Notice that the quantum NOT is the generalization of the classical gate NOT. Quantum mechanics however allows gates without any classical counterpart. Consider, for example, the so-called square root of NOT, that create a superposition of the computational states:

$$\sqrt{NOT} = \frac{1}{\sqrt{2}} \begin{pmatrix} 1 & 1 \\ 1 & -1 \end{pmatrix} \tag{1.10}$$

This is also known as the Hadamard gate which is very useful in quantum algorithms and its representation is given in Fig. 1.2b. Another one-qubit gate that has no classical counterpart is the phase gate $R_z(\varphi) = e^{i\sigma_z\varphi/2}$ (see Fig. 1.2c.) which introduces a phase difference φ between the computational states. Notice that $R_z(\varphi)$ is a rotation of the state vector of an angle φ around the z axis in the Bloch representation. In the same way we can define rotation around the other two axis x and y: $R_x(\varphi) = e^{i\sigma_x\varphi/2}$ and $R_y(\varphi) = e^{i\sigma_y\varphi/2}$. A generic one-qubit transformation can be decomposed in product of rotations around only two non-parallel axis (see for example [NC00]).

Among the two-qubits gates, one important example is the controlled-NOT operation ($CNOT$). The circuit representation is shown in Fig. 1.2d. Of the two input qubits, the top one, is the control and the second is the target. The result of the gate is to apply a NOT operation to the target when the control is in state $|1\rangle$ and to apply the identity when the control is in state $|0\rangle$. In a matrix representation this is:

$$CNOT = \begin{pmatrix} 1 & 0 & 0 & 0 \\ 0 & 1 & 0 & 0 \\ 0 & 0 & 0 & 1 \\ 0 & 0 & 1 & 0 \end{pmatrix} \tag{1.11}$$

Notice that in the computational basis this transformation recalls the truth table of an XOR classical gate. Do not forget however that a quantum operation can be applied also to superpositions. For example let us apply the $CNOT$ gate to the control in the (non-normalized) state $|0\rangle + |1\rangle$ and the target in the state $|0\rangle$. The result is an entangled state $|00\rangle + |11\rangle$. One can imagine also other controlled operations, and in principle we can construct a controlled-U operation where U is a one-qubit gate.

The controlled operations do not exhaust the set of possible two-qubit gates. In principle one can consider also three-qubit or n-qubit gates. It turns however out that these operations can be reduced to single and two-qubit gates due to a theorem demonstrated by Barenco *et al.* [BBC$^+$95].

Any quantum operation on n qubits can be approximated with arbitrary precision using a quantum circuits containing only single qubit gates and $CNOT$s. Thus the set of all one-qubit gate plus $CNOT$ form a universal set of quantum gates. It is not necessary however to use the $CNOT$ operation since we can substitute it with another "non trivial" two-qubit operation, i.e. this transformation must be capable of creating entanglement between two qubits.

Until now we have discussed on qubits and quantum gates that form the "software" of a quantum computer. Another important research area in quantum information is to find the proper "hardware" of a quantum computer. A quantum system, to be successfully used for the implementation of a quantum computer, should fulfill the so called DiVincenzo's requirements for quantum computing [DiV97, DiV00]:

1. A scalable physical system with an array of well defined qubits
2. The ability to initialize the system in a simple reference state (for example $|00\ldots0\rangle$)
3. The ability to implement a set of universal gates
4. Long decoherence times, compared to the typical gate times
5. The ability to measure the output qubits

In the first part of the Thesis we address the fourth requirement, finding and analyzing new ways of increasing the decoherence times. For example we considered quantum error correction in chapter 2, the use of spin networks in chapters 4 and 3, and the use of geometrical phase in chpater 5.

1.2 Entanglement and how to measure it

Quantum entanglement is one of the central topic of this Thesis (for a more comprehensive tutorial see [Bru02]) and therefore we briefly recall the main

properties of entangled states. Let us start defining what is an entangled state. Suppose we have two quantum systems A and B whose Hilbert spaces are denoted by $\mathcal{H}_A$ and $\mathcal{H}_B$ respectively. A state of the two systems $|\Psi_{AB}\rangle \in \mathcal{H}_A \otimes \mathcal{H}_B$ is entangled if it cannot be written as a product state:

$$|\Psi_{AB}\rangle \neq |\psi_A\rangle \otimes |\psi_B\rangle. \tag{1.12}$$

If such a product state decomposition exists the state is said to be separable. Examples of entangled states for two qubits are the four Bell states:

$$|\psi^{\pm}\rangle = \frac{1}{\sqrt{2}}\left(|01\rangle \pm |10\rangle\right) \tag{1.13}$$

$$|\phi^{\pm}\rangle = \frac{1}{\sqrt{2}}\left(|00\rangle \pm |11\rangle\right) \tag{1.14}$$

A simple property of a pure entangled state is that subsystems A and B taken alone are in a mixed state. For example if we calculate the reduced density matrix of subsystem A or B for one of the Bell states we obtain a maximally mixed state for the qubit:

$$\rho_{A\,(B)} = \mathrm{Tr}_{B\,(A)}|\psi^+\rangle\langle\psi^+| = \frac{1}{2}\begin{pmatrix} 1 & 0 \\ 0 & 1 \end{pmatrix} = \frac{1}{2}\mathbb{1} \tag{1.15}$$

From this example it is clear that the more two systems are entangled the more the reduce density matrix of one or the other subsystem is mixed. Using this argument we can define a measure of bipartite entanglement for a pure state called the entanglement entropy:

$$E(|\Psi_{AB}\rangle) = S(\rho_A) = -\mathrm{Tr}_A\left(\rho_A \log_2 \rho_A\right) \tag{1.16}$$

where $S(\rho)$ is the Von Neumann entropy that is the analogue of the Shannon entropy in classical information theory. Notice that throughout this Thesis we take the logarithm in the entropy to be in base 2 so that entropy and entanglement are measured in *bits*. From Eq. (1.16) it is simple to show that each of the Bell states have entanglement $E = 1$ which is the maximum achievable for two qubits. For this reason Bell states are called maximal entangled states for two qubits.

The Von Neumann entropy is a very useful tool for measuring the entanglement by no means restricted to qubits but to every system whose global state is pure. It is well suited for example for measuring entanglement of many body systems at zero temperature.

If the global state of systems A and B is not pure the definition of an entangled state is slightly modified. Let us call ϱ_{AB} the global density matrix of system A and B. Then ϱ_{AB} is entangled if it cannot be written as a mixture of product states:

$$\varrho_{AB} \neq \sum_i p_i |\psi_A^i\rangle\langle\psi_A^i| \otimes |\psi_B^i\rangle\langle\psi_B^i| \tag{1.17}$$

where p_i form a set of probabilities. Given a density matrix ϱ it is a very hard to determine if it is entangled or not. While for pure states the mixedness of the reduced density matrix is a necessary and sufficient condition for entanglement, for mixed state it is not. Though there are some operational separability criteria that allows one to recognize if a state is separable, these are only sufficient conditions.

For very special cases, one among all the case of two qubits, there are operational necessary and sufficient separability criteria. One example of these criteria is the positive partial transpose, also known as the Peres-Horodecki criterion [Per96,HHH96]: in order to check whether or not a density matrix ϱ is entangled one has to calculate its partial transposition with respect to one of the two subsystems A or B. So if the expression of ϱ in the computational basis is:

$$\varrho = \sum_{\alpha,\beta,\alpha',\beta'=0,1} \varrho_{\alpha\beta,\alpha'\beta'} |\alpha\beta\rangle|\alpha'\beta'\rangle \tag{1.18}$$

then the partial transposition of ϱ with respect to A is:

$$\varrho^{T_A} = \sum_{\alpha,\beta,\alpha',\beta'=0,1} \varrho_{\alpha'\beta,\alpha\beta'} |\alpha\beta\rangle|\alpha'\beta'\rangle \tag{1.19}$$

The criterion states that if ϱ is separable then ϱ^{T_A} is semipositive (all its eigenvalues are not negative) and the converse is true ony for qubits and for a qubit and a three level system (a qutrit).

In order to measure the entanglement of a mixed state of two qubits, one can use the (so-called) concurrence [HW97, Woo98]. For a density matrix of two qubits ϱ let us define $\tilde{\varrho} \doteq \sigma_y \otimes \sigma_y \rho^* \sigma_y \otimes \sigma_y$ and $R = \varrho\tilde{\varrho}$. Concurrence is defined as $C = \max\{0, \lambda_1 - \lambda_2 - \lambda_3 - \lambda_4\}$ where λ_i are the square roots of the eigenvalues of R labeled in decreasing order. To get the entanglement in bits from the value of concurrence there is a simple one-to-one non-decreasing function:

$$E = h(\frac{1+\sqrt{1-C^2}}{2}); \quad \text{where} \tag{1.20}$$

$$h(x) = -x\log_2 x - (1-x)\log_2(1-x). \tag{1.21}$$

As the entanglement is a monotonic function of concurrence, we will always consider concurrence to measure the entanglement between two qubits throughout the Thesis.

Until now we considered whether the state of a bipartite system is entangled or not. It is natural to ask if there exists other forms of entanglement. In other words, in the case of a tripartite system, is the entanglement between two of the three parties the more general form of entanglement or is there a *genuine tripartite entanglement*? Let us consider the GHZ (after Greenberger-Horne-Zeilinger [GHZ89]) for three qubits:

$$|GHZ\rangle = \frac{1}{\sqrt{2}}\left(|000\rangle + |111\rangle\right) \tag{1.22}$$

This state is not separable, as it cannot be written as the product of three wave functions, one for each qubits. It is also not biseparable, i.e. the product of one qubit wave function times a two qubit entangled state. This example shows that there exists genuine tripartite entanglement. If we trace out anyone of the three qubits we obtain the reduced density matrix of two qubits: $\rho = 1/2(|00\rangle\langle 00| + |11\rangle\langle 11|)$ which is separable, being the convex sum of separable states. The GHZ is indeed very fragile under particle losses. Another example of a state which is not either separable neither biseparable is the W state:

$$|W\rangle = \frac{1}{\sqrt{3}}\left(|001\rangle + |010\rangle + |100\rangle\right) \tag{1.23}$$

Differently from the GHZ state, this state contains some bipartite entanglement: after tracing out one qubit the reduced density matrix of the other two qubits is entangled.

It is possible to classify states of three qubits that contains genuine multipartite entanglement, according to their GHZ or W type entanglement. It has been indeed demonstrated that if a state $|\psi\rangle$ can be reduced to $|W\rangle$ with stochastic local operations and classical communication (SLOCC) and $|\phi\rangle$ can be reduced to $|GHZ\rangle$ with SLOCC then it is impossible to convert $|\psi\rangle$ in $|\phi\rangle$ and viceversa [DVC00]. Moreover we cannot obtain a $|W\rangle$ state from a $|GHZ\rangle$ using LOCC. The inequivalence of this two classes of states allow one to classify genuine multipartite states. To detect if a state is tripartite entangled we can use the notion of entanglement witness [HHH96]. A GHZ witness $\mathcal{W}_{GHZ}$ is an Hermitian operator with $\mathrm{Tr}(\mathcal{W}_{GHZ}\rho) < 0$ where ρ is some GHZ state, and $\mathrm{Tr}(\mathcal{W}_{GHZ}\rho_W) \geq 0$ for all ρ_W in the set of W states. An example for a GHZ witness is given by [Bru02]:

$$\mathcal{W}_{GHZ} = \frac{3}{4}\mathbb{1} - |GHZ\rangle\langle GHZ| \tag{1.24}$$

Analogously one can define a W witness which detects W states but has a non negative expectation value on separable and biseparable states. An example is given by the following operator:

$$\mathcal{W}_W = \frac{2}{3}\mathbb{1} - |W\rangle\langle W| \tag{1.25}$$

From these considerations it is clear that the notion of an entanglement measure is ambiguous since we can measure the distance of a state from either W or GHZ states. In addition the number of inequivalent classes of entangled states grows when the number of particles is larger than three [DVC00].

1.3 Geometric quantum computation

Berry's phase arises when a quantum system is subject to a slowly periodic changing Hamiltonian [Ber84]. Suppose that a quantum system is initially

in the nth eigenstate of the Hamiltonian at time $t = 0$ $|\psi(0)\rangle = |u_n(0)\rangle$. The Hamiltonian $H(\vec{R}(t))$ depends on time through its dependence on a set of parameters $\vec{R}$. If we change the set of parameters in an adiabatic fashion, then by virtue of the adiabatic theorem [Mes61] the state of the system at time t is parallel to the instantaneous corresponding eigenstate $|u_n(t)\rangle$ with eigenenergy $E_n(t)$. If at time T the parameters return to their initially configuration then the state of the system will return to its initial state $|\psi(T)\rangle = e^{i\delta_n} e^{i\gamma_n} |\psi(0))\rangle$ apart from a phase factor. Berry [Ber84] showed that the phase factor is made of two contributions: the dynamical phase[1]

$$\delta_n = \int_0^T E_n(t) dt \tag{1.26}$$

and the geometric phase

$$\gamma_n = i \int_0^T \langle u_n(\vec{R}) | \nabla_{\vec{R}} | u_n(\vec{R}) \rangle \cdot \frac{d\vec{R}}{dt} dt \tag{1.27}$$

where the integrand

$$\vec{A}_n = i \langle u_n(\vec{R}) | \nabla_{\vec{R}} | u_n(\vec{R}) \rangle \tag{1.28}$$

is called Berry connection and it is analogous to the vector potential in electromagnetism. The dynamic and geometric phases have many differences: δ depends on the energy eigenvalue and on T; instead γ is independent of this quantities and depends on the energy eigenstates and on the path traversed by the set of parameters.

Let us consider as an example a spin one half in an external magnetic field pointing in the direction $\hat{n}$ of polar angles (ϑ, φ). The Hamiltonian is

$$H = \frac{1}{2} |B| \hat{n} \cdot \vec{\sigma} \tag{1.29}$$

The eigenstates of H are the spin states pointing parallel and antiparallel to $\hat{n}$: $|\uparrow_{\hat{n}}\rangle$ and $|\downarrow_{\hat{n}}\rangle$.

The connection has only the φ component:

$$A_\varphi^\uparrow = -A_\varphi^\downarrow = i \langle \uparrow_{\hat{n}} | \frac{\partial}{\partial \varphi} | \uparrow_{\hat{n}} \rangle = \frac{1}{2} \cos\vartheta. \tag{1.30}$$

[1] Here and for the rest of the Thesis we set $\hbar = 1$.

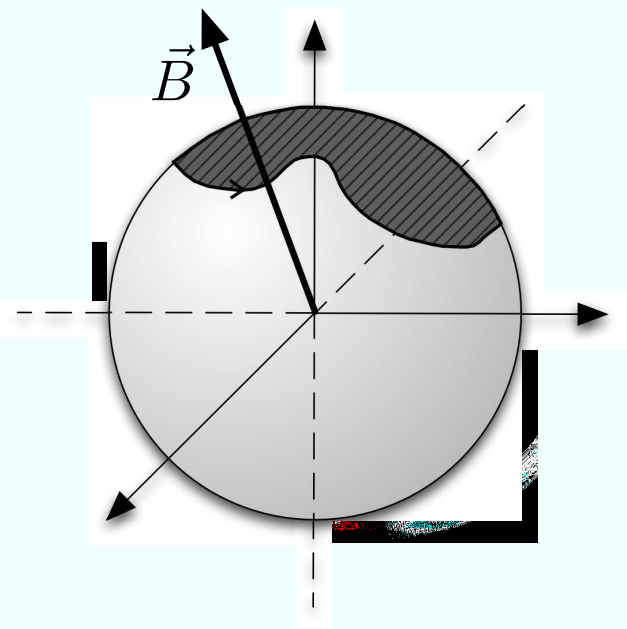

Figure 1.3: The magnetic field $\vec{B}$ adiabatically traverses the loop across the Bloch sphere. The Berry phase is proportional to the shadowed region enclosed by the loop.

The accumulated Berry phase for a simple conic path $\hat{n}(t) \equiv (\vartheta, 2\pi t/T)$ is given by $\gamma^{\uparrow(\downarrow)} = \pm\pi \cos\vartheta$. For a generic path the Berry phase is proportional to the solid angle subtended by the path on the Bloch sphere (see Fig. 1.3).

Apart from the general importance of Berry phase in quantum mechanics, it has been proposed [JVEC00,ZR97,FFP$^+$00,FSF03,DCZ01,EEH$^+$00] to use the geometric phase to generate quantum gates. A simple one-qubit phase gate can be obtained with a slow precession of the parameters as discussed above and, after spin-flip, effectuating the same path backward. This spin-echo protocol allows one to remove the dynamical phase while doubling the geometric phase. A controlled phase gate between two spins one half can be realized by coupling the magnetic moments of the two spins. Let us assume that the total Hamiltonian is:

$$H = \vec{B}_1 \cdot \vec{\sigma}_1 + \vec{B}_2 \cdot \vec{\sigma}_2 + J\vec{\sigma}_1 \cdot \vec{\sigma}_2 \tag{1.31}$$

Now suppose that B_1 and B_2 are varied in a slowly periodic way as in the case

with one qubit. The effective field experienced by spin 2 is $\vec{B}_{eff} = \vec{B}_2 + J\vec{\sigma}_1$ so it depends on the state of spin 1. The Berry phase accumulated by spin 2 is thus dependent on spin 1. Obviously this picture is symmetric in the two spins so we can write an effective transformation for the two spins:

$$U = \begin{pmatrix} e^{i\gamma^{\uparrow}} & 0 & 0 & 0 \\ 0 & e^{-i\gamma^{\uparrow}} & 0 & 0 \\ 0 & 0 & e^{i\gamma^{\downarrow}} & 0 \\ 0 & 0 & 0 & e^{-i\gamma^{\downarrow}} \end{pmatrix} \tag{1.32}$$

Notice that this controlled phase gate can be used instead of the $CNOT$ to form a set of universal gates.

Chapter 2

Entanglement production by quantum error correction in the presence of correlated environment

Quantum error correction (QEC) [Sho95, Ste96] is used to perform quantum information processing in the presence of small errors. These arise for example when the qubits interact with the external environment. When QEC was proposed, the theory of classical correction schemes [MS77a] was already established. The simplest example is the repetition code in which every logical bit is encoded in many physical bits:

$$0 \to \tilde{0} \equiv 00\ldots0 \tag{2.1}$$

$$1 \to \tilde{1} \equiv 11\ldots1 \tag{2.2}$$

Each time an error occurs it can be recognized by a majority criterion and corrected. In this way if the encoding consists of $2k+1$ physical bits then k errors can be exactly corrected at most. If the probability of bit flip is p then the probability of k errors is p^k and for small p the probability of having more than k errors is exponentially small. Shor [Sho95] showed that also QEC is possible and invented a quantum code for this purpose. Let us consider the 3-qubit repetition code that allows one to correct one bit flip, i.e. $|0\rangle \to |1\rangle$

and $|1\rangle \rightarrow |0\rangle$. The encoding transformation is:

$$|\tilde{0}\rangle \rightarrow |000\rangle \tag{2.3a}$$

$$|\tilde{1}\rangle \rightarrow |111\rangle \tag{2.3b}$$

To see how the protocol works let us consider a superposition of the encoded states and suppose that an error occurred in the first qubit:

$$a|\tilde{0}\rangle + b|\tilde{1}\rangle = a|000\rangle + b|111\rangle \rightarrow a|100\rangle + b|011\rangle \tag{2.4}$$

Now the crucial idea behind QEC is to reveal the error, without measuring each single qubit separately. This is achieved by performing collective measurements on two qubits and thus preserving the quantum superposition. In the specific case of a state $|xyz\rangle$ one has to measure $x \oplus y$ and $y \oplus z$ where $\oplus$ denotes addition modulo 2. Alternatively one can measure $\sigma_z^1\sigma_z^2$ and $\sigma_z^2\sigma_z^3$. After the measurement one finds two classical bits that form the syndrome $(x \oplus y, y \oplus z)$. The syndrome indicates if an error has occurred and where. Thus it can be corrected rotating the corresponding qubit. Notice that during this procedure no information is gained about the coefficients a and b so the superposition is left unchanged. In the example considered the syndrome is $(1, 0)$ indicating that the first qubit has been flipped.

Shor's code can be used to correct also phase errors, i.e. $|0\rangle \rightarrow |0\rangle$ and $|1\rangle \rightarrow -|1\rangle$. The procedure consists in encoding in a different basis:

$$|\tilde{0}\rangle \rightarrow |000\rangle_x \tag{2.5a}$$

$$|\tilde{1}\rangle \rightarrow |111\rangle_x \tag{2.5b}$$

where $|0\rangle_x = 2^{-1/2}(|0\rangle + |1\rangle)$ and $|1\rangle_x = 2^{-1/2}(|0\rangle - |1\rangle)$ are eigenstates of σ_x. A phase flip in the $|0\rangle, |1\rangle$ basis is equivalent to a bit flip in the $|0\rangle_x, |1\rangle_x$. Remarkably Shor's code can be used also to correct the combination of the two errors using two stages of the encoding procedure in the two different basis.

QEC have been developed to deal with independent errors on individual physical qubits due to the interaction of each physical qubit with its own

reservoir. In several physical situations however the presence of correlated reservoirs [PSE96] can result in non-trivial effects. For example it has been shown that the interaction of two subsystems with a finite temperature common bath of harmonic oscillators can, for short times, induce entanglement between the two subsystems initially in a product state. This is possible when the environment has some spatial correlations [Bra02], as often occurs in solid state physics, leading to an effective interaction between the two subsystems. This effect is also present for noisy baths in the Markovian regime [BFP03]. The dynamics of the entanglement rate in the presence of decoherence was also studied [YCW03].

In [Bra02] the model of two qubits interacting with a common boson bath is studied. In certain conditions the environment can induce a mediated interaction between the qubits even if they are not directly interacting with each other. The evolution operator of the two qubits system alone, after tracing out the environment degrees of freedom, results in a *CP-map* that contains two terms. The first destroys the coherences and comes from averaging the random phases induced by the environment. The second term, which is not trivial only when the environment is spatially correlated, induces a renormalization of the qubits energy. It is this coherent term responsible for an effective interaction between the qubits leading to the creation of entanglement. This is possible only if the effective coupling between the qubits is larger than the typical dephasing rate.

QEC in the presence of correlated environments is analyzed in Ref. [AF03]. The authors deal specifically with a quantum memory for which the task is to preserve the state of the qubit under the influence of external noise. They derive a quasi-continuos equation for the dissipative evolution of a single qubit in the presence of QEC. This is done under the assumption of short delay between two corrections. They also proposed a possible implementation of the scheme using superconducting qubits [MSS01].

In this chapter we address the issue of the effects of QEC on the entan-

glement between *logical* qubits in the presence of a correlated environment. It is reasonable to expect that the entanglement induced by the correlated bath between physical qubits will modify the encoded state and therefore corrected by the QEC procedure as if it were an error. However, when such entanglement becomes sufficiently large the protocol may not be able to correct it. It is therefore interesting to study how entanglement is modified by the application of QEC. In the following we will show that, although QEC is unable to correct such errors, it can enhance the generation of entanglement in a pair of *logical* qubits with respect to the entanglement induced by the environment on a pair of *physical* qubits.

2.1 Evolution without QEC

The model we consider in this chapter, the same as in [PSE96], consists of a register of quantum bits interacting with a common environment, modelled as a bath of harmonic oscillators. The bath - qubit interaction is described by the following Hamiltonian

$$H = \sum_j \sigma_z^j \xi_j(t) \tag{2.6}$$

where $\xi_j(t) = \sum_{m,\omega}[\lambda_{j,m}(\omega)a_{m,\omega} + h.c.]$ and $\sigma_{x,y,z}^j$ are the Pauli operators for qubit j. In the previous expression $\lambda_{j,m}(\omega)$ denote the coupling constants between the jth qubit and the oscillator at frequency ω in the mth bath with corresponding annihilation (creation) operator $a_{m,\omega}$ ($a_{m,\omega}^\dagger$).

In the following we concentrate our interest on the register dynamics i.e. on the reduced density operator $\rho(t) = \mathrm{Tr}_E[U(t)\rho(0)U^\dagger(t)]$ where Tr_E denotes the partial trace performed on the environment degrees of freedom. The resulting density matrix can be written in a compact form as [AF03]:

$$\rho(t) = \Xi[U_r\rho(0)U_r^\dagger] \tag{2.7}$$

where Ξ is a map (a super-operator) defined as

$$\Xi = \exp\left[-\frac{1}{2}\sum_{j,j'}\Gamma_{jj'}(\sigma_z^j - \bar{\sigma}_z^j)(\sigma_z^{j'} - \bar{\sigma}_z^{j'})\right] . \tag{2.8}$$

In the above expression we used the convention that a bar over an operator means that it acts on the density matrix from the right. The coefficients $\Gamma_{jj'}(t) = \langle\phi_j(t)\phi_{j'}(t)\rangle$, with $\phi_j(t) = \int_0^t \xi_j(t')dt'$, involve correlations of the bath at different times. Finally the unitary evolution U_r is given by

$$U_r = \exp\left[i\sum_{jj'} V_{jj'}t\sigma_z^j\sigma_z^{j'}\right] \tag{2.9}$$

where the quantity $V_{jj'} = 2\,\mathrm{Re}\sum_{m,\omega}\lambda_{m,j}(\omega)\lambda^*_{m,j'}(\omega)/\omega$ is non zero only if the same reservoir is coupled to different qubits. As we will see in the following, the unitary operator U_r is responsible for the creation of entanglement, while the super-operator Ξ describes dephasing of the off diagonal elements and is present also without spatial correlations of the environment.

As a measure of entanglement between two qubits we use the concurrence (see Cap. 1). In order to obtain information about the global properties of the map we consider states with fixed initial concurrence, which are of the form:

$$|\Psi\rangle = \cos\vartheta|0_{n1}0_{n2}\rangle + \sin\vartheta|1_{n1}1_{n2}\rangle \tag{2.10}$$

with

$$|0_{ni}\rangle = \cos\frac{\vartheta_i}{2}|0\rangle + \sin\frac{\vartheta_i}{2}e^{i\varphi_i}|1\rangle \tag{2.11}$$

$$|1_{ni}\rangle = \cos\frac{\vartheta_i}{2}|1\rangle - \sin\frac{\vartheta_i}{2}e^{-i\varphi_i}|0\rangle \tag{2.12}$$

The concurrence of $|\Psi\rangle$ is $\sin 2\vartheta$. In the following analysis we possibly average over the basis chosen for the two qubits. In other words we average over angles $\vartheta_1, \vartheta_2, \varphi_1, \varphi_2$. This means that the average of a quantity (for example concurrence or fidelity) $f(\vartheta_1, \vartheta_2, \varphi_1, \varphi_2)$ is:

$$f = \frac{1}{(4\pi)^2}\int_0^\pi \sin\vartheta_1 d\vartheta_1 \int_0^\pi \sin\vartheta_2 d\vartheta_2 \int_0^{2\pi} d\varphi_1 \int_0^{2\pi} d\varphi_2 f(\vartheta_1, \vartheta_2, \varphi_1, \varphi_2) \tag{2.13}$$

Since we are dealing with a quantum memory, whose function is to store a quantum state, it is useful to analyze also the fidelity $\mathcal{F}$ of the state of the qubits at a given time ρ with the initial state $|\Psi\rangle$:

$$\mathcal{F} = \langle\Psi|\rho|\Psi\rangle \tag{2.14}$$

Let us now consider the results for the evolution of the two qubits without QEC. For maximally entangled states $|\phi^{\pm}\rangle = (|00\rangle \pm |11\rangle)/\sqrt{2}$ the concurrence is $C(t) = e^{-4(\ {}_{11}+2\ {}_{12}+\ {}_{22})}$ while for $|\psi^{\pm}\rangle = (|01\rangle \pm |10\rangle)/\sqrt{2}$ the concurrence decays as $C(t) = e^{-4(\ {}_{11}-2\ {}_{12}+\ {}_{22})}$. It is easy to see that if the environment has special symmetries, for instance if Γ_{ij} is equal for different i and j then the subspace spanned by $|\psi^{\pm}\rangle$ is decoherence free [PSE96, ZR97]. Note that the typical decoherence times are of the order of $(d\Gamma/dt)^{-1}$. If we choose $|ij\rangle_x$, eigenstates of σ_x as initial states, it is possible to see that the qubits become entangled if $V_{12} > d\Gamma_i/dt$. In fact the entanglement oscillates with a frequency $4V_{12}$ and is damped with a rate proportional to $d\Gamma_i/dt$ (see figure 2.1). This is very similar to the results obtained by Braun [Bra02].

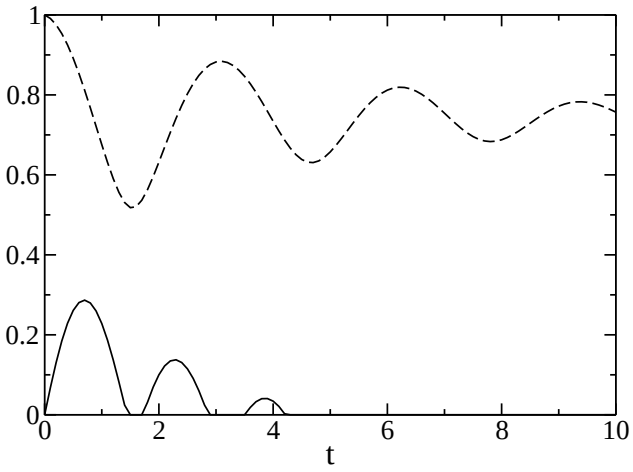

Figure 2.1: Time evolution of fidelity (dashed) and concurrence (solid) between physical qubits, averaged over initial product states ($\vartheta = 0$), in the absence of QEC. The time scale is chosen so that $V = 1$ and $\Gamma(t) \simeq 0.1t$

.

2.2 Evolution in the presence of QEC

Let us now introduce a QEC protocol. Since we the environment induces phase errors we use the encoding procedure described in (2.5).

To calculate the evolution of the density matrix of the two logical qubits in the presence of QEC let us introduce notations that will be useful in writing compact expressions. Let $|\mathbf{a}\rangle_{(z,x)} = |a_1 \dots a_6\rangle_{(z,x)}$ be a generic state of the quantum register in terms of eigenstates of $\sigma_{(z,x)}$ and $\sum_{\mathbf{a}} = \sum_{a_1 \dots a_6 = 0,1}$. The effect of the evolution (2.7) in the basis of eigenstates of σ_z reads:

$$\Xi U_r |\mathbf{a}\rangle_z \langle \mathbf{b}| U_r^\dagger = E(\mathbf{a}, \mathbf{b}) |\mathbf{a}\rangle_z \langle \mathbf{b}| \tag{2.15}$$

where

$$E(\mathbf{a}, \mathbf{b}) = \exp \Bigg\{ - \frac{1}{2} \sum_{jj'} \Gamma_{jj'} \left[(-1)^{a_j} - (-1)^{b_j} \right] \left[(-1)^{a_{j'}} - (-1)^{b_{j'}} \right] + i \sum_{j \neq j'} V_{jj'} \left[(-1)^{a_j + a'_j} - (-1)^{b_j + b'_j} \right] \Bigg\} \tag{2.16}$$

The curly braces is made of two terms: the first containing $\Gamma_{jj'}$ comes from the super-operator Ξ while the second containing $V_{jj'}$ comes from U_r.

The initial density matrix however is written in the basis of eigenstates of σ_x because of the encoding. To circumvent this problem first we change basis to the basis of eigenstates of σ_z, apply the evolution (2.15) and finally return to the original basis.

It is possible to change from x to z basis through

$$|\alpha\rangle_x \langle \beta| = \frac{1}{2^6} \sum_{\mathbf{a},\mathbf{b}} (-1)^{\mathbf{a}\cdot\alpha + \mathbf{b}\cdot\beta} |\mathbf{a}\rangle_z \langle \mathbf{b}|. \tag{2.17}$$

Using (2.17) and (2.15) we may write:

$$\Xi U_r |\mathbf{x}\rangle_x \langle \mathbf{x}'| U_r^\dagger = \frac{1}{2^{12}} \sum_{\mathbf{a},\mathbf{b}} \sum_{\alpha,\beta} (-1)^{\mathbf{x}\cdot\mathbf{a} + \mathbf{x}'\cdot\mathbf{b}} E(\mathbf{a}, \mathbf{b}) (-1)^{\mathbf{a}\cdot\alpha + \mathbf{b}\cdot\beta} |\alpha\rangle_x \langle \beta| \tag{2.18}$$

Until now we considered only the free evolution but at time T we measure the syndrome and apply the correction. After some algebra it is possible to write a linear relation between $\rho(0)$ and $\rho^C(T)$:

$$\begin{aligned}\rho^C(T) &= (z_0 + z_1\sigma_x^1\bar{\sigma}_x^1 + z_2\sigma_x^2\bar{\sigma}_x^2 + z_{12}\sigma_x^1\sigma_x^2\bar{\sigma}_x^1\bar{\sigma}_x^2 \\ &+ w_0\sigma_x^1\sigma_x^2 + w_0^*\bar{\sigma}_x^1\bar{\sigma}_x^2 + w_1\sigma_x^1\bar{\sigma}_x^2 + w_1^*\bar{\sigma}_x^1\sigma_x^2)\rho(0) \end{aligned} \tag{2.19}$$

where:

$$\begin{aligned} z_0 &= \sum_{\mathbf{a},\mathbf{b}} E(\mathbf{a},\mathbf{b})\Phi(\mathbf{a},\mathbf{b}) \\ z_1 &= \sum_{\mathbf{a},\mathbf{b}} E(\mathbf{a},\mathbf{b})\Phi(\mathbf{a},\mathbf{b})(-1)^{\sum_{i=1}^{3}(a_i+b_i)} \\ z_2 &= \sum_{\mathbf{a},\mathbf{b}} E(\mathbf{a},\mathbf{b})\Phi(\mathbf{a},\mathbf{b})(-1)^{\sum_{i=4}^{6}(a_i+b_i)} \\ z_{12} &= \sum_{\mathbf{a},\mathbf{b}} E(\mathbf{a},\mathbf{b})\Phi(\mathbf{a},\mathbf{b})(-1)^{\sum_{i=1}^{6}(a_i+b_i)} \\ w_0 &= \sum_{\mathbf{a},\mathbf{b}} E(\mathbf{a},\mathbf{b})\Phi(\mathbf{a},\mathbf{b})(-1)^{\sum_{i=1}^{6} a_i} \\ w_1 &= \sum_{\mathbf{a},\mathbf{b}} E(\mathbf{a},\mathbf{b})\Phi(\mathbf{a},\mathbf{b})(-1)^{\sum_{i=1}^{3} a_i + \sum_{i=4}^{6} b_i} \end{aligned} \tag{2.20}$$

and

$$\Phi(\mathbf{a},\mathbf{b}) = \frac{1}{2^{12}}\left[1 + \sum_{i=1}^{6}(-1)^{a_i+b_i} + \sum_{i,j=1}^{3}(-1)^{a_i+b_i+a_{j+3}+b_{j+3}}\right] \tag{2.21}$$

When $VT, \Gamma(T) \ll 1$, where T is the time interval between two quantum error corrections, following the same approach of [AF03] we can write the following master equation for the continuous evolution of the density matrix of the two logical qubits

$$\frac{d\rho}{dt} = -(\gamma_1 + \gamma_2)\rho + \gamma_1\sigma_x^1\rho\sigma_x^1 + \gamma_2\sigma_x^2\rho\sigma_x^2 \tag{2.22}$$

where

$$\gamma_i = \frac{2}{T}\sum_{j>j'}(T^2V_{jj'}^2 + 2\Gamma_{jj'}^2(T) + \Gamma_{jj}(T)\Gamma_{j'j'}(T)) \ . \tag{2.23}$$

as in Ref. [AF03]. In Eq. (2.22) we have to take $j = 1, 2, 3$ for $i = 1$ and $j = 4, 5, 6$ for $i = 2$. The rates $\gamma_i \ll d\Gamma_{ij}/dt$ are the same found in [AF03] for the single qubit case.

Let us now turn our attention to the time evolution of the entanglement between logical qubits in the presence of QEC. As a first example we consider the initial state $|\tilde{0}\tilde{0}\rangle$. In this case the only non-vanishing elements at time t are those in the main diagonal, and they decay exponentially with decay constants equal to γ_1, γ_2 and $\gamma_1 + \gamma_2$. If instead we start with a Bell state $|\tilde{\phi^+}\rangle$ of logical qubits the non-zero elements at time t are those on the two diagonals. Such state evolves towards an incoherent superposition of two Bell states whose concurrence decays as $C(t) = e^{-2(\gamma_1+\gamma_2)t}$ and the fidelity with respect to the initial state is $\mathcal{F}(t) = \frac{1}{2}(1 + e^{-2(\gamma_1+\gamma_2)t})$. From these results it is evident that the fidelity and the concurrence, in the presence of QEC, decay with the same rate. It is interesting also to see what happens to the state $|\tilde{i}\tilde{j}\rangle_x$. In this case the density operator does not evolve: $\rho(t) = \rho(0)$. This does not follow from the decoherence free subspace phenomenon but rather from the fact that QEC freezes the unitary evolution by means of the repeated measurements, as in the quantum Zeno effect [MS77b], and the conditional dynamics depending on the measurement outcome.

We can see that averaging over all initial product states $\vartheta = 0, \pi/2$ one finds that the concurrence is always zero and the fidelity decays with a rate proportional to γ_i. For partially or maximally entangled states the entanglement decays monotonically again with decay constants $\gamma_1 + \gamma_2$. This means that QEC suppresses the effective interaction between logical qubits due to the presence of a correlated environment. In other words the bath does not induce entanglement between logical qubits and the entanglement initially present decays. This implies that for small T there is not creation of entanglement since the QEC protocol destroys all the correlations between physical qubits of different logical qubits. The reason for this can be seen in a qualitative way: for a state $|\tilde{0}\tilde{0}\rangle = |000\rangle_x|000\rangle_x$ the operator $U_r = \mathbb{1} + i\sum_{ij} V_{ij} t \sigma_z^i \sigma_z^j$ up to first order creates superpositions like $|000\rangle_x|000\rangle_x + |110\rangle_x|000\rangle_x + \cdots$

which is entangled. After the corrections one gets a mixture of $|000\rangle_x|000\rangle_x$ and $|111\rangle_x|000\rangle_x$ which is no longer entangled. Not surprisingly then QEC inhibits the production of entanglement which is corrected as an error.

This may no longer be true if the time T is comparable to the period of oscillation of entanglement without QEC. In this case the environment have time to create enough entanglement and the QEC may even amplify it.

If the time T between two corrections is not short the approximations which lead to the master equation (2.22) are no longer valid and we must use the exact map which links $\rho(t)$ and $\rho(t+T)$ after the free time evolution and the QEC. In terms of Kraus operators such map can be written as

$$\rho_C(t+T) = \sum_k M_k \rho(t) M_k^\dagger \tag{2.24}$$

where $\sum_k M_k^\dagger M_k = \mathbb{1}$. In our case we found the following seven Kraus operators:

$$\begin{array}{rcccl}
M_0 &=& m_0\mathbb{1} & & m_0 = \sqrt{z_0 - |\mathrm{Im}w_0| - |\mathrm{Re}w_0|} \\
M_1 &=& m_1\sigma_x^1 & & m_1 = \sqrt{z_1 - w_1} \\
M_2 &=& m_2\sigma_x^2 & & m_2 = \sqrt{z_2 - w_1} \\
M_3 &=& m_3\sigma_x^1\sigma_x^2 & \text{where} & m_3 = \sqrt{z_{12} - |\mathrm{Im}w_0| - |\mathrm{Re}w_0|} \\
M_4 &=& m_4(\sigma_x^1 + \sigma_x^2) & & m_4 = \sqrt{\mathrm{Re}w_0} \\
M_5 &=& m_5(\mathbb{1} + \sigma_x^1\sigma_x^2) & & m_5 = \sqrt{w_1} \\
M_6 &=& |m_6|(\mathbb{1} \pm i\sigma_x^1\sigma_x^2) & & m_6 = \sqrt{\mathrm{Im}w_0}
\end{array}$$

The Kraus operators can be related to the $\Gamma_{ij}(T)$ rates, however the expressions which explicit such dependence are lengthy and not of immediate reading. A more transparent picture of the action of the map is instead gained by considering the plot of the coefficients m_i as functions of T (see Fig.2.2). We supposed that $\Gamma_{ij}(T) = \Gamma(T) \simeq 0.1T$ from which it follows that $m_1 = m_2$. Notice that in general $m_4 = m_5$ and that the sign in M_6 depends on the sign of $\mathrm{Im}(m_6)$.

Figure 2.2 shows various regimes for the evolution of the logical qubits. For $VT \ll 1$ only m_0 and m_1 are non zero, leading to the dissipative master equation (2.22). This is best shown in figure 2.3 where the coefficients m_i

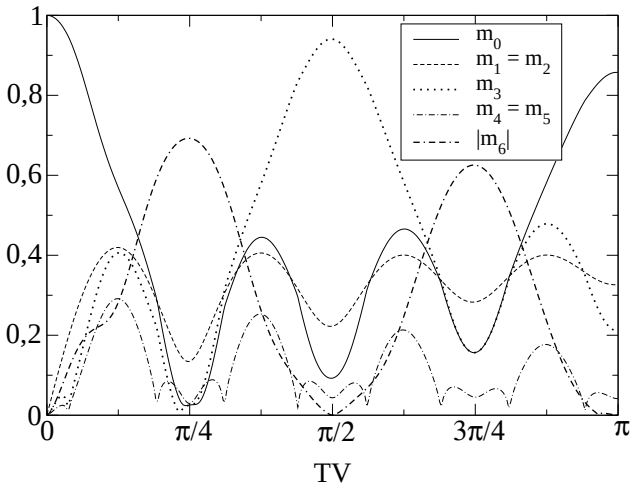

Figure 2.2: Relative weights of the Kraus operators, i.e. the quantities m_i, as functions of T. For simplicity we assume $\Gamma_{ij}(T) = \Gamma(T) \simeq 0.1T$. From this it follows that $m_1 = m_2$.

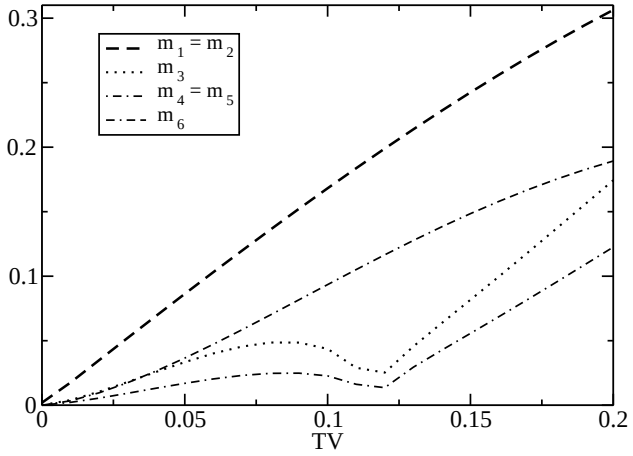

Figure 2.3: Relative weights of the Kraus operators, i.e. the quantities m_i for small VT. Same parameters as in figure 2.2. Notice that m_0 is out of range.

are shown for small values of VT. As we have seen in this regime there is no creation of entanglement because $M_{1,2}$ are single qubit operators. When T is close to the value $\pi/8V$ there are also contributions from the two-qubit operators $M_{4,5,6}$ but the dissipative effect of $M_{1,2,3}$ is predominant and again we verified that the entanglement production is zero. The interesting regime is for $T \simeq \frac{\pi}{4V}$, when the main contribution comes from M_6. As expected in this case there is creation of entanglement that oscillates between zero and a maximum value (which will gradually decay). For the particular choice $T = \frac{\pi}{4V}$ (see figure 2.4) the created entanglement is maximum and the QEC amplifies it. The other non zero dissipative contribution is M_1 and it is present only if Γ_i is non zero. On the other hand, if Γ_i is negligible, M_6 is the only Kraus operator, and therefore the evolution is unitary even in the presence of QEC. Under this condition the evolution induces the transformation $|\tilde{0}\rangle \rightarrow |\tilde{1}\rangle$ and vice versa. For larger T one again finds regimes with no entanglement production. When the map (2.24) is applied (for $\Gamma_i = 0$

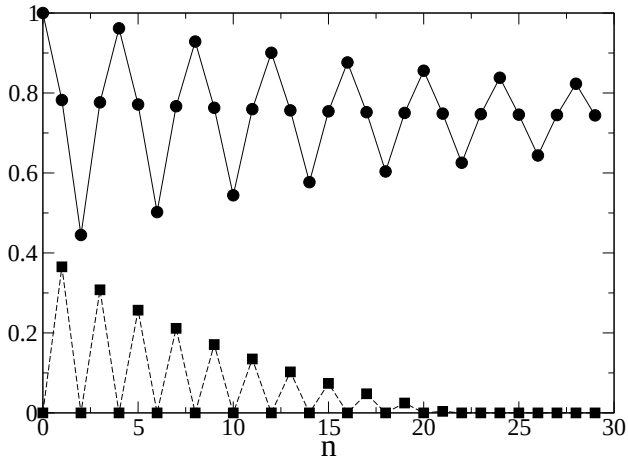

Figure 2.4: Mean fidelity (circle) and concurrence (square) between logical qubits in the presence of QEC as functions of the number of applications of the map, for $T = \pi/4V$, $V = 1$ and $\Gamma(t) \simeq 0.1t$, the same parameters used in figure 2.1.

and $T = \frac{\pi}{4V}$) to the state $|\tilde{0}\tilde{0}\rangle$ then one sees that it makes a sort of periodic

oscillation:

$$|\tilde{0}\tilde{0}\rangle \rightarrow |\tilde{0}\tilde{0}\rangle + i|\tilde{1}\tilde{1}\rangle \rightarrow |\tilde{1}\tilde{1}\rangle \rightarrow |\tilde{0}\tilde{0}\rangle - i|\tilde{1}\tilde{1}\rangle \rightarrow |\tilde{0}\tilde{0}\rangle \tag{2.25}$$

If Γ is not zero then the other Kraus operators also contribute and so this oscillation is damped. This type of oscillation is not restricted to initial product states but also to entangled states as is shown in Fig.2.5. As a

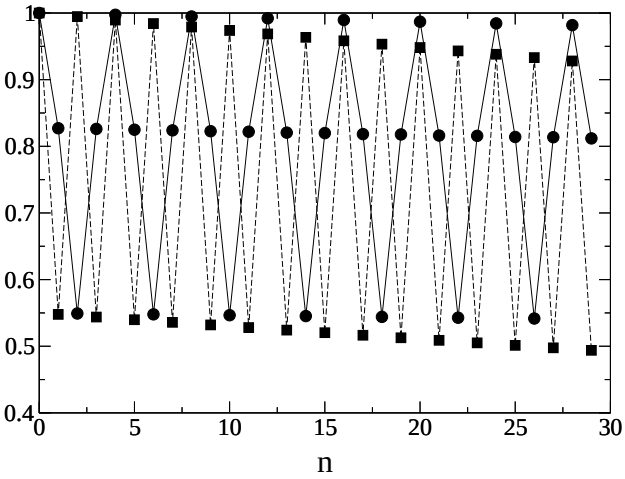

Figure 2.5: Mean fidelity (circle) and concurrence (square) for maximally entangled initial states as functions of the number of applications of the map. Same parameters of figure 2.4

consequence it is possible to create entanglement that can be distilled to obtain maximally entangled states or even extracted from the system. Notice that the period of oscillation of the concurrence is twice that of the fidelity. The reason is that for the concurrence the relative phase in the superposition (2.25) does not matter.

Figure 2.4 shows that the maximum average concurrence obtainable is around 0.4. It is important to underline that this is an average value: there are states, like $|\tilde{0}\tilde{0}\rangle_x$, that do not evolve and so there is no production of entanglement while there are states for which the created entanglement is more than the average value. This is the case of initial product states of the computational basis for which the production of entanglement is maximal.

For example, let us compare the initial states that lead to the maximum production of entanglement with and without QEC. In the presence of QEC the best case is $|\tilde{0}\tilde{0}\rangle$: the entanglement is 0.92 after just one application of QEC. On the other hand the maximum entanglement reached in the case without QEC is only 0.74 for the state $|00\rangle_x$. These results are insensitiv

is that, given an effective interaction in the presence of decoherence, one has to find optimal subsystems and projection protocols in order to maximize the production of entanglement.

Our protocol can be thought as a generalization of the one proposed in Ref. [DVC+01] where the entanglement production is optimized, in the presence of a direct interaction and in the absence of decoherence, by means of local operations and ancillas. In our QEC protocol we use some sort of ancillary system to enlarge the Hilbert space, although in this case there is not a sharp distinction between qubits and ancillas. Furthermore, we make use also of local projections on the enlarged subsystems and conditional dynamics.

Chapter 3

From perfect to fractal transmission in spin chains

The ability to transfer a quantum state between distant parties is a basic requirement in many quantum information protocols. We mention for example quantum key distribution [GRTZ02], necessary for private key cryptographic schemes, or the teleportation [BBC$^+$93]. Until now the best examples of quantum communication come from quantum optics. The carriers of information (photons) can be addressed and transmitted with high control and with a low level of decoherence.

Very recently, in view of the great potentialities of solid-state quantum information, attention is also focusing on the problem of the transfer of quantum information in a solid-state environment. This could have great applications in the development of a quantum processor in which different parts, where information is processed, must communicate. Also these protocols could be useful to create entanglement, necessary for quantum computation, between distant parties. A possible way to follow would be to properly design couplings between optical and solid-state systems [TRBZ04]. However it seems natural to consider also another solid state device as a data bus. This can avoid the difficulties of interfacing different physical systems. A spin network for quantum computation based only on Heisen-

berg interactions has been proposed [BB03, YLB04]. The first example of quantum communication in condesed matter has been put forward by S. Bose [Bos03]. He proposes to use a linear spin chain with Heisenberg interaction as a quantum wire for transmission over reasonable distance ($\sim 10^2$ lattice sites). This work stimulated a flourishing activity and works proceeded in the same spirit modifying and improving the original proposal [Sub04, CDEL04, OL04b, BB05, BGB04, ACDE04, PS05]. Information capacities for this Heisenberg channel have been analyzed in Ref. [GF05]. In Ref. [LSC$^+$05] a slightly different scheme has been proposed, in which the simple spin chain has been replaced with an isotropic antiferromagnetic spin ladder. A great advantage of these approaches is that state transfer occurs due to the interaction between the spins of the chain and no dynamical control is required (except for the preparation and the detection of the state). An advantage of not using external control is that the system during the evolution can be much better decoupled from the environment. Proposals to implement this scheme with superconducting nanocircuits [RFB05, PPKF05] have been already suggested and very likely these implementations can also be extended to other solid-state systems. In this and in the following chapter we discuss two examples of quantum information process realized with spin networks. While in this chapter we analyze quantum communication, in chapter 4 we show how to realize quantum cloning, the imperfect copy of an unknown quantum state, without (almost) any external control.

In Bose's proposal the output fidelity, a figure of merit for the quality of a quantum channel, decays with the length of the chain. There are several ways to circumvent this limitation: using several spin chains in parallel [BB05], if local measurements on the individual spins can be implemented [VMDC04], when communicating parties have access to limited numbers of qubits in a spin ring [OL04b]. Another way to achieve perfect transfer over arbitrary distances is to modify Bose's original proposal by considering a modulated spin chain. As suggested in Ref. [CDEL04] it is sufficient to engineer a spin chain with coupling strengths that position dependent. As in all situations in quan-

tum information, the efficiency of such protocols relies on the capability of isolating the experimental setup from the external world (decoherence) [Zur91]. In the case of the protocols presented in Refs. [Bos03,CDEL04], where no control is needed on the system during the state transfer, that is, no dynamical control is applied, the coupling to the environment is supposed to be weak. In addition to decoherence also static imperfections play an important role in the destruction of information in quantum computers [GS00, BCMS01a], especially in solid-state implementations with engineered nanodevices. For these reasons in this chapter we want to study the effect of static disorder in quantum communication protocols and in particular the ideal case in which perfect state transfer is obtained in Ref. [CDEL04], which has already been experimentally implemented in Ref. [ZLZ$^+$05] using a three qubit nuclear magnetic-resonance quantum computer. Anticipating some results of the work, we study the stability of the state transfer to random, but time independent, variations both of the coupling between the spins and of an externally applied magnetic field. Similar questions for quantum computation protocols have been already analyzed in Refs. [GS00, BCMS01a, BCMS01b]. In that case the loss of efficiency of the protocol was related to the appearance of quantum chaos in a quantum computer register. This relation has been characterized studying the level spacing statistics. Following these lines we study the transition of the level spacing statistics of the spin chain in the presence of static imperfections. Even though it is not possible to frame this problem with the random matrix theory [GMGW98], we show that the level spacing statistic is still a convenient tool to describe the system efficiency in performing the state transfer.

The presence of static imperfections leads also to a clear signature of the modified properties of the time dependence of the fidelity. The degradation of the state transfer corresponds to the emergence of a fractal signal, i.e., the fidelity changes from a periodic function of time to a fractal time series. This behavior has the same origin as the one found in the probability densities of the quantum evolution in tight-binding lattices [Ber96, AKE04].

The chapter is organized as follows. In Sec. 3.1 we introduce the model used throughout this work, we set up the notations, and we briefly review the quantum state transmission protocol of Refs. [Bos03, CDEL04]. We then analyze the fidelity of the transferred state (Sec. 3.2), and the level spacing statistics of the Hamiltonian of the system (Sec. 3.3). Interestingly, the dependence of the fidelity, as a function of the length of the chain and the level of disorder, obeys simple scaling laws. In Sec. 3.4 we take a closer look at the behavior of the fidelity as a function of time. The presence of static imperfections leads to a fractal behavior of the time signal of the fidelity. In the same section, we relate the fractal dimension to the amount of disorder present in the chain. The last section is devoted to the conclusions.

3.1 Model

The protocol introduced in Ref. [Bos03] enables quantum state transfer between two parties by means of a spin chain: the state of the left-most qubit is transferred to the right-most qubit after a given time (dictated by the dynamics of the chain). In Ref. [CDEL04] the approach is the same as in Ref. [Bos03], but the idea is to use a modulated chain whose Hamiltonian is given by

$$H = \sum_{k=1}^{N} B_k \, \sigma_k^z + \sum_{k=1}^{N-1} J_k \, (\sigma_k^x \sigma_{k+1}^x + \sigma_k^y \sigma_{k+1}^y + \Delta \sigma_k^z \sigma_{k+1}^z). \tag{3.1}$$

In Eq. (3.1) N is the number of spins in the chain, σ_k^x, σ_k^y, σ_k^z are the Pauli operators of the kth spin, and Δ is the anisotropy parameters. The parameters B_k and J_k are, respectively, the local magnetic field and the exchange coupling constant. In Bose's proposal [Bos03] $\Delta = 1$, $J_k = J$ and $B_k = B$.

The protocol consists of three steps: initialization, evolution and read-out. The spin chain is initially (at time $t = 0$) prepared in the state

$$|\Psi_0(\vartheta, \varphi)\rangle = (\cos\vartheta|0\rangle + \sin\vartheta \, e^{i\varphi}|1\rangle) \otimes |0\rangle^{\otimes(N-1)}, \tag{3.2}$$

that is, the left-most spin is prepared in a given superposition of its two levels while the others are in their ground state. The state (3.2) will evolve according to the dynamics dictated by Eq. (3.1). Since the Hamiltonian commutes with the total spin component along the z direction, one has to consider separately the evolution of the projection of (3.2) onto the subspaces with different total angular momentum. Since $|\mathbf{0}\rangle$, the chain state with all the spins in $|0\rangle$ is an eigenstate of the Hamiltonian (3.1) it remains to consider only the evolution of the projection of the initial state onto the sector of the Hilbert space $\mathcal{E}_1$ spanned by the states

$$|\boldsymbol{j}\rangle \equiv |0, 0, \cdots 0, 1, 0, \cdots 0\rangle \ , \tag{3.3}$$

which for $j = 1, \cdots, N$ represents a state of the chain where the jth spin is prepared in $|1\rangle$ and the other $N-1$ ones in $|0\rangle$. The evolution of the global state of the chain at time t can thus be written:

$$|\Psi(t)\rangle = \cos\,\vartheta|\mathbf{0}\rangle + \sin\,\vartheta e^{i\varphi}\sum_{j=1}^{N} f_j(t)|\boldsymbol{j}\rangle \ , \tag{3.4}$$

where

$$f_j(t) \equiv \langle \boldsymbol{j}|e^{-iHt}|\mathbf{1}\rangle \ . \tag{3.5}$$

Finally in the read-out stage the accuracy of the state transfer is determined through the analysis of the fidelity

$$\mathcal{F}(t, \vartheta, \varphi) = \langle \Psi_0(\vartheta, \varphi)|\rho_N(t)|\Psi_0(\vartheta, \varphi)\rangle$$

where $\rho_N(t)$ is the reduced density matrix of the Nth spin at time t. We consider the fidelity averaged over the initial state $|\Psi_0\rangle$ distributed uniformly over the Bloch sphere [Bos03],

$$\mathcal{F}(t) = \langle \mathcal{F}(t, \vartheta, \varphi)\rangle_{\vartheta,\varphi} = \frac{|f_N|\cos\gamma}{3} + \frac{|f_N|^2}{6} + \frac{1}{2}. \tag{3.6}$$

where $\gamma = \arg f_N$. We ignore the phase of f_N as it can be gauged away by a proper choice of the external field. For convenience we therefore set $B_k = 0$

and we choose $\Delta = 0$ since for $\Delta \neq 0$ the same conclusions hold choosing the magnetic field properly [CDD+05]. Let us consider the projection of the Hamiltonian (3.1) onto the subspace $\mathcal{E}_1$:

$$\tilde{H} = \begin{pmatrix} 0 & J_1 & 0 & \cdots & 0 \\ J_1 & 0 & J_2 & \cdots & 0 \\ 0 & J_2 & 0 & \ddots & 0 \\ \vdots & 0 & \ddots & \ddots & J_{N-1} \\ 0 & 0 & \cdots & J_{N-1} & 0 \end{pmatrix} \tag{3.7}$$

For $J_k = J\sqrt{k(N-k)}$ in (3.7) $\tilde{H} \propto S_x$ where S_x is the x component of the angular momentum operator for a spin $\vec{S} = (N-1)/2$. The N basis states $|\boldsymbol{j}\rangle$ of $\mathcal{E}_1$ can be put in one-to-one correspondence with the eigenstates of the angular momentum of this large pseudospin (see Fig. 3.1). The evolution operator is simply a rotation around the axis x with constant angular velocity $J/2$. The initial condition (3.2) corresponds to the eigenstates of S_z with the largest component and the evolution of the state of the chain corresponds to a rotation of the pseudospin around the x axis. After half of the period, $Jt = \pi/4$, the pseudospin has minus the largest component of S_z and this corresponds to the state of the chain to be:

$$|\Psi_1(\vartheta, \varphi)\rangle = \cos\,\vartheta|\mathbf{0}\rangle + \sin\,\vartheta e^{i\varphi}|\boldsymbol{N}\rangle, \tag{3.8}$$

for which the input state is exactly transmitted to the final spin.

Perfect transmission occurs at times $t_n = (2n+1)\pi/4J$. (n integer). In order to analyze the robustness of this protocol to static imperfections, we model their effects by adding to the Hamiltonian a random perturbation both in the exchange couplings and in the local variations of the magnetic field. The coefficients in Eq. (3.1) are replaced with the new values

$$B_k \to b_k, \quad J_k \to J_k(1+\delta_k)$$

where δ_k and b_k are random variables with uniform distribution in the intervals $\delta_k \in [-\varepsilon_J, \varepsilon_J]$ and $b_k \in [-\varepsilon_B, \varepsilon_B]$. Eventually, we will average over

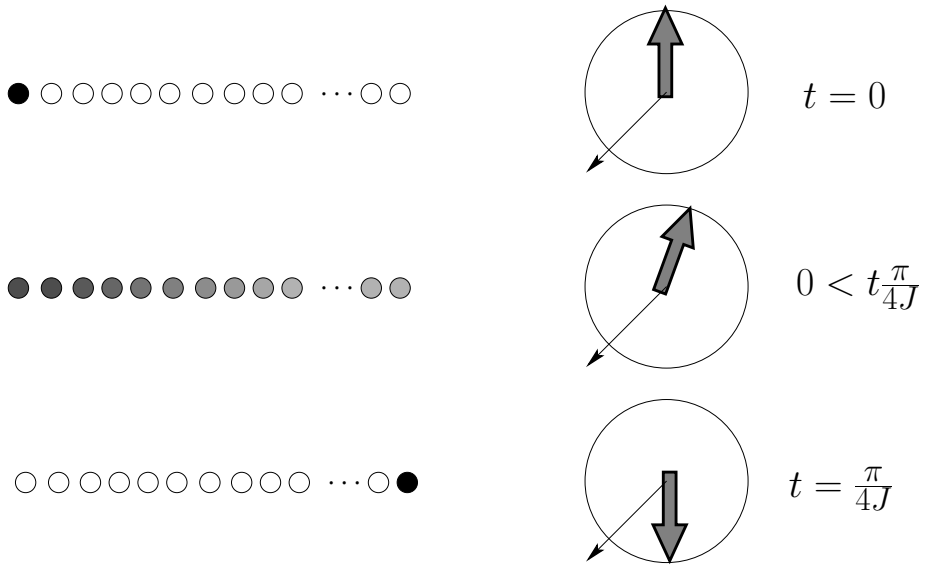

Figure 3.1: Correspondence between the evolution of the initial state (3.2) in the subspace $\mathcal{E}_1$ and the precession of a large spin around a magnetic field. The transmission of information corresponds to a π rotation of the spin.

different disorder realizations, that is,

$$\overline{\mathcal{F}}(t) = \langle \mathcal{F}(t) \rangle_{\mathcal{D}} \tag{3.9}$$

where $\langle . \rangle_{\mathcal{D}}$ stands for the average over different imperfection configurations. The results presented in this paper are obtained by averaging over N_{av} different disorder realizations.

3.2 Stability of the communication in a disordered chain

We numerically solve the Schrödinger equation for the dynamical evolution and compute the fidelity of the rightmost spin with respect to the input state. In Fig. 3.2 we plot typical results of this evolution both for the ideal case (Fig. 3.2 a)) and in presence of imperfections (Fig. 3.2 b).). Figure 3.2 c) is the result of an average over 10^2 disorder realizations. In the presence of

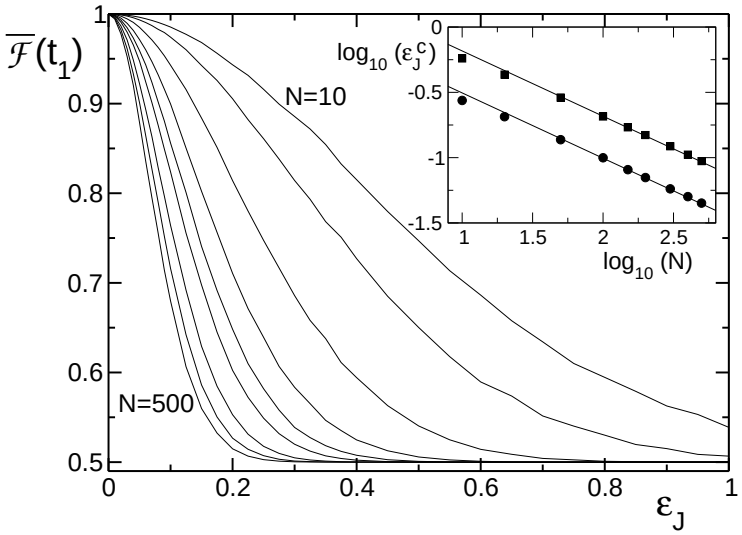

Figure 3.3: Averaged fidelity at time t_1 as a function of the disorder ε_J for different spin-chain lengths and $\varepsilon_B = 0$, $N_{av} = 10^3$. From right to left $N = 10$, 20, 50, 100, 150, 200, 300, 400, 500. Inset: ε_J^c as a function of N obtained from the condition $\overline{\mathcal{F}}(t_1) = 0.9$ (circles) and $\overline{\mathcal{F}}(t_1) = 0.7$ (squares). Straight lines are proportional to $N^{-0.5}$. Here and in the following figures the logarithms are decimal.

disorder the simple periodicity of the fidelity oscillation is lost. Moreover, the maximal value of the fidelity is less than unity (it is reached at slightly different time intervals as compared to the ideal case). The periodicity of the signal of the ideal case is recovered averaging over different disorder realizations, however, the maxima are progressively suppressed on increasing time. Therefore the optimal state transfer, in presence of imperfections, is obtained in correspondence of the first peak at time $t_1 = \pi/4J$.

In this section we concentrate on the dependence of the optimal fidelity ($\overline{\mathcal{F}}$ at time t_1) as a function of static imperfection strength and of the chain length.

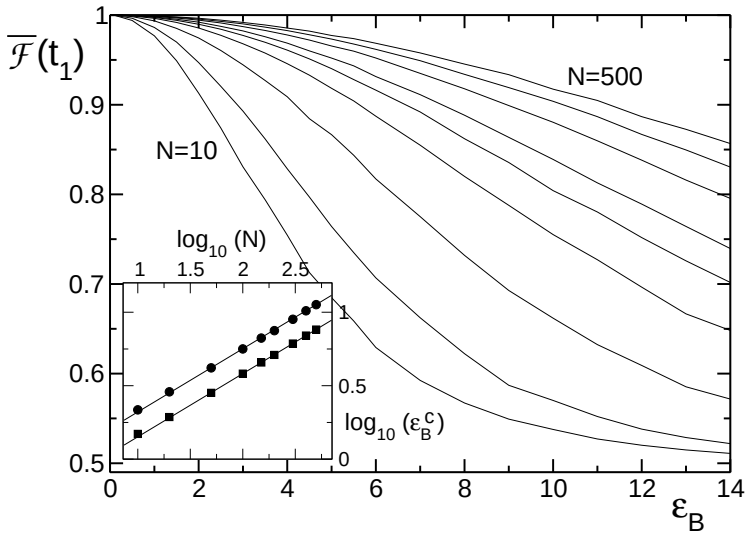

Figure 3.4: Averaged fidelity at time t_1 as a function of magnetic field disorder ε_B for different spin-chain lengths and $\varepsilon_J = 0$, $N_{av} = 10^3$. From left to right N = 10, 20, 50, 100, 150, 200, 300, 400, 500. Inset: ε_B^c as a function of N obtained from the condition $\overline{\mathcal{F}}(t_1) = 0.9$ (circles) and $\overline{\mathcal{F}}(t_1) = 0.95$ (squares). Straight lines are proportional to $N^{0.43}$.

In Fig. 3.3 we report the fidelity as a function of ε_J for different chain lengths assuming, for the moment, that there is no disorder in the local field ($\varepsilon_B = 0$). The opposite situation, with disordered local magnetic field ($\varepsilon_B \neq 0$) and ideal nearest neighbor interaction ($\varepsilon_J = 0$) is shown in Fig. 3.4.

These sources of disorder lead to a striking different behavior. While in the first case the error introduced by the imperfections increases with N, the effect of the disorder on local magnetic field decreases, becoming less effective on increasing the chain length. For completeness we show the case where both ε_B and ε_J are different from zero in Fig. 3.5. The fact that the two effects are almost independent are related to the fact that we are working in the sector with one spin up.

The behavior of the fidelity obeys a simple scaling law. We verified numerically that it scales as

$$\overline{\mathcal{F}}(t_1) = \frac{1}{2}(1 + e^{-\kappa_J N \varepsilon_J^2 - \kappa_B \varepsilon_B^2 / N}) \tag{3.10}$$

where $\kappa_J \sim 0.2$ and $\kappa_B \sim 0.7$. The constants κ_J (κ_B) have been obtained from the dependence, as a function of N, of the value ε_J^c (ε_B^c) at which the fidelity reaches a given threshold value (see the insets of Figs. 3.3 and 3.4).

The scaling given in Eq. (3.10) can be justified in the limit of very small disorder by means of perturbation theory. In the limit $\varepsilon_J t, \varepsilon_B t \ll 1$, the fidelity reads

$$\begin{aligned} \overline{\mathcal{F}}(t) &\approx 1 - \frac{\varepsilon_B^2}{3} \sum_{k=1}^{N} \Big(2\,\Re e[D_{k,k}(t)] - C_k^2(t) \Big)/3 \\ &- \frac{\varepsilon_J^2}{3} \sum_{k=1}^{N} \Big(2\,\Re e[F_{k,k}(t)] - E_k^2(t) \Big)/3 \end{aligned} \tag{3.11}$$

The coefficients C_k, $D_{k,k}$, E_k, and $F_{k,k}$ as well as the details of the calculation are given in appendix A. The disorder in the local magnetic field averages out in the limit of infinite spin chains. In view of the little effect of random fields on the quantum communication over long chains, from now on we will consider only the effect of disordered exchange coupling between spins.

The presence of spatial correlation in the disorder is a concrete possibility in experimental realizations of this protocol, as, for example, with Josephson-junction chains [RFB05, PPKF05]. We model correlated disorder as follows:

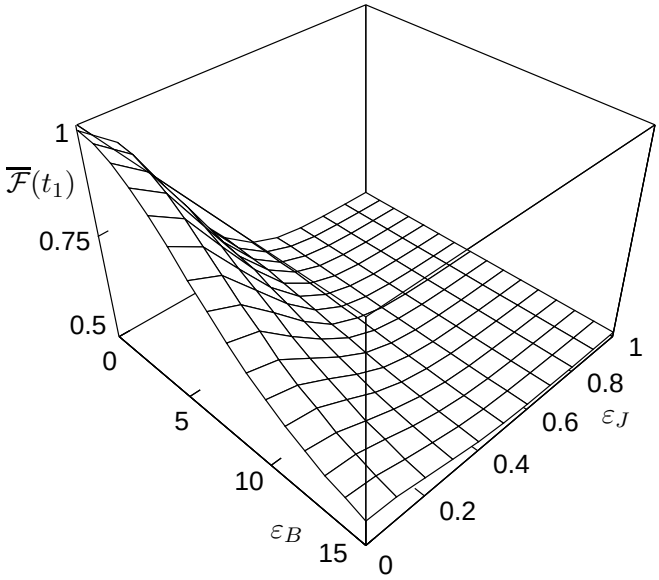

Figure 3.5: Average fidelity at time t_1 as a function of the amplitudes of disorder ε_J, ε_B for a $N = 50$ spin network, $N_{av} = 100$.

The sign of any single δ_k, the error on the kth coupling, is correlated with the previous one following the rule:

$$\begin{aligned} &\delta_i\delta_{i-1} > 0 \quad \text{with probability } \mathcal{P}, \\ &\delta_i\delta_{i-1} < 0 \quad \text{otherwise.} \end{aligned} \tag{3.12}$$

The correlations introduced in Eq.(3.12) result in a perfect correlation (anticorrelation) in the signs between the fluctuations among nearest neighbors if $\mathcal{P} = 1$ ($\mathcal{P} = 0$). Uncorrelated disorder is recovered for $\mathcal{P} = 0.5$. In Fig. 3.6 the fidelity as a function of ε_J ($\varepsilon_B = 0$) for different values of $\mathcal{P}$ is plotted. Notice that the fidelity decay is a monotonic function of $\mathcal{P}$. Anticorrelated disorder is more dangerous than correlated one.

Within the model of disorder studied in this work, strong fluctuations of the exchange couplings lead to a degradation of the signal while the same protocol is not very sensitive (especially for long chains) to fluctuations in the local magnetic fields.

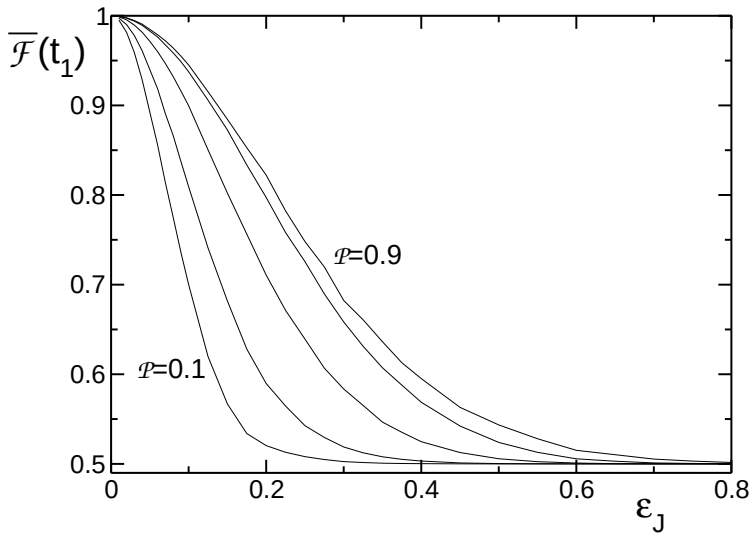

Figure 3.6: Fidelity at time t_1 as a function of ε_J with $N = 100$, $N_{av} = 200$ and from left to right $\mathcal{P} = 0.1$, 0.25, 0.5, 0.75, 0.9.

3.3 Level spacing statistics

The behavior of the fidelity is essentially dictated by the time dependence of the amplitude f_N defined in Eq. (3.5). A deeper insight of its characteristics in disordered chains can be understood by analyzing the statistics of the level spacing of the spin-chain Hamiltonian in presence of disorder. The level spacing statistics $P(s)$ is widely used to study complex many-body systems [Haa91] and quantum systems with classically chaotic counterparts [Izr90] in the framework of random matrix theory [GMGW98]. The distribution $P(s)ds$ gives the probability that the energy difference between two adjacent levels (normalized to the average level spacing) belongs to the interval $[s, s + ds]$. The only non zero entries in the Hamiltonian (3.1) is a tridiagonal matrix (thus not a random matrix) however, we will show that this analysis helps in understanding the behavior of the disordered chain. The level spacing statistics can still be used to characterize the crossover that static imperfections induce in the spectrum of the Hamiltonian.

As already said the only non zero entries in the Hamiltonian matrix are

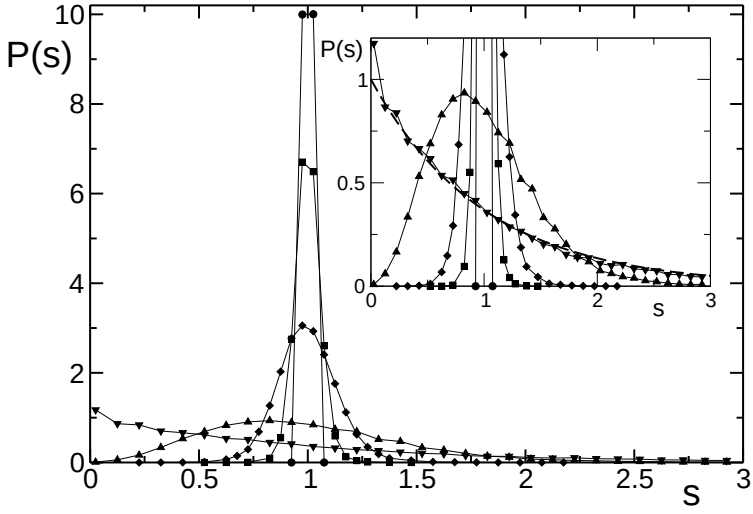

Figure 3.7: Level spacing statistics $P(s)$ for $N = 100, \epsilon_B = 0$, $N_{av} = 10^3$ and different values of ϵ_J: $\epsilon_J = 10^{-3}$ (circles), $\epsilon_J = 2 \times 10^{-2}$ (squares), $\epsilon_J = 5 \times 10^{-2}$ (diamonds), $\epsilon_J = 2 \times 10^{-1}$ (triangles up), $\epsilon_J = 1$ (triangles down). Inset: magnification of the same figure around $s = 1$. The dashed line corresponds to the Poissonian $P_P(s)$.

$H_{k,k+1} = H_{k+1,k} = \lambda\sqrt{k(N-k)}$ where N is the chain length and λ a constant. In the absence of any perturbation ($\epsilon_J = \epsilon_B = 0$) the energy levels are then equally spaced, while in presence of strong random perturbations ($|\epsilon_J| \sim 1$) its eigenvalues are completely uncorrelated. This crossover is detected by the level spacing statistics. It changes from a delta function to a Poisson distribution given by the formula

$$P_D(s) = \delta(s-1) \quad \text{no disorder} \tag{3.13}$$

$$P_P(s) = \exp(-s) \quad \text{strong disorder.} \tag{3.14}$$

Figure 3.7 shows this crossover: $P(s)$ changes from one limiting case to the other as a function of static imperfection strength. This crossover can be quantitatively characterized by the parameter:

$$\eta = \frac{\int_0^1 |P(s) - P_P(s)| ds}{\int_0^1 |P_D(s) - P_P(s)| ds}, \tag{3.15}$$

which varies from $\eta = 1$ in the case of a delta function to $\eta = 0$ for a Poisson

distribution [GS00]. In Fig. 3.8 we show the dependence of η on the strength of the perturbation. The crossover starts at $\epsilon_J \sim 10^{-3} - 10^{-2}$ depending on the length of the chain. In the inset of Fig. 3.8 we report the dependence of the imperfection strength η_c at which the parameter η reaches a given constant value ($\eta = 0.5, 0.8$). The threshold η_c drops with the spin length as

$$\eta_c \sim N^{-0.5}.$$

Thus it follows the same law found in the previous section regarding the fidelity of the state transfer.

In the next section, we show that the same crossover is reflected with the appearance of a fractal behavior in the fidelity time series.

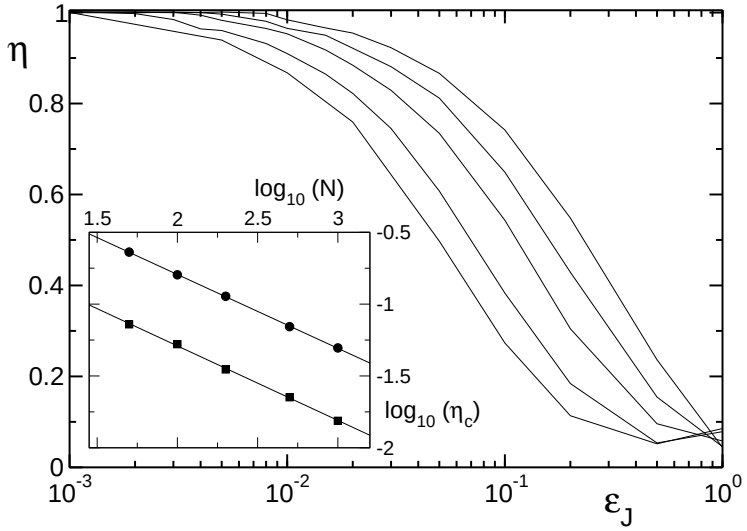

Figure 3.8: The parameter η as a function of the strength of the static imperfections ϵ_J. Different curves correspond to different spin chain length: from right to left $N = 50$, $N = 100$, $N = 200$, $N = 500$. We averaged over N_{av} disorder realizations with $N_{av} = 10^4$. Inset: scaling of the parameter η_c as a function of the chain length N obtained from the condition $\eta = 0.5$ (circles) and $\eta = 0.8$ (squares). Straight lines are proportional to $N^{-0.5}$.

3.4 Fractal dimension of the fidelity

Finally in this section we discuss the temporal behavior of the fidelity in the presence of disorder. The most striking change in the fidelity is that it becomes a fractal function of time. In order to measure the fractal dimension of the signal we used the modified box counting algorithm [SKG+98]. In the standard box counting algorithm the fractal dimension D of the signal is obtained by covering the data with a grid of square boxes of size L^2. The number $M(L)$ of boxes needed to cover the curve is recorded as a function of the box size L. The (fractal) dimension D of the curve is then defined as

$$D = -\lim_{L\to 0} \log_L M(L). \tag{3.16}$$

One finds $D = 1$ for a straight line, while $D = 2$ for a periodic curve. Indeed, for times much larger than the period, a periodic curve covers uniformly a rectangular region. Any given value of D in between of these integer values is a signal of the fractality of the curve. The modified algorithm of Ref. [SKG+98] follows the same lines but uses rectangular boxes of size $L \times \Delta_i$ (Δ_i is the largest excursion of the curve in the region L). Then, the number

$$M(L) = \frac{\sum_i \Delta_i}{L} \tag{3.17}$$

is computed (the time boxes L are expressed in units of the exchange coupling J). For any curve a region of box e 07184x5357(Δ)2.92332]TJΩ/R425-8(s)9269es

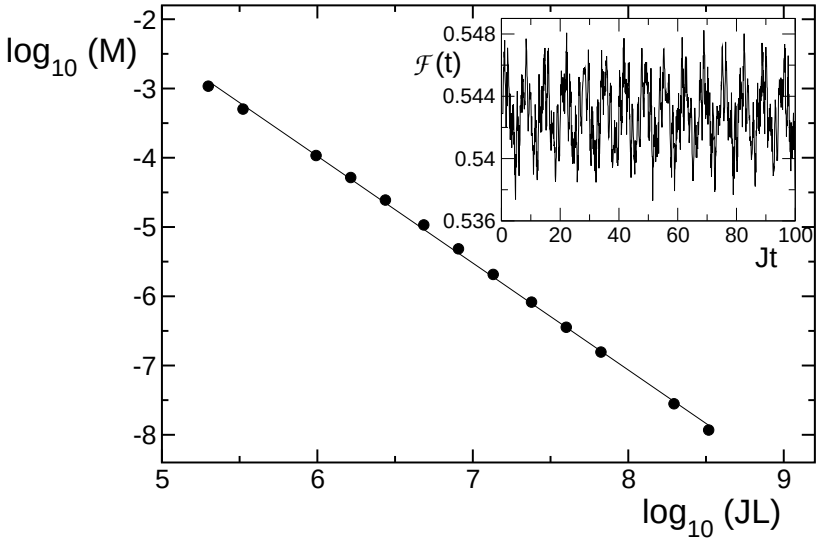

Figure 3.9: M as a function of the interval JL. A numerical fit gives a fractal dimension $D = 1.52$. Inset: Temporal evolution of the fidelity up to time $T = 10^4/J$ in the presence of disorder for $\varepsilon_J = 0.26$, $\varepsilon_B = 0$, $N_{av} = 1$, $N = 500$.

different disorder configurations. We instead average over different input states in order to show that the fractality of the fidelity is a common feature for all qubit states. The inset of Fig. 3.9 shows the typical fluctuating signal we analyzed while Fig. 3.9 shows the numerically computed function $M(L)$ which gives a fractal dimension $D = 1.52$. It is natural to investigate the dependence of the fractal dimension with the static imperfection strengths: the results of numerical simulations are given in Fig. 3.10. The curve changes gradually its dimension from $D \approx 2$ (periodic curve) to $D = 1$ for very large imperfection strengths. This last result is due to the fact that for very large disorder the fidelity drops almost immediately to 0.5 corresponding to a complete loss of the initial state information: the fidelity remains then constant, characterized by dimension $D = 1$. For $\epsilon \sim 0$ D is not exactly 2 as expected, this is a consequence of the finiteness of the time interval that we analyze. The most general situation in presence of static imperfections is a fidelity with fractal dimension: defining, as before, a threshold of disorder

strength D_c at which the fidelity has a given fractal dimension (between two and one), we find that this threshold drops as

$$D_c \sim N^{-0.5}.$$

This behavior is shown in Fig. 3.11 and follows exactly the same scaling as the parameters η_c and ϵ_J^c.

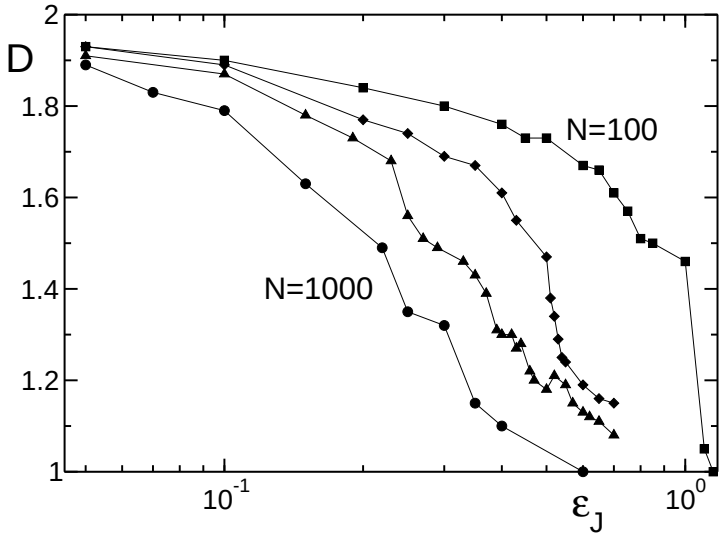

Figure 3.10: Fractal dimension D of the signal $\mathcal{F}(t)$ as a function of the perturbation strength ε_J for $\varepsilon_B = 0$, $N_{av} = 1$ and, from right to left, $N = 100$, $N = 200$, $N = 500$, $N = 1000$. The error on the fractal dimension is of the order of three percent. For $\varepsilon_J < 5 \times 10^{-2}$ the error on the fractal dimensions D increases significantly as $L_{min} \lesssim L_{max}$.

3.5 Conclusions

We have shown that static imperfections in a modulated spin chain destroy, above a given threshold, the transmission of quantum states if performed following the protocols presented in Ref. [CDEL04, CDD+05]. We characterize the effects of static imperfections by means of the fidelity of the state transmission. This transition is reflected in the changing of the level spacing

statistics (from delta-correlated to completed uncorrelated) and in the behavior of the fidelity time series: the perfect state transfer is characterized by a periodic fidelity with integer fractal dimension while beyond the critical threshold it is described by a fractal dimension. We characterize these crossovers by analyzing $\epsilon_J^c, \eta_c, D_c$: the imperfection strength needed to reach this value defines a critical threshold. The three distinct critical thresholds follow the same scaling as a function of the chain length and imperfection strength, independently from the critical value chosen. This common behavior reflects the profound changes in the quantum system induced by the presence of static imperfections. The threshold drops as the square root of the chain length: this is a behavior similar to the one found in Ref. [BCMS01a] in a different system where it was a consequence of the two body nature of the interactions. Here, the dependence is mainly due to the fact that the system is confined to the subspace of one excitation. The conclusion of this analysis is that it is possible, at least in principle, to tolerate or correct the errors introduced by static imperfection.

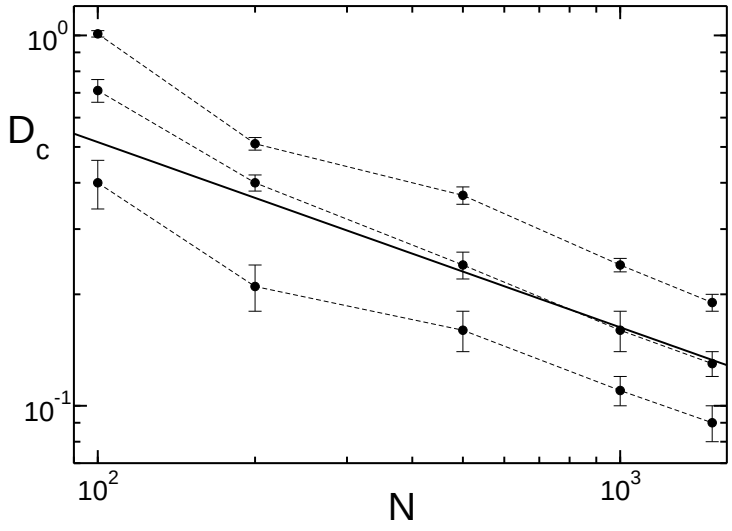

Figure 3.11: Scaling parameter D_c as a function of chain length N from the condition $D = 1.76, 1.6, 1.4$ (from bottom to the top) from Fig. 3.10. The full straight line is proportional to $N^{-0.5}$.

Chapter 4

Quantum cloning in spin networks

4.1 Introduction

The no cloning theorem [WZ82] states that it is impossible to make perfect copies of an unknown quantum state. Differently with the classical world, where it is possible to duplicate information faithfully, the unitarity of time evolution in quantum mechanics does not allow to build a perfect quantum copying machine. This no go theorem is at the root of the security of quantum cryptography [GRTZ02], since an eavesdropper is unable to copy the information transmitted through a quantum channel without disturbing the communication itself. Although perfect cloning is not allowed, it is nevertheless possible to produce several approximate copies of a given state. Several studies, starting from the seminal paper by Bužek and M. Hillery [BH96], have been devoted to find the upper bounds to the fidelity of approximate cloning transformations compatible with the rules of quantum mechanics [SIGA05]. Besides the theoretical interest on its own, these works

ally quantified in terms of the fidelity of each output cloned state with respect to the input. The largest possible fidelity depends on several parameters and on the characteristics of the input states. For an $N \to M$ cloner it depends on the number N of the input states and on the number M of output copies. It also depends on the dimension of the quantum systems to be copied. Moreover, the fidelity increases if some prior knowledge of the input states is assumed. In the universal cloning machine the input state is unknown. A better fidelity is achieved, for example, in the phase covariant cloner (PCC) where the state is known to lie on the equator of the Bloch sphere (in the case of qubits). Upper bounds to the fidelity for copying a quantum state were obtained in Refs. [BH96] and [BDE$^+$98] in the case of universal and state dependent cloning respectively. The more general problem of copying $N \to M$ qubits has been also addressed [GM97, BEM98, Wer98a]. The PCC has been proposed in Ref. [BCDM00]. Several protocols for implementing cloning machines have been already achieved experimentally [CJF$^+$02,LLSHB02,PSS$^+$03,DDZ$^+$03]. In all the above proposals the cloning device is described in terms of quantum gates, or otherwise is based on post-selection methods. For example, the quantum circuit corresponding to the $1 \to 2$ PCC consists of two C-NOT gates together with a controlled rotation [NG99].

In this chapter we show how to realize quantum cloning using a spin network and without the use of quantum gates. The main goal is to find a spin network and an interaction Hamiltonian such that at the end of its evolution the initial state of a spin is (imperfectly) copied on the state of a suitable set of the remaining spins. In this chapter we will show that this is indeed possible and we will analyze various types of quantum cloners based on the procedure just described. We will describe a setup for the $N \to M$ PCC and we will show that for $N = 1$ and $M = 2$ the spin network cloning (SNC) achieves the optimal bound. We will also describe the more general situation of cloning of qudits, i.e. d-level systems. An important test is to compare the performance of our SNC with the traditional approach using quantum

gates. We show that in the (unavoidable) presence of noise our method is far more robust.

The chapter is organized as follows. In Section 4.2 we review the basic properties of approximate cloning showing the theoretical optimal bounds. In Section 4.3 we introduce the main results of this chapter, presenting the models and the networks employed for cloning. Sections 4.4 and 4.5 are devoted to the analysis of the spin network model to implement the $1 \to M$ and $N \to M$ phase covariant cloning transformations respectively. The effects of noise are analyzed in Section 4.6, where we compare our cloning setup with cloning machines based on a gate design. In Sect. 4.7 we study the possibility of achieving universal cloning with the spin network approach. In Section 4.8 we generalize the SNC for qutrits and qudits. Finally, in Section 4.9 we propose a Josephson junctions network that realizes the protocol. In Sec. 4.10 we summarize the main results and present our conclusions.

4.2 Optimal fidelities for Quantum Cloning

In this section we give a brief summary of the results known so far for the optimal fidelity achievable for different cloning machines.

4.2.1 Cloning of qubits: universal cloner

We start our discussion by considering quantum cloning of qubits. The most general state of a qubit can be parametrized by the angles (ϑ, φ) as discussed in chapter 1:

$$|\psi\rangle = \cos\frac{\vartheta}{2}|0\rangle + e^{i\varphi}\sin\frac{\vartheta}{2}|1\rangle\,. \tag{4.1}$$

Quantum cloning was first analyzed [BH96], where the $1 \to 2$ universal quantum cloning machine (UQCM) was introduced. By definition the fidelity of a UQCM does not depend on (ϑ, φ). As already mentioned, the quality of the cloner is quantified by means of the fidelity $\mathcal{F}$ of each output copy,

described by the density operator ρ, with respect to the original state $|\psi\rangle$

$$\mathcal{F} = \langle\psi|\rho|\psi\rangle \ . \tag{4.2}$$

The value of the optimal fidelity is achieved by maximizing $\mathcal{F}$ over all possible cloning transformations. The result for the $1 \rightarrow 2$ UQCM is $\mathcal{F} = 5/6 \simeq 0.83$ [BH96,BDE$^+$98]. The general form of the optimal transformation, which requires an auxiliary qubit, has been obtained in Ref. [BDE$^+$98].

4.2.2 Cloning of qubits: phase covariant cloner

When the initial state is known to be in a given subset of the Bloch sphere, the value of the optimal fidelity generally increases. For example, in Ref. [BDE$^+$98] cloning of just two non orthogonal states is studied and it is shown that the fidelity in this case is greater than that for the UQCM. The reason is that now some prior knowledge information on the input state is available. Another important class of transformations, which will be extensively analyzed in the present chapter, is the so called phase covariant cloning (PCC). In this type of cloner the fidelity is optimise

In the $N \to M$ case of PCC, the optimal fidelities were derived in Ref. [DM03]. For the $1 \to M$ PCC case they read [FMWW02]:

$$\mathcal{F} = \frac{1}{2}\left(1 + \frac{M+1}{2M}\right) \qquad \text{for odd } M \tag{4.7}$$

$$\mathcal{F} = \frac{1}{2}\left(1 + \frac{\sqrt{M(M+2)}}{2M}\right) \qquad \text{for even } M \tag{4.8}$$

4.2.3 Cloning of qudits: phase covariant cloner

Optimal cloning has also been studied for systems with higher dimensions. The universal case was discussed in Ref. [Wer98b]. The phase covariant cloner for qudits, i.e. d level systems, acts on input state of the form:

$$|\psi\rangle = \frac{1}{\sqrt{d}} \sum_{i=0}^{d-1} e^{i\varphi_i} |i\rangle \tag{4.9}$$

where $\varphi_0 = 0$, while $\varphi_1, \varphi_2, \ldots, \varphi_{d-1}$ are independent phases.

The case with $d = 3$, cloning of qutrits, was specifically treated in Refs. [DLP01, CDG02], where the optimal fidelity for the double phase covariant symmetric $1 \to 2$ cloner was derived. The optimal $1 \to M$ fidelity in the case of $M = 3k + 1$ (with k positive integer) is given by the simple expression [DM03]:

$$\mathcal{F} = \frac{1}{3}\left(1 + 2\frac{M+2}{3M}\right) \tag{4.10}$$

The fidelity for $1 \to 2$ PCC in dimension d is given by [FIMW03]

$$\mathcal{F} = \frac{1}{d} + \frac{1}{4d}\left(d - 2 + \sqrt{d^2 + 4d - 4}\right) \ . \tag{4.11}$$

More recently the general $N \to M$ case of PCC for qudits was analysed [BDM05]. Explicit solutions were obtained for a number of output copies given by $M = kd + N$, with k positive integer.

The quantum transformations corresponding to the cloning machines described above can be implemented by suitably designed quantum circuits. For qubits, in the $1 \to 2$ and $1 \to 3$ cases the circuits implementing PCC were

derived in Refs. [DDZ+04] and [BBHB97] respectively and they are shown in Fig.4.1 (note that in these cases no auxiliary qubits are needed). In Fig.4.1b

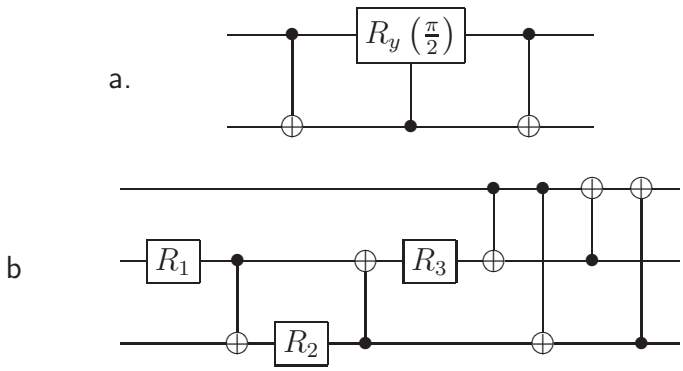

Figure 4.1: a Circuit implementing $1 \rightarrow 2$ PCC for qubits and experimentally realized in [DDZ+04]. b. Circuit implementing $1 \rightarrow 3$ PCC [BBHB97].

we defined $R_i = R_y(-2\vartheta_i)$ and $\vartheta_1 = \vartheta_3 = \pi/8$ and $\vartheta_2 = \arcsin\sqrt{\frac{1}{2} - \frac{\sqrt{2}}{3}}$.

4.3 The spin network cloning

In this section we show how quantum cloning can be implemented using a spin network. First let us discuss our Hamiltonian model. We start with the model defined as

$$H_\lambda = \frac{1}{4}\sum_{ij} J_{ij}(\sigma_x^i\sigma_x^j + \sigma_y^i\sigma_y^j + \lambda\sigma_z^i\sigma_z^j) + \frac{B}{2}\sum_i \sigma_z^i \tag{4.12}$$

where $\sigma_{x,y,z}^i$ are the Pauli matrices corresponding to the i-th site, J_{ij} are the exchange couplings defined on the links joining the sites i and j and B is an externally applied magnetic field. We choose to restrict the anisotropy parameter λ in the range from 0 (XY Model) to 1 (Heisenberg Model). We discuss separately the two limiting cases $\lambda = 1$ and $\lambda = 0$. It turns out that for PCC the $\lambda = 0$ case leads always to the highest fidelity. Given the model of Eq. (4.12) the fidelity is maximized over B/J and Jt. We defined $B^{(M)}$ and $t^{(M)}$ the values of the parameters leading to the optimal solution. Notice

that the total angular momentum as well as its z component are always constants of motion independently of the topology of the network. In all the cases we consider in this chapter, the couplings $J_{ij} \neq 0$ only for nearest neighbors sites i, j, i.e. sites connect with a bond in the corresponding graph. For the $1 \to M$ PCC we choose $M+1$ spins in a star configuration (see fig.

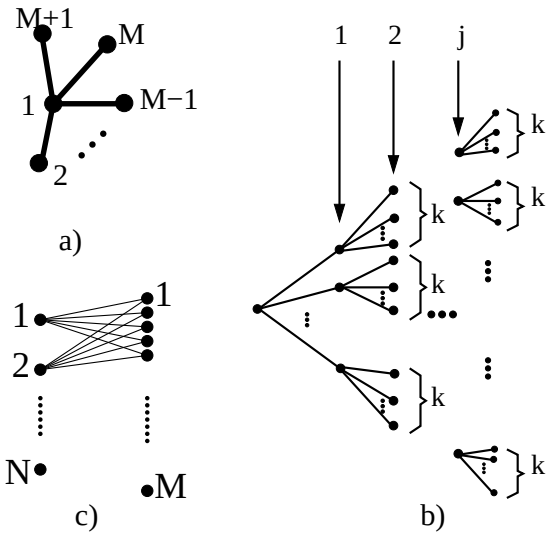

Figure 4.2: Different topologies for $N \to M$ cloner: a) Spin star network for $1 \to M$ cloner. b) Generic graph for the $1 \to M$ cloner with j intermediate steps and k links departing from each vertex. c) Spin network for the $N \to M$ cloning

4.2a). The central spin labeled by 1 is initialized in the input state while the remaining M spins are the blank qubits and are initialized to the state $|0\rangle$ if $0 < \vartheta < \pi/2$ and $|1\rangle$ if $\pi/2 < \vartheta < \pi$. For this network $J_{ij} = J$ only if one of the two linked sites is the central one. This configuration has also been studied in a different context [HB02] where the entanglement properties of the ground state have been analyzed. For the $1 \to M$ case we have considered also other types of networks. These are represented in Fig.4.2b. The input state is placed on the top of the tree while the blank qubits are on the lowest level. The spins at intermediate levels are auxiliary. Each graph is characterized by the number k of links departing from each site and the number j of intermediate levels between the top and the blank

qubits level. The number of blank qubits can be obtained from j and k as $M = k^{j+1}$. Notice that for this class of graphs a symmetry property holds: the global state of the blank qubits is invariant under any permutation of the M qubits. For the $N \to M$ PCC we have considered a generalization of the star network (see Fig.4.2c). It consists of a star with N centers and M tips so no auxiliary qubits are present. Also this network is permutation invariant.

The cases defined above are not the only networks and/or model Hamiltonian conceivable for $N \to M$ cloning. Since the fidelity must be maximized over the parameters of the Hamiltonian as well as over the network topology one may wonder whether it is sufficient to consider only the cases introduced above. In Section 4.4.4 we partially answer to this question by considering the more general configuration for the $1 \to 3$ case containing 4 spins and we believe to have found the best possible scenario for the SNC. As far as the choice of the model Hamiltonian is concerned, the symmetry in the XY-plane is suggested by the phase covariance requirement for a PCC. We checked that the Ising model in transverse field, which is not phase covariant, gives poorer results for the fidelity. In principle one should also explore the possibility of multi-bit couplings, but we did not considered this (in principle interesting) situation. Multi-bit couplings are much more difficult to achieve experimentally and at the end of this work we want to propose to implement our scheme using Josephson nanocircuits, where two-qubit couplings with XY-symmetry are easy to realize.

4.4 $1 \to M$ PCC cloning

In this case the Hamiltonian (4.12) can be easily diagonalized because it can be mapped to the problem of a spin-1/2 interacting with a spin-M/2

$$H_\lambda = J\left(S_x^1 S_x + S_y^1 S_y + \lambda S_z^1 S_z\right) + B(S_z^1 + S_z) \quad . \tag{4.13}$$

where we have defined $S^1 = \sigma^1/2$ and $S = 1/2 \sum_2^{M+1} \sigma^i$. The operators S obey the usual commutation relations for an angular momentum operator.

Notice that the modulus and the z component of the total angular momentum $\vec{F} = \vec{S}^1 + \vec{S}$ commute with the Hamiltonian. Thus the evolution is invariant under rotations around the z axis. This property automatically makes our model a PCC.

For $0 < \vartheta < \pi/2$ (the case for $0 < \vartheta < \pi/2$ is equivalent) the initial state of the star is:

$$|\Psi(0)\rangle = \alpha|\mathbf{0}\rangle + \beta|\mathbf{1}\rangle \tag{4.14}$$

where $\alpha = \cos\frac{\vartheta}{2}$ and $\beta = e^{i\varphi}\sin\frac{\vartheta}{2}$. Here we are using the same notation of Chap. 3 with $M+1$ spins.

Because of the conservation of the total angular momentum the state of the star at time t will be a linear combination of $|\mathbf{0}\rangle$ and $|\boldsymbol{j}\rangle$ i.e. states with only one qubit in state $|1\rangle$. The state at time t can thus be written in the form (apart from a global phase factor):

$$|\Psi(t)\rangle = \alpha|\mathbf{0}\rangle + \beta_1(t)|\mathbf{1}\rangle + \beta_2(t)\frac{1}{\sqrt{M}}\sum_{j=2}^{M+1}|\boldsymbol{j}\rangle \tag{4.15}$$

where the coefficients $\beta_1(t)$ and $\beta_2(t)$ depend on the particular choice of the Hamiltonian and can be expressed as:

$$\beta_1(t) = f_1(t) \equiv \langle\mathbf{1}|e^{-iHt}|\mathbf{1}\rangle \tag{4.16}$$

$$\beta_2(t) = f_{j\neq 1}(t) \equiv \langle\boldsymbol{j}|e^{-iHt}|\mathbf{1}\rangle \tag{4.17}$$

In order to calculate the fidelity of the clones we need the expression for the reduced density matrix of one site. Because of the symmetries of the underlying network this is independent on the site chosen, the result being

$$\rho(t) = \begin{pmatrix} |\alpha|^2 + |\beta_1|^2 + \left(1 - \frac{1}{M}\right)|\beta_2|^2 & \frac{\alpha\beta_2^*}{\sqrt{M}} \\ \frac{\alpha^*\beta_2}{\sqrt{M}} & \frac{|\beta_2|^2}{M} \end{pmatrix} . \tag{4.18}$$

The fidelity for the SNC is then given by

$$\begin{aligned} \mathcal{F}_\lambda &= |\alpha|^2\left[|\alpha|^2 + |\beta_1|^2 + \left(1 - \frac{1}{M}\right)|\beta_2|^2\right] \\ &+ \frac{|\beta_1\beta_2|^2}{M} + 2\mathrm{Re}\left[\frac{|\alpha|^2\beta_1^*\beta_2}{\sqrt{M}}\right] . \end{aligned} \tag{4.19}$$

4.4.1 Heisenberg model

Let us start with the Heisenberg model ($\lambda = 1$) and let $B = 0$ (we checked that a finite external magnetic field is not necessary to achieve the maximum fidelity). The Hamiltonian can be rewritten in the form $H = J\vec{S^1} \cdot \vec{S}$ and using $\vec{S^1} \cdot \vec{S} = 1/2(F^2 - S^2 - S_1^2)$ one finds that the eigenenergies are given by $E(F, S, S^1) = \frac{J}{2}\left[F(F+1) - S(S+1) - S^1(S^1+1)\right]$ where F, S, S^1 are the quantum numbers associated to the corresponding operators. The eigenvectors can be found in terms of the Clebsch-Gordan coefficients. The coefficients $\beta_i(t)$ in this case reduce to:

$$\beta_1(t) = \beta\frac{1}{1+M}\left[M\, e^{i\frac{M+1}{2}t} + 1\right] \tag{4.20}$$

$$\beta_2(t) = \beta\frac{\sqrt{M}}{1+M}\left[1 - e^{i\frac{M+1}{2}t}\right] \tag{4.21}$$

The maximum value for the fidelity

$$\mathcal{F}_1 = \frac{4 + M\,(3+M) + (M-1)[(3+M)\cos\vartheta - \cos 2\vartheta]}{2(1+M)^2} \tag{4.22}$$

is obtained for the parameters $Jt^{(M)} = 2(2k+1)\pi/(M+1)$ where $k = 1, 2, \ldots$.

4.4.2 XY model

Now let us turn our attention to the XY model. Solving the eigenvalue problem as in [HB02] one finds

$$\beta_1(t) = \beta e^{iBt}\cos\frac{J}{2}\sqrt{M}t \tag{4.23}$$

$$\beta_2(t) = -i\beta e^{iBt}\sin\frac{J}{2}\sqrt{M}t \tag{4.24}$$

The fidelity is maximized when $B^{(M)}/J = \sqrt{M}/2$ and $Jt^{(M)} = \pi/\sqrt{M} + 2k\pi$ where $k = 1, 2, \ldots$:

$$\mathcal{F}_0 = \frac{(1+\sqrt{M})^2 - (2-2M)\cos\vartheta + \left(1-\sqrt{M}\right)\cos 2\vartheta}{4M} \tag{4.25}$$

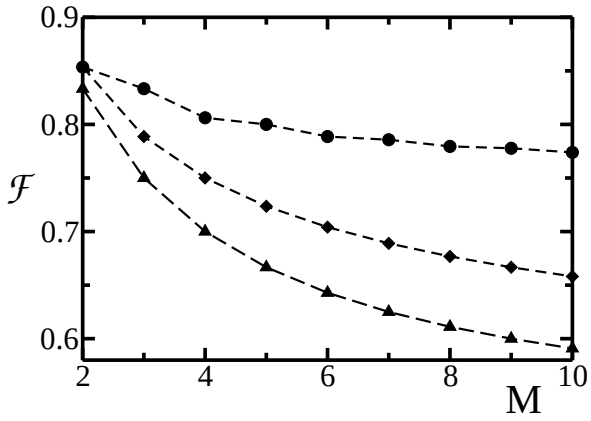

Figure 4.4: The fidelity $\mathcal{F}$ for PCC (circle), XY (diamond) and Heisenberg (triangle) as functions of M for $\vartheta = \pi/2$.

noise, SNC may be competitive with the quantum circuit approach, where the number of gates are expected to *increase* with M. We analyze this point in more details in Section 4.6.

Recently an implementation based on a multi-qubit cavity has been proposed for the realization of our scheme for the PCC with the star configuration [OCJQ05]. In this proposal the central spin is replaced by a bosonic mode of the cavity. By restricting the dynamics in the subspace with only one excitation (one excited qubit or one photon in the cavity) the Hamiltonian is equivalent to the XY spin star network considered here.

All the results discussed so far have been obtained for the star network. Obviously this is not the only choice which fulfills the symmetries of a quantum cloning network. In general one should also consider more general graphs and understand to what extent the fidelity depends on the topology. We analyzed this point by studying the fidelity for the XY model and $\vartheta = \pi/2$ for $M \leq 32$ for the graph b of Fig.4.2 (the fidelity for Heisenberg model in this case is much worse than in the star configuration). We found that the optimal fidelity for these graphs is the same as that obtained with the star configuration though the optimal time is larger.

4.4.3 Imperfections

To assess the robustness of our protocol, it is important to analyze the effect of static imperfections [GS00, BCMS01b]. Indeed in a nanofabricated network, as for example with Josephson nanocircuits, one may expect small variations in the qubit couplings. Here we analyze the $1 \to M$ cloning assuming that the couplings J_{ij} have a certain degree of randomness. For each configuration of disorder J_{1i} are assigned in an interval of amplitude 2ε centered around $J = 1$ with a uniform distribution. First we study the case of uncorrelated disorder in different links. The values of B and t are chosen to be the optimal values of the ideal situation. For a given configuration of the couplings the fidelities of each of the clones are different due to the different coupling with the central spin. Only the average fidelity is again symmetric under permutation among the clones. We average the fidelity over the M sites and over 10^3 realization of disorder. For $\varepsilon = 10^{-1}$ and $M \leq 10$ the mean fidelity decreases only of the 0.2% compared to the optimal value. The effect of imperfections is quite weak on the average fidelity. This is because for certain values of J_{ij} the fidelity of a particular site can become much larger than the fidelity in the absence of disorder; at the same time for the same parameters the fidelity in other sites is very small. In figure 4.5 we show the fidelity for the $1 \to 2$ SNC with imperfections as a function of ε. We study also the case with correlations between the signs of nearest neighbor bonds. We consider samples in which couplings of neighbor sites are shifted from the unperturbed coupling J in the same direction with probability which depends on a parameter μ. We thus choose the probability of equal signs $(J_{1i} - J)(J_{1i+1} - J) > 0$ to be proportional to $\mu \in [-1; 1]$ If $\mu > 0$ than it is likely that two neighbor couplings are perturbed in the same direction and vice-versa. The uncorrelated results are recovered for $\mu = 0$. As shown in figure 4.5, this type of disorder is more destructive.

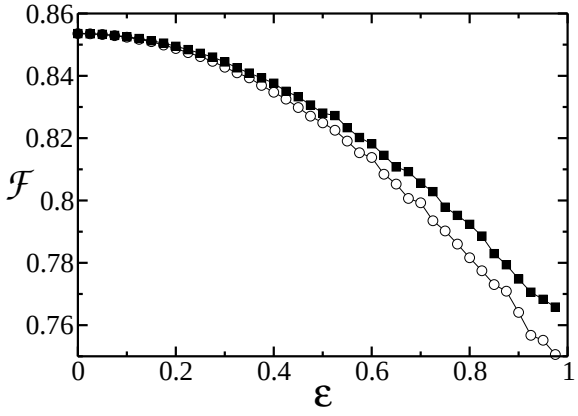

Figure 4.5: Mean fidelity for the $1 \to 2$ case with static imperfections as a function of the tolerance ϵ with $\mu = 0$ (filled squares) and $\mu = 0.5$ (empty circles).

4.4.4 The optimal network Hamiltonian for $1 \to 3$ PCC

As shown in Fig.4.4, the $1 \to 2$ SNC saturates the PCC optimal bound. However this is not the case for $M > 2$, at least for the network topologies considered up to now. One may wonder whether a different choice for the network could allow to approach the optimal fidelity. In order to understand this point we studied the simplest non trivial case namely $M = 3$ and considered the tetrahedron network shown in Fig.4.6.

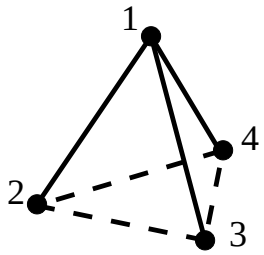

Figure 4.6: The tetrahedron network analyzed for the $1 \to 3$ cloning.

We concentrated on the general anisotropic XXZ model presented in (4.12) in which the local magnetic field and the couplings between the central spin and the blank spin can be different. This is the most general Hamiltonian

for 4 spins that fulfills the symmetry and covariance property. For this general model we maximized analytically the on-site fidelity diagonalizing the corresponding Hamiltonian. We found that the maximum fidelity exactly coincides with that found with the simple star configuration. It is thus demonstrated that, at least for $M \leq 3$, the star configuration is the optimal network for cloning.

It is however important to stress that, given the transformation for the optimal PCC, it is always possible to find a Hamiltonian that generates this transformation during the dynamical evolution. Therefore, at least in principle, one should be able to saturate the optimal value by including other terms in the Hamiltonian (multi-spin coupling for example). Another possibility is to consider a different initial state of the blank qubits as pointed out in [CCWD05]. If this is chosen as a multipartite entangled state the optimal fidelity can be reached. However it is difficult to prepare multipartite states of many spins without using external control. On purpose we chose to limit ourselves to a model which however can be realized experimentally.

4.5 $N \to M$ PCC cloning

In this section we discuss the generalization of the SNC to the $N > 1$ case. A suitable network to accomplish this task is depicted in Fig.4.2c. The model can be mapped to the problem of the interaction between two higher dimensional spins, $N/2$ and $M/2$ respectively. Since we did not succeed in finding the analytic solution (for example for $2 \to 8$ the relevant subspace has dimension 56), we analyzed it numerically. We have simulated the evolution of the network in the range $B/J \in [0.01; 10]$ and $tJ < 5 \cdot 10^3$. We found the absolute maximum of the fidelity $\mathcal{F}_{abs}$ in this interval. The results are summarized in Table 4.1 for several values of N and M. We also calculated the time to reach a value of fidelity slightly lower than $\mathcal{F}_{abs}$. The time needed to reach $\mathcal{F}_{abs} - \delta$, $\delta \ll 1$, is greatly reduced. The fidelity is a quasi periodic function of time approaching several times values very close to $\mathcal{F}_{abs}$. In Table

N	M	$\mathcal{F}_{PCC}$	$\mathcal{F}_{abs}$	Jt_c	J/B	$Jt_c(10^{-2})$
2	3	0.941	0.938	1516.0	39.5	2.9
2	4	0.933	0.889	53.1	4.5	5.3
2	5	0.912	0.853	774.1	12.8	2.7
2	6	0.908	0.825	563.4	28.7	2.8
2	7	0.898	0.804	156.0	40	4.9
2	8	0.895	0.786	116.6	29.9	6.9
3	4	0.973	0.967	2201.6	47.5	111.8
3	5	0.970	0.931	1585.5	33.1	19.6
3	6	0.956	0.905	8.3	10.6	8.3
3	7	0.954	0.875	8.1	3.4	7.9

Table 4.1: The maximum fidelity $\mathcal{F}$ for $N \to M$ for the network of Fig.4.2c. $\mathcal{F}_{PCC}$ is the optimal fidelity for the PCC [DM03]. Column 5 (6) reports the corresponding evolution time t_c (interaction strength J). Column 7 reports the time $t_c(\epsilon = 10^{-2})$ at which the fidelity reaches the value $\mathcal{F}_{abs} - 10^{-2}$. The results refer to the XY model ($\lambda = 0$). The value $\mathcal{F}$ is found by numerical maximization in the intervals $B/J \in [0.01; 10]$ for $N + M < 10$ and $Jt \in [0; 5 \cdot 10^3]$.

4.1 both the absolute maximum $\mathcal{F}_{abs}$ (column 4) in the chosen interval and the time $t_c(\delta = 10^{-2})$ (last column in the table) are shown.

4.6 Quantum cloning in the presence of noise

So far we have described the unitary evolution of isolated spin networks. Real systems however are always coupled to an environment which destroys their coherence. In this section we will try to understand the effect of noise on the SNC. We will also compare the performances of quantum cloning machines implemented with spin networks and with quantum circuits using the same Hamiltonian. The effect of the environment can be modeled in different ways. One is to add classical fluctuations to the external magnetic field B or the coupling J. In Fig. 4.7 we compare the fidelity, averaged over different noise realizations, $\mathcal{F}_{1\to 2}$ and $\vartheta = \pi/2$ as a function of the field variance Δ for the

XY model with the optimal average values for fluctuating J (solid) and B (dashed). The probability distributions are chosen to be Gaussian. Note that the fidelity is more sensitive to fluctuations of B.

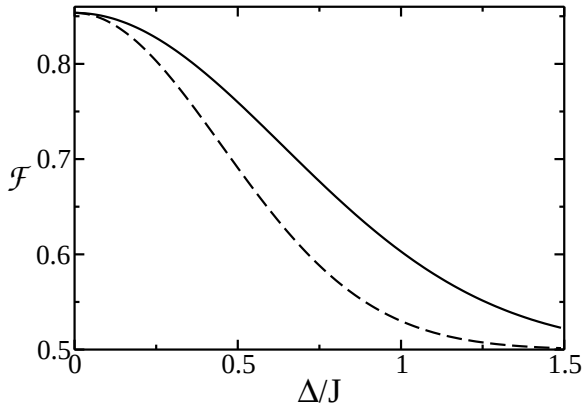

Figure 4.7: Fidelity for equatorial qubits in the XY model with a classical fluctuating field. $\mathcal{F}$ is plotted as a function of the variance Δ for fluctuating J (solid) and B (dashed).

There are situations in which the environment cannot be modeled as classical noise and one has to use a fully quantum mechanical description. Following the standard approach, we model the effects of a quantum environment by coupling the spin network to a bosonic bath. Then the time evolution for the reduced density matrix of the spin system is obtained after tracing out the bath degrees of freedom in terms of a master equation [CTDRG92]. The Hamiltonian for the whole system is

$$H = H_S + H_R + H_I \tag{4.30}$$

$$H_I = \sum_{i=1}^{M+1} \sum_k \lambda_i(k)\ \sigma_z^i \left[a_i^\dagger(k) + a_i(k)\right] \tag{4.31}$$

$$H_R = \sum_{i=1}^{M+1} \sum_k \omega_i(k)\ a_i^\dagger(k)\, a_i(k) \tag{4.32}$$

where H_S is the spin Hamiltonian defined in Eq. (4.12). We considered

the specific case in which the spins degrees of freedom are coupled to the environment through the σ_z operator. This kind of interaction induces only dephasing in the spin system without exchange of energy with the environment.

The model is presented for generic M but we will discuss the results only for $M = 2$ and $M = 3$. We suppose that each spin is coupled to a different bath, labeled by i, and that all baths are independent, $\omega_i(k)$ and $\lambda_i(k)$ are the frequency and the coupling constant of the kth mode of the ith bath. It is convenient to define the operator $E_i = \sum_k \lambda_i(k) \left[a_i^\dagger(k) + a_i(k)\right]$, the environment operator to which the system is coupled.

The master equation in the basis of eigenstates of H_S can be written as:

$$\frac{d}{dt}\rho_{ab} = -\sum_{abcd} \mathcal{R}_{abcd}\ \rho_{cd} \tag{4.33}$$

where the indexes a, b, c, d run over the energy eigenstates and $\mathcal{R}_{abcd}$ is the so called Bloch-Redfield tensor in the interaction picture:

$$\mathcal{R}_{abcd} = \sum_i \int_0^\infty d\tau \left\{G_i(\tau)\Sigma^{>}_{abcd} + G_i(-\tau)\Sigma^{<}_{abcd}\right\} \tag{4.34}$$

where

$$\Sigma^{>}_{abcd} = \delta_{bd} \sum_n (\sigma_z^i)_{an}(\sigma_z^i)_{nc} e^{i\omega_{cn}\tau} - (\sigma_z^i)_{ac}(\sigma_z^i)_{db} e^{i\omega_{ac}\tau} \tag{4.35}$$

and

$$\Sigma^{<}_{abcd} = \delta_{ac} \sum_n (\sigma_z^i)_{dn}(\sigma_z^i)_{nb} e^{i\omega_{nd}\tau} - (\sigma_z^i)_{ac}(\sigma_z^i)_{db} e^{i\omega_{bd}\tau} \tag{4.36}$$

with $(\sigma_z^i)_{ab} = \langle a|\sigma_z^i|b\rangle$. The function $G(\tau)$ is the correlation function of the environment operators in the interaction picture:

$$G_i(\tau) = \mathrm{Tr}\left[\rho_F \widetilde{E_i}(\tau)\widetilde{E_i}(0)\right] \tag{4.37}$$

The functions $G_i(\tau)$ can be related to the spectral density of the bath through

$$[G_i(\tau)]_\omega = 2N_i(\omega)J_i(\omega) \tag{4.38}$$

where $[\cdot]_\omega$ indicates the Fourier transform. In Eq.(4.38) $N_i(\omega) = (e^{\beta\omega} - 1)^{-1}$ is the mean occupation number of the ω_i mode at temperature $T = \beta^{-1}$ and $J_i(\omega) = \pi \sum_{\omega_k} |\lambda_i(\omega_k)|^2 \delta(\omega - \omega_k)$ is the spectral density of the bath. We suppose that the bath is Ohmic, i.e. $J(\omega)$ has a simple linear dependency at low frequencies up to some cut-off:

$$J_i(\omega) = \frac{\pi}{2}\alpha\omega e^{-\omega/\omega_C} \tag{4.39}$$

The parameter α represents the strength of the noise and ω_C is the high energy cut-off frequency.

In order to to compare SNC with traditional quantum cloning machines we have to consider a specific system where the required gates are performed. Obviously this can be done in several different ways: we choose the XY Hamiltonian as the model system for both schemes. In particular we compare the two methods for $M = 2$ and $M = 3$ equatorial qubits. For the quantum circuit approach quantum gates are implemented by a time dependent Hamiltonian. It has been shown [KW02, SS03] that the XY Hamiltonian is sufficient to implement both one and two-qubit gates. The elementary two-qubit gate is the iSWAP:

$$U(\text{iSWAP}) = \begin{pmatrix} 1 & & & \\ & 0 & i & \\ & i & 0 & \\ & & & 1 \end{pmatrix} \tag{4.40}$$

It can be obtained turning on an XY interaction between the two qubits without external magnetic field and letting them interact for $Jt = \pi/4$. By applying the iSWAP gate twice, the CNOT operation can be constructed This means that we need two two-qubit operations for each CNOT. We simulated the circuits shown in Fig. 4.1 for $M = 2$ and $M = 3$ in the presence of noise and we calculated the corresponding fidelities. We neglected the effect of noise during single qubit operations. This is equivalent to assume, as it can happen in real experiments, that the time needed to perform this gates is much smaller than the typical decoherence time. The resulting fidelity will

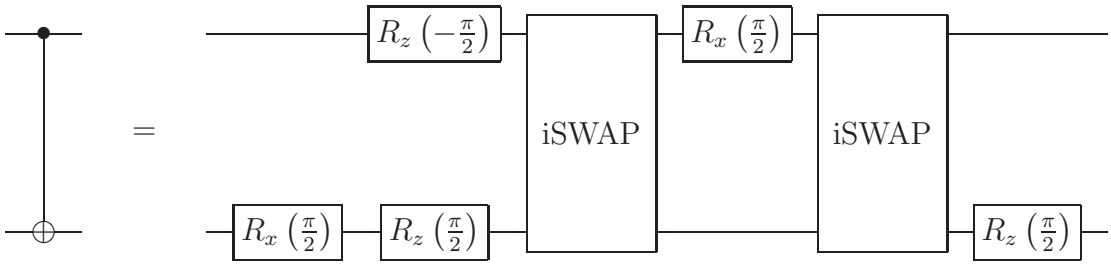

Figure 4.8: Circuit implementing the CNOT from the iSWAP. This circuit is used to implement the quantum cloning by means of gates.

therefore be overestimated. The results are shown in Fig.4.9 and Fig.4.10. The fidelity for the quantum gates (squares) and that for the SNC (circles) are compared as functions of the coupling parameter α. Even for small α the

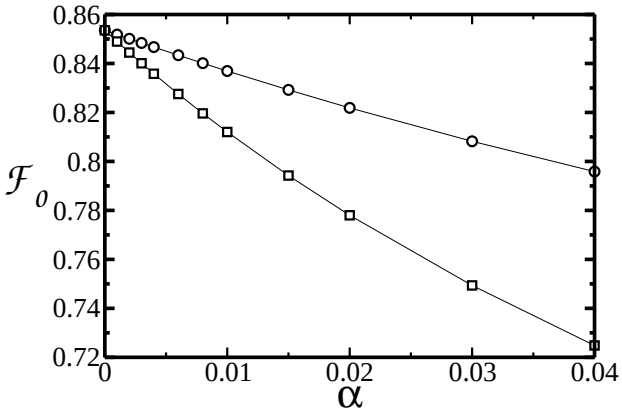

Figure 4.9: $1 \rightarrow 2$ cloning. Comparison of the fidelity $\mathcal{F}_0$ obtained by the spin network method and the quantum circuit (XY interaction) discussed in [DDZ+04, BBHB97] in the presence of an external quantum noise. Circles and squares refer to the network and gates case respectively ($\vartheta = \pi/2.$). The parameters for the environment are $\beta = 10/J$ and $\omega_C = 10^4 J$.

fidelity for the circuits is much worse than that for the network. Notice that for $M = 3$, though without noise ($\alpha = 0$) the SNC fidelity is lower than the ideal one, for $\alpha > \alpha^* = 2.5 \cdot 10^{-3}$ the situation is reversed. This shows that our scheme is more efficient than the one based on quantum gates. Moreover

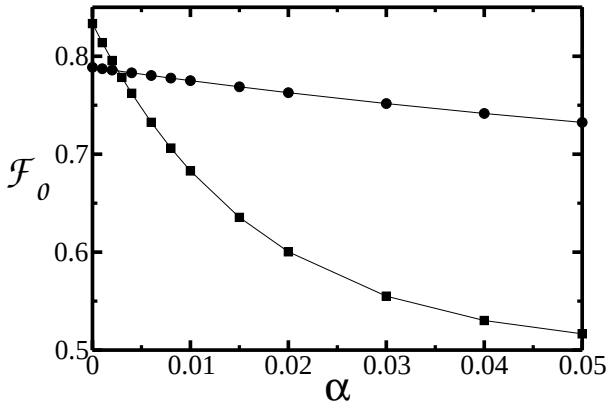

Figure 4.10: The same as in Fig.4.9 for the $1 \rightarrow 3$ case.

for $M > 3$ the time required for quantum circuit PCC grows with increasing M while, as discussed previously, the optimal $t^{(M)}$ of the SNC decreases with M. This suggests that our proposal might be more efficient for growing M. By changing the model does not affect these results. The time required to perform a CNOT using Heisenberg or Ising interactions is just half the time required for the XY model.

We also believe that in a real implementation the effect of noise on our system can be very small compared to the that acting on a quantum circuit. This is because during the evolution the spin network can be isolated from the environment.

4.7 The universal cloner with spin networks

It would be desirable to implement also a universal quantum cloner by the same method illustrated here. In this section we briefly report our attempt to implement the $1 \rightarrow 2$ universal cloner. In the previous sections we demonstrated that for the models presented the fidelity is invariant on φ (phase covariance) but still depends on ϑ. This axial symmetry relies on the selection of the z-axis for the initialization of the blank spins. In order to

perform a universal cloner we need a spherical symmetry. This means that both the Hamiltonian and the initial state must be isotropic. The first condition is fulfilled using the Heisenberg interaction without static magnetic field that would break the spherical symmetry. The second requirement can be obtained using for the initial state of the blank qubits a completely random state. In other words the complete state of the network (initial state + blanks) is

$$\rho(0) = |\psi\rangle\langle\psi| \otimes \frac{1}{4}\mathbb{1}\mathbb{1} \quad . \tag{4.41}$$

The maximum fidelity is obtained for $Jt = \frac{2\pi}{3}$ and has the value $\mathcal{F} = 13/18 \simeq 0.72$ that has to be compared with the value $5/6 \simeq 0.83$ of the optimal universal cloner [BH96]. Our model is the most general time independent network containing 3 spins and fulfills the symmetry and covariance symmetries.

4.8 Quantum cloning of qutrits and qudits

The spin network cloning technique can be generalized to qutrits and qudits. This is what we discuss in this Section starting, for simplicity, with the qutrit case. The cloning of qudits is a straightforward generalization. Our task is to find an interaction Hamiltonian between qutrits able to generate a time evolution as close as possible to the cloning transformation. One obvious generalization of the qubit case is to consider qutrits as spin-1 systems. In this picture the three basis states could be the eigenstates of the angular momentum with z component (-1,0,1). The natural interaction Hamiltonian would then be the Heisenberg or the XY interaction

$$H_I = J_{ij}\vec{S^i}\cdot\vec{S^j} \quad \text{or} \quad H_I = J_{ij}(S_X^i S_X^j + S_Y^i S_Y^j) \tag{4.42}$$

Alternatively one can think to use the state of physical qubits to encode the qutrits. Such an encoding, originally proposed in a different con-

text [KBDW01], uses three qubits to encode one single logical qutrit:

$$\begin{aligned} |0\rangle_L &= |001\rangle \\ |1\rangle_L &= |010\rangle \\ |2\rangle_L &= |100\rangle \end{aligned}$$

In Ref. [KW02

processes are possible. This network is the generalization of the spin star that we analyzed before in which a single qutrit interacts with the others. It is easily generalized for the $1 \to M$ case using three spin stars. The single qutrit Hamiltonian is realized applying magnetic fields to the physical qubits.

In analogy with the qubit cloner we will prepare qutrit 1 in the input state

$$|\psi\rangle = \alpha|0\rangle_L + \beta|1\rangle_L + \gamma|2\rangle_L \tag{4.43}$$

and initialize the other qutrits in a blank state, for example $|0\rangle_L$. Due to the interaction, the state will evolve in a restricted subspace of the Hilbert space:

$$\begin{aligned} |\psi(t)\rangle &= \alpha|000\rangle_L + \beta_1|100\rangle_L + \beta_2|010\rangle_L + \beta_3|001\rangle_L \\ &+ \gamma_1|200\rangle_L + \gamma_2|020\rangle_L + \gamma_3|002\rangle_L \end{aligned} \tag{4.44}$$

To find the fidelity of the clones with respect to the state of Eq.(4.43) we need the reduced density matrix of one of the clones (for example the third). The result, in the basis $(|0\rangle_L, |1\rangle_L, |2\rangle_L)$, is

$$\rho_3 = \begin{pmatrix} 1 - |\beta_3|^2 - |\gamma_3|^2 & \alpha\beta_3^* & \alpha\gamma_3^* \\ \alpha^*\beta_3 & |\beta_3|^2 & \beta_3\gamma_3^* \\ \alpha^*\gamma_3 & \beta_3^*\gamma_3 & |\gamma_3|^2 \end{pmatrix} \tag{4.45}$$

The coefficients $\beta_i(t)$ and $\gamma_i(t)$ can be calculated by diagonalizing the Hamiltonian. We consider the PCC of Eq. (4.9) for $d = 3$: our model is automatically invariant on φ_i because there is no preferred direction in the space of the qutrits. The maximum fidelity achievable with SNC is:

$$\mathcal{F}_3 = \frac{4 + 2\sqrt{2}}{9} \simeq 0.759 \tag{4.46}$$

This value has been obtained with $\Delta/J = 1/\sqrt{2}$ and $Jt = \pi/\sqrt{2}$. This value is very close to the optimal one, the maximum difference between the two values is $\sim 4 \cdot 10^{-3}$ for every $d \geq 2$.

We calculated also the fidelity for the $1 \to M$ cloning of qutrits using the star configuration. The maximum fidelity is:

$$\mathcal{F} = \frac{2 + 4\sqrt{M} + 3M}{9M} \tag{4.47}$$

obtained for the same value of the star configuration of qubits ($Jt^{(M)} = \pi/\sqrt{M}$ and $B^{(M)}/J = \sqrt{M}/2$).

The generalization to qudits is straightforward. Following the same approach we encode qudits using d qubits to encode each qudit. After some algebra one finds the general expression for the PCC in d dimensions. The values $t^{(M)}$ and $B^{(M)}$ are independent from d and the expression for the fidelity is:

$$\mathcal{F}_{1\to 2,d} = \frac{(d-1)(d+2\sqrt{2})+2}{2d^2} \tag{4.48}$$

In Fig.4.12 the optimal and SNC fidelities are compared. As we can see, the fidelity of the spin network implementation is very close to ideal one.

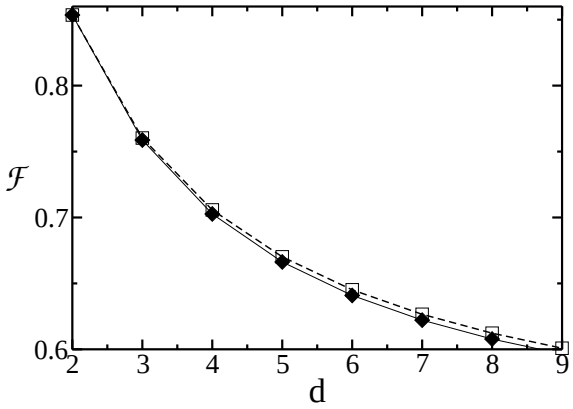

Figure 4.12: The optimal (square) and the SNC (diamond) fidelities for $1 \to 2$ PCC in d dimensions are compared.

4.9 Implementation with Josephson nanocircuits

The final section of this chapter is devoted to the possibility of implementing SNC in solid state devices. Besides the great interest in solid state quantum information, nanofabricated devices offer great flexibility in the design and allow to realize the graphs represented in Fig.4.2. Here we discuss only the $1 \to 2$ cloning for qubits. Generalization to other cases is immediate.

We analyze the implementation with Josephson nanocircuits which are currently considered among the most promising candidates as building blocks of quantum information processors [MSS01, Ave00].

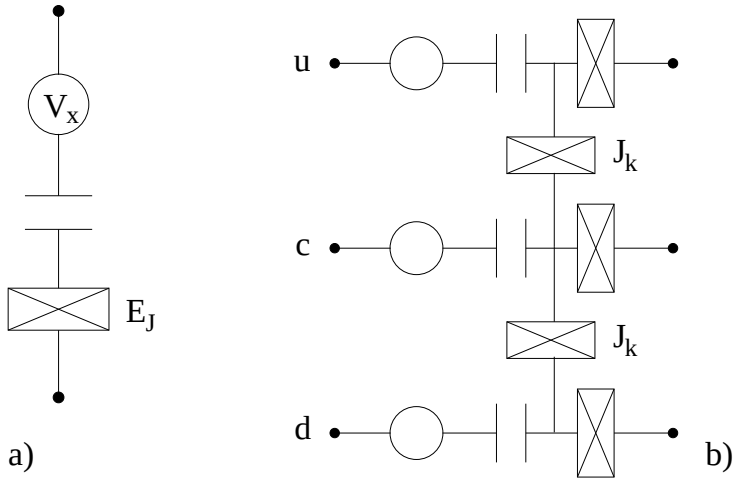

Figure 4.13: a) A sketch of the charge qubit. It consists of a superconducting electron box formed with an applied gate voltage V_x. The device operates in the charging regime, i.e. the Josephson couplings E_J of the junction (crossed box in the figure) is much smaller than the charging energy. b) Implementation of the $1 \rightarrow 2$ Spin Network Cloning by means of Josephson qubits. The unknown state to be cloned in stored in the central qubit c while the blank qubits u and d are the ones where the state is cloned. The coupling between the qubits is via the Josephson junctions of coupling energy J_K.

The system we consider is a Cooper pair box (see Fig.4.13a). This consists of a small superconducting island connected by a tunnel junction to a superconducting gate and connected to a voltage gate through a capacitor. The electrostatic Hamiltonian describing the system is:

$$H_0 = 4E_C(n - n_g)^2 - E_J \cos\phi \tag{4.49}$$

where n is the number of (extra) Cooper pairs on the island, $n_g = C_x V_x/2e$, E_C is the charging energy of the island, E_J is the Josephson energy and ϕ is the phase of the order parameter of the island. The two terms in the Hamiltonian represent respectively the electric energy of n Cooper pairs in the island and the Josephson tunneling energy across the junction. In the

charge regime ($E_C \gg E_J$) the eigenstates of the Hamiltonian are close to the states with definite n: $|n\rangle$. Close to degeneracy points, i.e. when n_g is half-integer, only two number states differing for one Cooper pair are relevant for the dynamics. This two levels define the charge qubit. The Hamiltonian in the qubit subspace can thus be rewritten as

$$H_0 = \delta E_C \sigma_z - E_J \sigma_x \tag{4.50}$$

where $\delta E_C = 4E_C(1 - 2n_g)$.

There are various ways to couple charge qubits, in order to implement SNC we couple the qubits via Josephson junctions [SFPS00] (see Fig.4.13b). The c qubit will encode the state to be cloned while the u and d qubits are initially in the blank state. All the Josephson junctions are assumed to be tunable by local magnetic fluxes. The total Hamiltonian of the 3-qubit system is given by the sum of the Hamiltonians H_0 of the qubits plus the interaction between them H_{cou}.

The coupling Hamiltonian for the 3-qubit system is

$$\begin{aligned} H_{cou} &= \sum_{i=u,d} E_K^{(i)} \sigma_z^{(c)} \sigma_z^{(i)} \\ &- (1/2) \sum_{i=u,d} J_K^{(i)} [\ \sigma_+^{(c)} \sigma_-^{(i)} + \text{h.c.}\ ] \end{aligned} \tag{4.51}$$

Here J_K is the Josephson energy of the junctions which couple the different qubits and $\sigma_\pm = (\sigma_x \pm i\sigma_y)/2$. If the coupling capacitance between the qubits is very small as compared to the other capacitances one can assume $E_K^{(j)}$ to be negligible. Since in practice the capacitive coupling is always present it is necessary to have $J_K^{(j)} \gg 4E_K^{(j)}$. Then the dynamics of the system approximates the ideal XY dynamics required to perform quantum cloning.

4.10 Conclusions

We have demonstrated that quantum cloning, in particular PCC, can be realized using no external control but just with an appropriate design of

the system Hamiltonian. We considered the Heisenberg and XY coupling between the qubits and we found that the XY model saturates the optimal value for the fidelity of the $1 \rightarrow 2$ PCC. In all other cases we have analyzed ($N \rightarrow M$ PCC, universal cloning, cloning of qudits) our protocol gives a value of the fidelity of clones that is always within a few percent to the optimal value. As compared to the standard protocol using quantum gates, however, there is a major advantage. Our setup is fast and, moreover, its execution time does not increase with the number of qubits to be cloned. In the presence of noise this allows to reach a much better fidelity than with the standard protocol already in the presence of a weak coupling to the external environment.

Chapter 5

Berry phase in open quantum systems: a quantum Langevin equation approach

In his seminal work [Ber84] Berry showed the appearance of a purely geometrical phase factor associated to the non degenerate eigenstates of a Hamiltonian undergoing a cyclic adiabatic evolution (see chapter 1).

Since the original discovery much work has been done to generalize Berry phase to non cyclic, non degenerate or non adiabatic evolution [SW89]. The renewed interest for geometric phases in a quantum computation scenario [JVEC00, ZR97, FFP$^+$00, FSF03, DCZ01, EEH$^+$00] is due to their supposed intrinsic fault tolerance. Such hypothesis is corroborated with this simple argument: since geometrical phases depend only on the area subtended by the path traversed by the control parameters (the magnetic field components, in the case of a spin 1/2), then small fluctuations in the parameters will leave the area unaffected.

This intrinsic robustness has been analyzed in [DCP03] for the case of a spin in a slowly varying magnetic field with small classical random fluctuations. There it was shown that for small fluctuations, i.e. to first order in the perturbation, and in the adiabatic limit the main source of decoherence are dynamical fluctuations. Similar conclusions have been reached for

quantum noise in [CFGSV02] by means of a quantum trajectories approach. In this chapter we analyze the problem using a quantum Langevin equation approach. Our system consists of a pseudospin interacting with a quantized bosonic field. The spin free Hamiltonian is assumed to undergo a slow cyclic evolution. The geometric phase appears in a natural way in terms of the so called adiabatic Hamiltonian [VW91, BP94]. Once such Hamiltonian is introduced the Heisenberg equations of motion are derived and from them the quantum Langevin equations. This approach allowed us to analyze the effects of the quantum fluctuations on both the decay constants and on the overall phase acquired by the spin energy eigenstates in their cyclic evolution. Similar questions have been addressed by some recent papers [WG03, WMSG05] where the effect of quantum fluctuations have been analyzed using the master equation formalism. We will show how our approach allows to obtain in a simple and straightforward way the corrections to the overall phase. Furthermore we will provide a simple physical picture of the results obtained. The effect of noise on geometric phases in different scenarios from the one described above has been studied in [BT03, NSM02].

This chapter is organized as follows: in Section 5.1 we introduce the model for the system and the environment and derive the adiabatic Hamiltonian. In Section 5.2 we derive the Langevin equations for the spin operators and in Section 5.3 we discuss the results for decay constants and energy shifts and give a geometric interpretation. Finally in Section 5.4 we summarize the results.

5.1 The adiabatic Hamiltonian

The system we consider consists of a pseudospin in a slowly varying static magnetic field interacting with an environment modeled as a bath of harmonic oscillators. The overall system Hamiltonian is assumed to be of the

standard form

$$\hat{H} = \frac{1}{2}\mathbf{B}\cdot\boldsymbol{\sigma} + \sum_k \omega_k \hat{a}_k^\dagger \hat{a}_k + \sum_k g_k \sigma_z \left(\hat{a}_k + \hat{a}_k^\dagger\right) \tag{5.1}$$

where $\boldsymbol{\sigma} \equiv (\sigma_x, \sigma_y, \sigma_z)$ are the Pauli operators and $\mathbf{B}(t) \equiv B_0(\sin\vartheta\cos\varphi, \sin\vartheta\sin\varphi, \cos\vartheta)$ is a three dimensional vector, which we assume to be time dependent and $\hat{a}_k^\dagger(\hat{a}_k)$ are bosonic creation (annihilation) operators for mode k.

The first step to obtain the Heisenberg equation of motion for the spin and bath operators is the introduction of the so called adiabatic Hamiltonian [VW91, BP94] i.e. of the Hamiltonian whose eigenstates, in the absence of interaction with the environment, after a cyclic evolution acquire the dynamical and geometrical phase predicted by Berry. Let us rewrite the free spin Hamiltonian in the form

$$\hat{H}_S \equiv \frac{1}{2}\mathbf{B}\cdot\boldsymbol{\sigma} = \frac{B_0}{2}\left(|\uparrow_n(t)\rangle\langle\uparrow_n(t)| - |\downarrow_n(t)\rangle\langle\downarrow_n(t)|\right) \tag{5.2}$$

where $|\uparrow_n(t)\rangle$ and $|\downarrow_n(t)\rangle$ are the eigenstates of $\hat{H}_S$ at time t i.e. they are the eigenstates of the operator $\boldsymbol{\sigma}\cdot\hat{\mathbf{n}}$ where $\hat{\mathbf{n}} \equiv (\sin\vartheta\cos\varphi, \sin\vartheta\sin\varphi, \cos\vartheta)$ is a unit vector pointing in the instantaneous $\mathbf{B}$ direction. Let us then define the following time dependent unitary operator:

$$U(t) = |\uparrow_n(0)\rangle\langle\uparrow_n(t)| + |\downarrow_n(0)\rangle\langle\downarrow_n(t)| \tag{5.3}$$

In the absence of any coupling with the environment the time evolution of the state vector $|\tilde{\psi}(t)\rangle = U(t)|\psi(t)\rangle$ is generated by the Hamiltonian

$$\hat{\tilde{H}}_S = U(t)\hat{H}_S U^\dagger(t) - iU(t)\frac{d}{dt}U^\dagger(t) \tag{5.4}$$

When the Hamiltonian varies slowly enough i.e. when the adiabatic approximation holds, we can set $\langle\uparrow(t)|\frac{d}{dt}|\downarrow(t)\rangle = 0$. This amounts to assume that transitions between states $|\uparrow_n(t)\rangle$ and $|\downarrow_n(t)\rangle$ are negligible. The adiabatic Hamiltonian is therefore

$$\begin{aligned}\hat{H}_S^{ad} &= \left(\tfrac{B_0}{2} - i\langle\uparrow_n(t)|\tfrac{d}{dt}|\uparrow_n(t)\rangle\right)|\uparrow_n(0)\rangle\langle\uparrow_n(0)| \\ &+ \left(-\tfrac{B_0}{2} - i\langle\downarrow_n(t)|\tfrac{d}{dt}|\downarrow_n(t)\rangle\right)|\downarrow_n(0)\rangle\langle\downarrow_n(0)|\end{aligned} \tag{5.5}$$

Note that when $\mathbf{B}$ undergoes a cyclic evolution the eigenstates of (5.5) correctly acquire the dynamical plus the geometrical phase predicted by Berry.

In the basis of the eigenstates of the σ_z operator we have

$$\begin{aligned}|\uparrow_n\rangle &= e^{-i\varphi/2}\cos\frac{\vartheta}{2}|\uparrow_z\rangle + e^{i\varphi/2}\sin\frac{\vartheta}{2}|\downarrow_z\rangle \\ |\downarrow_n\rangle &= e^{-i\varphi/2}\sin\frac{\vartheta}{2}|\uparrow_z\rangle - e^{i\varphi/2}\cos\frac{\vartheta}{2}|\downarrow_z\rangle\end{aligned} \tag{5.6}$$

from which it follows that

$$i\langle\uparrow_n(t)|\frac{\partial}{\partial t}|\uparrow_n(t)\rangle = -i\langle\downarrow_n(t)|\frac{\partial}{\partial t}|\downarrow_n(t)\rangle = \dot{\varphi}\frac{1}{2}\cos\vartheta \tag{5.7}$$

which is just the expression of the connection for the two eigenstates of the Hamiltonian.

The adiabatic Hamiltonian takes therefore the form

$$\hat{H}_S^{ad} = \frac{B_0 - \dot{\varphi}\cos\vartheta(t)}{2}\hat{\mathbf{n}}(0)\cdot\boldsymbol{\sigma} \tag{5.8}$$

For the sake of simplicity, and with no loss of generality, we will consider the case most discussed in literature in which $\mathbf{B}(\mathbf{t})$ precesses slowly with angular velocity $\Omega = 2\pi/T$ i.e. $\varphi(t) = \Omega t, \varphi(0) = 0, \vartheta(t) = \vartheta(0)$. Furthermore we will rotate our axis so that $[\cos\vartheta(0)\sigma_z + \sin\vartheta(0)\sigma_x] \to \sigma_z$ In this case the adiabatic Hamiltonian takes the following simple form

$$\hat{H}_S^{ad} = \frac{\omega_0}{2}\sigma_z \tag{5.9}$$

where $\omega_0 = B_0 + \Omega\cos\vartheta(0)$. The full, time independent, adiabatic spin - boson Hamiltonian then reads:

$$\hat{H} = \frac{\omega_0}{2}\sigma_z + \sum_k \omega(k)\hat{a}_k^\dagger\hat{a}_k + \sum_k g_k\left(\hat{a}_k + \hat{a}_k^\dagger\right)(\sigma_z\cos\vartheta - \sigma_x\sin\vartheta) \tag{5.10}$$

5.2 Langevin equations

The derivation of the quantum Langevin equations of motion for a two level systems coupled with a harmonic bath is well known in literature [CTDRG92, AE74]. Here, for the sake of clarity, we will sketch its main steps. The starting point are the Heisenberg equations of motion ($\dot{O} = i[\hat{H}, O]$) for the spin Pauli operators σ_z, $\sigma_+ = (\sigma_x + i\sigma_y)/2$ and the bath operators $\hat{a}_k, \hat{a}_k^\dagger$ which are

$$\dot{\sigma}_z = 2i \sin\vartheta \sum_k g_k \left(\sigma_+ - \sigma_-\right) \left(\hat{a}_k + \hat{a}_k^\dagger\right), \tag{5.11a}$$

$$\dot{\sigma}_+ = i\omega_0 \sigma_+ + i \sum_k g_k \left(\hat{a}_k + \hat{a}_k^\dagger\right) \left(\sin\vartheta \sigma_z + 2\cos\vartheta \sigma_+\right), \tag{5.11b}$$

$$\dot{\hat{a}}_k = -i\omega_k \hat{a}_k - i g_k \left(\cos\vartheta \sigma_z - \sin\vartheta(\sigma_+ + \sigma_-)\right). \tag{5.11c}$$

which can be cast in the following equivalent integral form

$$\sigma_z(t) - \sigma_z(0) = 2i \sin\vartheta \sum_k g_k \int_0^t \left(\sigma_+ - \sigma_-\right) \left(\hat{a}_k + \hat{a}_k^\dagger\right) dt', \tag{5.12a}$$

$$\sigma_+(t) - e^{i\omega_0 t}\sigma_+(0) = i \sum_k g_k \int_0^t e^{i\omega_0(t-t')} \left(\hat{a}_k + \hat{a}_k^\dagger\right) \left(\sin\vartheta \sigma_z + 2\cos\vartheta \sigma_+\right) dt', \tag{5.12b}$$

$$\hat{a}_k(t) - e^{-i\omega_k t}\hat{a}_k(0) = -i g_k \int_0^t e^{-i\omega_k(t-t')} \left(\cos\vartheta \sigma_z - \sin\vartheta \left(\sigma_+ + \sigma_-\right)\right) dt'. \tag{5.12c}$$

A standard assumption in the derivation of a quantum Langevin equation is that the timescale of the decay processes is much slower than the free evolution so that, in the above integrals, we can put

$$\sigma_z(t') = \sigma_z(t) \tag{5.13a}$$

$$\sigma_+(t') = e^{-i\omega_0(t-t')}\sigma_+(t) \tag{5.13b}$$

$$\hat{a}_k(t') = e^{i\omega_k(t-t')}\hat{a}_k(t). \tag{5.13c}$$

Eqs. (5.12) then become

$$\sigma_z = \sigma_z(0) + 2i\sin\vartheta \sum_k g_k \left[\sigma_+ \hat{a}_k \zeta^\star(\omega_0 - \omega_k) + \sigma_+ \hat{a}_k^\dagger \zeta^\star(\omega_0 + \omega_k) - \right.$$
$$\left. - \sigma_- \hat{a}_k \zeta(\omega_0 + \omega_k) - \sigma_- \hat{a}_k^\dagger \zeta(\omega_0 + \omega_k)\right], \tag{5.14a}$$
$$\sigma_+ = e^{i\omega_0 t}\sigma_+(0) + i\sin\vartheta \sum_k g_k \sigma_z \left[\hat{a}_k \zeta(\omega_0 + \omega_k) + \hat{a}_k^\dagger \zeta(\omega_0 - \omega_k)\right] +$$
$$+ 2i\cos\vartheta \sum_k g_k \sigma_+ \left[\hat{a}_k \zeta(\omega_k) + \hat{a}_k^\dagger \zeta^\star(\omega_k)\right], \tag{5.14b}$$
$$\hat{a}_k = e^{-i\omega_k t}\hat{a}_k(0) - i g_k \left[\cos\vartheta \sigma_z \zeta(\omega_k) - \sin\vartheta \left(\sigma_+ \zeta^\star(\omega_0 + \omega_k) + \sigma_- \zeta(\omega_0 - \omega_k)\right)\right]. \tag{5.14c}$$

where

$$\zeta(x) = \lim_{t\to\infty} \int_0^t e^{ixt'}\, dt' = P\frac{i}{x} + \pi\delta(x), \tag{5.15}$$

P denotes principal part and $\delta(x)$ is the Dirac delta function. The integration limit $t \to \infty$ is justified on the ground that we are interested at times $t \gg \omega_0^{-1}$.

By inserting Eqs.(5.14) into Eqs.(5.11) and taking care of a consistent choice of all operator products [CTDRG92, AE74], one obtains the desired equations of motion for the spin operator expectation value

$$\langle \dot{\sigma}_z \rangle = -2\sin^2\vartheta \left(\gamma_\perp \langle \sigma_z \rangle + \gamma_{\perp vac} \mathbb{1}\!\!1\right) - 2\sin 2\vartheta \gamma_\parallel \left(\langle \sigma_+ \rangle + \langle \sigma_- \rangle\right), \tag{5.16}$$
$$\langle \dot{\sigma}_+ \rangle = i\omega_0 \langle \sigma_+ \rangle + \sin 2\vartheta \xi \mathbb{1}\!\!1 - \frac{1}{2}\sin 2\vartheta (i\lambda + \gamma_\perp)\langle \sigma_z \rangle$$
$$+ \sin^2\vartheta \{(i\lambda - \gamma_\perp)\langle \sigma_+ \rangle - (+i\lambda + \gamma_\perp)\langle \sigma_- \rangle)\} - 4\cos^2\vartheta \gamma_\parallel \langle \sigma_+ \rangle, \tag{5.17}$$

where

$$\gamma_\perp = \pi \sum_k |g_k|^2 (2n_k + 1)\, \delta(\omega_0 - \omega_k) \tag{5.18}$$
$$\gamma_\parallel = \pi \sum_k |g_k|^2 (2n_k + 1)\, \delta(\omega_k) \tag{5.19}$$
$$\lambda = \sum_k |g_k|^2 (2n_k + 1) \left(\frac{P}{\omega_0 - \omega_k} + \frac{P}{\omega_0 + \omega_k}\right) \tag{5.20}$$
$$\xi = \frac{1}{2}\sum_k |g_k|^2 \left[i\left(\frac{2P}{\omega_k} - \frac{P}{\omega_0 - \omega_k} + \frac{P}{\omega_0 + \omega_k}\right) - \pi\delta(\omega_k - \omega_0)\right] \tag{5.21}$$

n_k is the mean number of photon in field mode k and $\gamma_{\perp vac}$ is $\gamma_\perp$ for $n_k = 0$.

5.3 Dissipation and energy shifts

The above equations allow us to clearly identify the effects of the adiabatic evolution on the physical quantities which characterize the spin dynamics, namely the decay constants and the energy shift. First of all let us consider the decay constant $\gamma_\parallel$ which describes the decoherence mechanism due to fluctuations "parallel" to the instantaneous direction of $\mathbf{B}$. As expected it is not modified by the adiabatic change of such direction. Furthermore the value of $\gamma_\parallel$ depends on the density of field modes at zero frequency which, in most situations of physical interest is equal to zero.

The decay constant $\gamma_\perp$ describes the dissipation mechanism due to the exchange of energy between system and bath and depends on the density of modes at the resonance frequency $\omega = \omega_0$. If we assume that the density of modes is a slowly varying function of ω near resonance, we can safely assume for very small Ω, i.e. in the adiabatic limit, $\sum_k |g_k|^2 (2n_k + 1)\, \delta(\omega_k - \omega_0) \approx \sum_k |g_k|^2 (2n_k + 1)\, \delta(\omega_k - B)$. This confirms that the timescale of dipole decay is not modified by the adiabatic evolution, a result which has been obtained with different techniques, from classical stochastic noise [DCP03], to quantum jump [CFGSV02]. We should point out that in order to observe the geometric phase we must have

$$\gamma_\perp \ll \Omega \ll \omega_0 \tag{5.22}$$

Let us consider now the change in the energy shift λ. In the adiabatic limit we must consider terms up to order $O(\Omega)$ and therefore

$$\begin{aligned}\lambda = \sum_k |g_k|^2 (2n_k + 1) \Bigg[&\left(\frac{P}{B_0 - \omega_k} + \frac{P}{B_0 + \omega_k} \right) \\ &+ \Omega \cos\vartheta \left. \frac{\partial}{\partial \omega_0} \right|_{\omega_0 = B} \left(\frac{P}{\omega_0 - \omega_k} + \frac{P}{\omega_0 + \omega_k} \right) \Bigg] \approx \lambda_0 + \delta\lambda. \end{aligned} \tag{5.23}$$

The quantity $\sin^2\vartheta\lambda_0$ is the Lamb Shift [CTDRG92, AE74], while

$$\delta\lambda = -\Omega\cos\vartheta\sum_k |g_k|^2(2n_k+1)\left[\frac{1}{(B_0-\omega_k)^2}+\frac{1}{(B_0+\omega_k)^2}\right] \tag{5.24}$$

gives information on the the effect of the quantum fluctuations on the geometric phase. This is in agreement with the result obtained by [WMSG05]. The observable overall phase difference between the two energy eigenstates at the end of their cyclic evolution, i.e. at time $T = 2\pi\Omega^{-1}$, will be

$$\Phi(T) = \Phi_D + \Phi_G \tag{5.25}$$

where the dynamical phase Φ_D

$$\Phi_D = \left[B_0 + \sin^2\vartheta\sum_k |g_k|^2(2n_k+1)\left(\frac{P}{B_0-\omega_k}+\frac{P}{B_0+\omega_k}\right)\right]T \tag{5.26}$$

is simply due to the renormalized energy splitting, while the geometric phase Φ_G is

$$\Phi_G = 2\pi\cos\vartheta\left\{1-\sin^2\vartheta\sum_k |g_k|^2(2n_k+1)\left[\frac{1}{(B_0-\omega_k)^2}+\frac{1}{(B_0+\omega_k)^2}\right]\right\}. \tag{5.27}$$

The expression (5.27) is amenable to a straightforward intuitive geometric interpretation. As we said before the Berry phase for a spin 1/2 is proportional to the solid angle spanned by the time varying magnetic field $\mathbf{B}$ on the Bloch sphere. As opposite energy eigenstates acquire opposite geometric phases the overall phase difference between them will be, for a slowly precessing field at an angle ϑ, equal to $\Phi_{\text{Berry}} = 2\pi\cos\vartheta$. In the presence of a weak coupling with the bosonic bath however each energy eigenstate will undergo virtual transitions, responsible for the Lamb Shift, with a probability

$$\text{Prob}_{\text{vt}} = \sin^2\vartheta\sum_k |g_k|^2(2n_k+1)\left[\frac{1}{(B_0-\omega_k)^2}+\frac{1}{(B_0+\omega_k)^2}\right]. \tag{5.28}$$

During such transition the spin state parallel (antiparallel) to the direction of the field $\mathbf{B}$ "jumps" to the antiparallel (parallel) spin state, acquiring an

opposite geometric phase. The overall geometric phase difference between the energy eigenstates will be therefore decreased by an amount proportional to Prob_{vt}, as shown in (5.27). Notice that the correction to the Berry phase is of order $O(g^2)$. In [DCP03], where the effects of classical noise were considered, no analogous correction was obtained because only contributions to first order in the fluctuating field were considered.

5.4 Conclusions

In this chapter we have shown how the corrections to the Berry phase and the decay constants for a spin 1/2 undergoing an adiabatic cyclic evolution can be obtained in terms of quantum Langevin equation once the adiabatic Hamiltonian is introduced. We have confirmed that the main source of decoherence is due only to the dynamical fluctuations, a result which has been obtained with different techniques, from classical stochastic noise [DCP03], to quantum jump [CFGSV02] and which emerges in a straightforward way in our approach. From the Langevin equations we have inferred the decay rates which are not modified by the adiabatic evolution. The Heisenberg equations of motion give also the correction to the geometric part of the overall phase difference between the energy eigenstates at the end of the cyclic evolution due to the coupling with the bath. We have also shown how such corrections are amenable to a straightforward geometrical interpretation.

Chapter 6

Phase diagram of spin-1 bosons on one-dimensional lattices

The experimental realization of optical lattices [AK98, CBF$^+$01, BCF$^+$01, MMC$^+$01] has paved the way to study strongly correlated many-particle systems with cold atomic gases (see e.g. the reviews [JZ05, MST$^+$04]). The main advantages with respect to condensed matter systems lie on the possibility of a precise knowledge of the underlying microscopic models and an accurate and relatively easy control of the various couplings. Probably one of the most spectacular experiments in this respect is the observation [GME$^+$02] of a Superfluid - Mott Insulator transition previously predicted in [JBC$^+$98] by a mapping onto the Bose-Hubbard model [FWGF89].

Optical lattices have received great attention from the quantum informa-

A quantum computer based on atoms in an optical lattice can be used not only for quantum computation but also for quantum simulations. This is reminiscent of Feynman's original vision [Fey82] and recently some realistic proposals have been put forward [GRMDC04]. It is indeed possible to simulate a variety of models of quantum spin chains and ladders. Different models can be realized by tuning electrical and magnetic fields applied to the atoms.

More recently the use of far-off-resonance optical traps, has opened the exciting possibility to study spinor condensates [SKK99]. Spin effects are enhanced by the presence of strong interactions and small occupation number, thus resulting in a rich variety of phases characterized by different magnetic ordering. For spin-1 bosons it was predicted that the Mott insulating phases have nematic singlet [DZ02] or dimerized [Yip03] ground state depending on the mean occupation and on the value of the spin exchange. Since the original paper by Demler and Zhou [DZ02] several works have addressed the properties of the phase diagram of spinor condensates trapped in optical lattices (see [

a dimerized phase.

6.1 The model and the numerical method

The effective Bose-Hubbard Hamiltonian, appropriate for $S = 1$ bosons, is given by

$$\begin{aligned}\hat{\mathcal{H}} &= \frac{U_0}{2}\sum_i \hat{n}_i(\hat{n}_i - 1) + \frac{U_2}{2}\sum_i \left(\hat{\mathbf{S}}_i^2 - 2\hat{n}_i\right) - \mu\sum_i \hat{n}_i \\ &- t\sum_{i,\sigma}\left(\hat{a}^\dagger_{i,\sigma}\hat{a}_{i+1,\sigma} + \hat{a}^\dagger_{i+1,\sigma}\hat{a}_{i,\sigma}\right) . \end{aligned} \tag{6.1}$$

The operator $\hat{a}^\dagger_{i,\sigma}$ creates a boson in the lowest Bloch band localized on site i and with spin component along the quantization axis σ: $\hat{n}_i = \sum_\sigma \hat{a}^\dagger_{i,\sigma}\hat{a}_{i,\sigma}$ and $\hat{\mathbf{S}}_i = \sum_{\sigma,\sigma'} \hat{a}^\dagger_{i,\sigma}\mathbf{T}_{\sigma,\sigma'}\hat{a}_{i,\sigma'}$ are the total number of particles and the total spin on site i ($\hat{\mathbf{T}}$ are the spin-1 operators). The first term in Hamiltonian (6.1) is the Hubbard repulsion between different atoms on the same site, the second term comes from the difference in energy between different spin configurations on the same site. In the third μ is the chemical potential which controls the mean number of particles in the system. Finally the fourth term proportional to t is responsible for the hopping of atoms between neighboring lattice sites with the same angular momentum.

Atoms residing on the same lattice site have identical orbital wave function and their spin function must be symmetric. This constraint imposes that $S_i + n_i$ must be even. The uniqueness of the completely symmetric state with fixed spin and number makes it possible to denote the single site states with $|n_i, S_i, S_i^z\rangle$ (S_i^z is the z-projection of the i-th spin). The coupling constants, which obey the following constraint

$$-1 < \frac{U_2}{U_0} < \frac{1}{2} ,$$

can be expressed in terms of the appropriate Wannier functions [ILD03].

From now on U_0 is set as the energy scale unit ($U_0 = 1$). Furthermore we discuss only the anti-ferromagnetic case ($0 < U_2 < 1/2$).

In the absence of spin dependent coupling a qualitative picture of the phase diagram can be drawn starting from the case of zero hopping ($t = 0$). The ground state is separated from any excited state by a finite energy gap. For finite hopping strength, the energy cost to add or remove a particle $\Delta E_{\pm}$ (excitation gap) is reduced and at a critical value $t_c^{\pm}(\mu)$ vanishes. This phase is named the Mott insulator (MI). For large hopping amplitudes the ground state is a globally coherent superfluid phase (SF). When the antiferromagnetic coupling U_2 is different from zero, states with lowest spins (compatible with the constraint $n_i + S_i =$ even) are favoured. This introduces an even/odd asymmetry of the lobes. More precisely, the amplitude of lobes with odd filling is reduced as compared with the lobes corresponding to even fillings [DZ02]. In the first lobe, for example, the extra energy required to have two particles on a site (instead of one) is $1 + 2U_2 - \mu$, thus lowering the chemical potential value where the second lobe starts. On the other hand, having no particles on a site gives no gain due to spin terms, accounting for the nearly unvaried bottom boundary of the lobe.

In order to determine the phase diagram of Eq.(6.1) we use the finite-size Density Matrix Renormalization Group (DMRG) with open boundary conditions [Whi92, Whi93]. The strategy of the DMRG is to construct a portion of the system (called the system block) and then recursively enlarge it, until the desired system size is reached. At every step the basis of the corresponding Hamiltonian is truncated, so that the size of the Hilbert space is kept manageable as the physical system grows. The truncation of the Hilbert space is performed by retaining the eigenstates corresponding to the m highest eigenvalues of the block's reduced density matrix (DMRG is extensively discussed in appendix B).

The DMRG has been employed, for the spinless case, in [KM98, KWM00]. The presence of the spin degree of freedom makes the analysis considerably more difficult. In the numerical calculations the Hilbert space for the on-site part of the Hamiltonian is fixed by imposing a maximum occupation number $\overline{n}_{max}$. As the first lobe is characterized by an insulating phase with

$n = 1$ particle per site we choose $\overline{n}_{max} = 3$ in this case. Already at this level the dimension of the Hilbert space per site becomes $d = 20$. We have checked, by increasing the value of $\overline{n}_{max}$, that this truncation of the Hilbert space is sufficient to compute the first lobe. In each DMRG iteration we keep up to $m = 300$ states in order to guarantee accurate results. The numerical calculations of the second lobe ($n = 2$ particles per site) have been performed with $\overline{n}_{max} = 4$ (which corresponds to a local Hilbert space of dimension $d = 35$). Using the DMRG algorithm with such large local site dimensions d is particularly time and memory consuming. It is thus necessary to take advantage of good quantum numbers. In our case both the total number of particle and the total angular momentum are conserved. Using these conserved operators we can label basis states according to their quantum numbers and rearrange the Hamiltonian in blocks of symmetry.

6.2 Phase Diagram

In the insulating phase the first excited state is separated by the ground state by a Mott gap. In the limit of zero hopping the gap is determined by the extra-energy $\Delta E_{\pm}$ needed to place/remove a boson at a given site. The finite hopping renormalizes the gap which will vanish at a critical value. Then the system becomes superfluid. This method has been employed for the spinless case by Freericks and Monien [FM96], and in [KM98, KWM00] where it was combined with the DMRG. Here we use it for the spinor case. Three iterations of the DMRG procedure are performed, with projections on different number sectors; the corresponding ground states give the desired energies E_0, $E_{\pm} = E_0 + \Delta E_{\pm}$. As target energies we used those obtained by the mapping of the Bose-Hubbard system into effective models as described in [ILD03]. We considered chains up to $L = 128$ sites for the first lobe, and $L = 48$ for the second lobe. The extrapolation procedure to extract the asymptotic values was obtained by means of linear fit in $1/L$, as discussed in [KWM00]. A comparison with a quadratic fit shows that $O(1/L^2)$ corrections are negligible

on the scale of Fig.6.1.

The plot of the phase diagram in the (μ, t) plane for different values of the spin coupling U_2 is shown in Fig.6.1. The first lobe tends to reduce its size on increasing the spin coupling; in particular the upper critical chemical potential at $t = 0$ is $\mu_c^+(0) = 1 - 2U_2$, while the t^* value of the hopping strength over which the system is always superfluid is suppressed as U_2 increases. On the other hand, the second lobe grows up when U_2 increases. This even/odd effect, predicted in [DZ02], is quantified in Fig.6.1. In the following we concentrate on the first Mott lobe.

6.3 Magnetic properties of the first Mott lobe

The first lobe of the spinor Bose lattice has a very interesting magnetic structure. In the presence of small hopping t boson tunneling processes induce effective pairwise magnetic interactions between the spins described by the Hamiltonian [ILD03]

$$\hat{\mathcal{H}}_{eff} = \kappa \sum_{\langle ij \rangle} \left[\cos\theta \, (\hat{\mathbf{S}}_i \cdot \hat{\mathbf{S}}_j) + \sin\theta \, (\hat{\mathbf{S}}_i \cdot \hat{\mathbf{S}}_j)^2 \right] \tag{6.2}$$

with

$$\tan\theta = \frac{1}{1 - 2U_2} \qquad \kappa = \frac{2t^2}{1 + U_2} \sqrt{1 + \tan^2\theta} \ . \tag{6.3}$$

The absence of higher order terms, such as $(\hat{\mathbf{S}}_i \cdot \hat{\mathbf{S}}_j)^3$, is due to the fact that the product of any three spin operators can be expressed via lower order terms. In the case of anti-ferromagnetic interaction in Eq.(6.1), the parameter θ varies in the interval $\theta \in [-3/4\pi, -\pi/2[$. Because of the form of the magnetic Hamiltonian, each bond tends to form a singlet-spin configuration, but singlet states on neighbouring bonds are not allowed. There are two possible ground states that may appear in this situation. A nematic state can be constructed by mixing states with total spin $S = 0$ and $S = 2$ on each bond. This construction can be repeated on neighbouring bonds, thereby preserving trans-

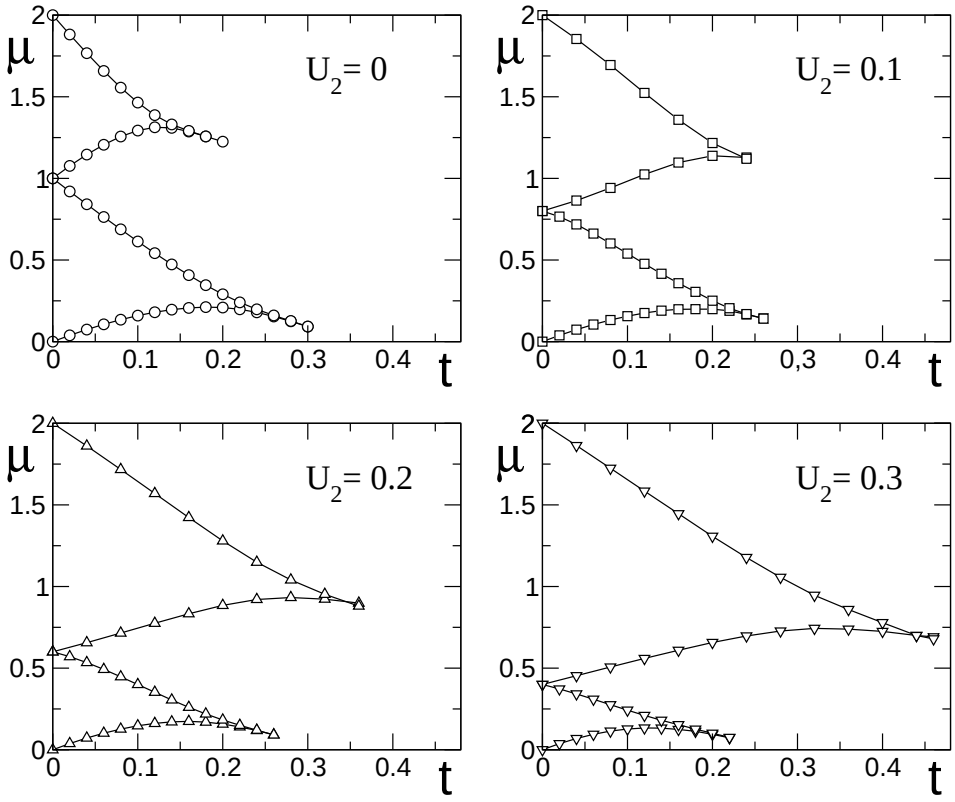

Figure 6.1: Phase diagram in the (μ, t) plane for the first two lobes of the one-dimensional Bose-Hubbard spin 1 model with nearest-neighbour interactions. The different panels correspond to different values of U_2: $U_2 = 0$ (upper-left), 0.1 (upper-right), 0.2 (lower-left), 0.3 (lower-right). The curves for $U_2 = 0$ coincide with the first two lobes for the spinless model computed in Refs. [KM98, KWM00].

lational invariance. This state breaks the spin-space rotational group $O(3)$, though time-reversal symmetry is preserved. The expectation value of any spin operator vanishes ($\langle \hat{S}_i^\alpha \rangle = 0,\ \alpha = x, y, z$), while some of the quadrupole operators have finite expectation values. The tensor $\mathcal{Q}^{ab} = \langle \hat{S}^a \hat{S}^b \rangle - \frac{2}{3}\delta^{ab}$ is a traceless diagonal matrix, due to invariance under spin reflections. Since it has two identical eigenvalues ($\langle (\hat{S}_i^x)^2 \rangle = \langle (\hat{S}_i^y)^2 \rangle \neq \langle (\hat{S}_i^z)^2 \rangle$), it can be written as $\mathcal{Q}^{ab} = Q\left(d^a d^b - \frac{1}{3}\delta^{ab}\right)$ using an order parameter $\langle \hat{Q} \rangle \equiv \langle (\hat{S}_i^z)^2 \rangle - \langle (\hat{S}_i^x)^2 \rangle = \frac{3}{2}\langle (\hat{S}_i^z)^2 \rangle - 1$ and a unit vector $\mathbf{d} = \pm\mathbf{z}$. However, since $[\hat{Q}, \hat{\mathcal{H}}_{eff}] = 0$, it is not possible to get $Q \neq 0$ in finite size systems, analogously to what happens for the magnetization without external field. Therefore we characterized the range of nematic correlations in the ground state by coupling this operator to a fictitious "nematic field"

$$\hat{\mathcal{H}}_\lambda = \hat{\mathcal{H}}_{eff} + \lambda \hat{Q}$$

and then by evaluating the nematic susceptibility χ_{nem} as a function of the system size:

$$\chi_{nem} \equiv -\left.\frac{\mathrm{d}^2 E_0(\lambda)}{\mathrm{d}\lambda^2}\right|_{\lambda=0} = \sum_\gamma \frac{|Q_{0,\gamma}|^2}{E_\gamma - E_0}\,, \tag{6.4}$$

where $E_0(\lambda)$ is the ground energy of $\hat{\mathcal{H}}_\lambda$, $Q_{0,\gamma}$ is the matrix element between the ground and an excited state of $\hat{\mathcal{H}}_{eff}$ (respectively with energy E_0 and E_γ).

On the other hand a possibility to have $SO(3)$ symmetric solution stems from breaking translational invariance. Indeed, a dimerized solution with singlets on every second bond satisfy these requirements. Dimerization could be described looking at the differences in expectation values of the pair Hamiltonian $\hat{\mathcal{H}}_{eff}^{(ij)}$ on adjacent links ($\hat{\mathcal{H}}_{eff} = \sum_{\langle ij \rangle} \hat{\mathcal{H}}_{eff}^{(ij)}$). On any finite chain some inhomogeneity exists, thus leading to a finite D_L even if $D = 0$. Quantitatively, an order parameter D_L could be defined by evaluating Eq. (6.5) in the middle of the finite size chain. The order parameter D has to be extrapolated in the thermodynamic limit: $D \equiv \lim_{L\to\infty} D_L$. The order parameter D reads

$$D \equiv \left| \langle \hat{\mathcal{H}}_{eff}^{(i-1,i)} - \hat{\mathcal{H}}_{eff}^{(i,i+1)} \rangle \right|. \tag{6.5}$$

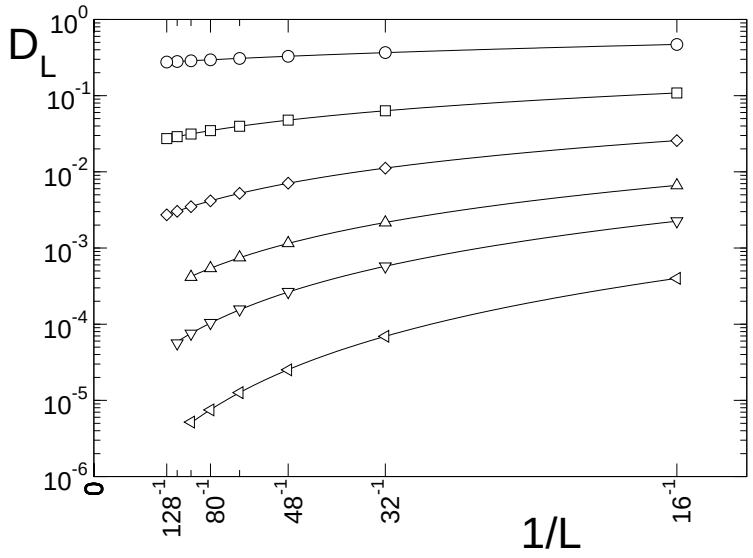

Figure 6.2: Finite size scaling of D_L for selected values of θ: circles ($\theta = -0.65\pi$), squares (-0.7π), diamonds (-0.72π), triangles up (-0.73π), triangles down (-0.735π), triangles left (-0.74π). In order to extrapolate the order parameter D, numerical data have been fitted with $D_L = D + cL^{-\alpha}$ (straight lines). DMRG simulations are performed with $m \simeq 140$ for $\theta > -0.73\pi$, and $m \simeq 250$ for $\theta \leq -0.73\pi$.

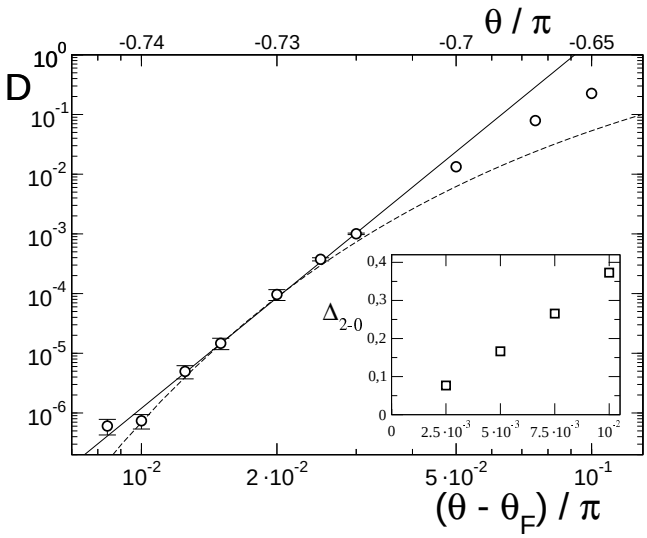

Figure 6.3: Behaviour of the dimerization order parameter D of Eq. (6.5) near the ferromagnetic boundary: solid line shows a power law fit $D \sim (\theta - \theta_F)^\gamma$ of numerical data with an exponent $\gamma \simeq 6.15$; dashed line shows an exponential law fit $D \sim \exp[-a/(\theta - \theta_F)^{-1/2}]$ with $a \simeq 2.91$. The linear fit is done over data for $\theta < -0.7\pi$, while the exponential fit is for $\theta \leq -0.73\pi$. DMRG calculations are performed with up to $m \simeq 300$ states. The inset shows the extrapolated scaled gap $\Delta_{2-0} = (L-1)(E_2 - E_0)$ at the thermodynamic limit, for some points at $\theta \leq -0.74\pi$.

It has been proposed [Chu91] that a narrow nematic region exists between the ferromagnetic phase boundary ($\theta_F = -3\pi/4$, i.e. $U_2 = 0$) and a critical angle $\theta_C \approx -0.7\pi$ (i.e. $U_2 \sim 10^{-2}$), whereas a dimerized solution is favoured in the remaining anti-ferromagnetic region $\theta_C \leq \theta \leq -\pi/2$. This implies that the dimerization order parameter D should scale to zero in the whole nematic region. This possibility has been analyzed in Ref. [FS95] where it was suggested that D might go to 0 in an exponential way near the ferromagnetic boundary, making it difficult to detect the effective existence of the nematic phase. This interesting challenge has motivated numerical investigations with different methods [FS95, Kaw02, PVC05, LST03]. Here we present new DMRG results which, in our opinion, clarify the magnetic properties of the first Mott lobe (for sufficiently small hopping) and consequently of the

Heisenberg chain with biquadratic interaction.

According to our numerical calculation there is *no* intermediate nematic phase, indeed we found a power law decay of the dimerization order parameter near $\theta_F = -3\pi/4$. The simulations of the bilinear-biquadratic model (6.2) are less time and memory consuming than Bose-Hubbard ones, since the local Hilbert space has a finite dimension $d = 3$. The number of block states kept during the renormalization procedure was chosen step by step in order to avoid artificial symmetry breaking. This careful treatment insures that there are no spurious sources of asymmetry like partially taking into account a probability multiplet. Here we considered up to $m \simeq 300$ states in order to obtain stable results. Raw numerical data are shown in Fig.6.2, where the finite size dimerization parameter $D(L)$ is plotted as a function of the chain length L (see Eq. 6.5). Finite size scaling was used to extrapolate to the thermodynamic limit. After the extrapolation to the $L \to \infty$ limit, see Fig. 6.3, we fitted the dimer order parameter with a power law

$$D = \left(\frac{\theta - \theta_F}{\theta_0} \right)^{\gamma} \tag{6.6}$$

where $\gamma \sim 6.1502$ and $\theta_0 \sim 0.09177\,\pi$ (Fig. 6.3, solid line). We also tried to fit our data by an exponential law of the form

$$D = D_0\, e^{-a/\sqrt{\theta - \theta_F}} \tag{6.7}$$

as suggested in [FS95], with $a \sim 2.911$, $D_0 \sim 9.617$; this fit seems to work for narrower regions (Fig. 6.3, dashed line), however from our numerics we cannot exclude an exponential behaviour of D in the critical region. The dimerized phase thus seems to survive up to the ferromagnetic phase boundary, independently from the chosen fitting form. This is also confirmed by the fact that the scaled gap between the ground state E_0 and the lowest excited state E_2 (which is found to have total spin $S_T = 2$) seems not to vanish in the interesting region $\theta > -0.75\pi$ (see the inset of Fig. 6.3). To further characterize the behaviour of the system we analyzed the susceptibility of the chain to nematic ordering χ_{nem}. The numerical data, presented in

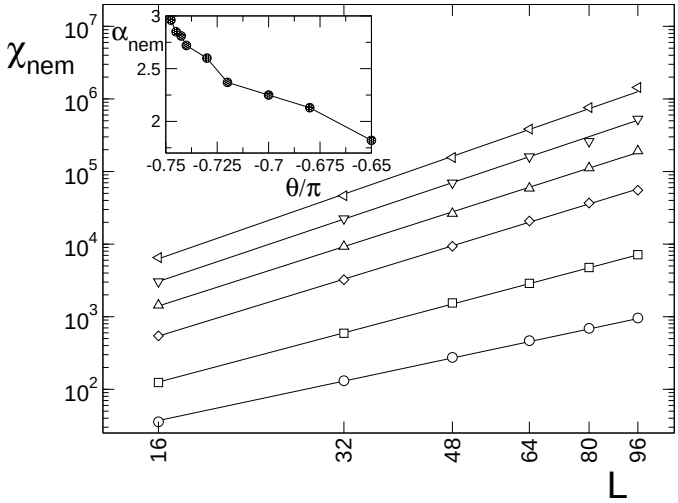

Figure 6.4: Nematic susceptibility χ_{nem} as a function of the system size L. The various symbols refer to different values of θ: circles ($\theta = -0.65\pi$), squares (-0.7π), diamonds (-0.73π), triangles up (-0.74π), triangles down (-0.745π), triangles left (-0.7475π). Straight lines are the result of a power law fit $\chi_{nem} = cL^{\alpha}$ of numerical data. In the inset the exponent α is plotted as a function of θ.

Fig. 6.4, show a power law behaviour $\chi_{nem}(L) \propto L^{\alpha}$ as a function of the system size. The exponent α (shown in the inset) approaches the value $\alpha = 3$ as $\theta \to \theta_F$. This can also be confirmed by means of a perturbative calculation around the exact solution available at θ_F; indeed one obtains $|Q_{0,\gamma}|^2 \sim L^2$ and $(E_\gamma - E_0) \sim L^{-1}$ to be inserted in Eq. (6.4). The increase of the exponent for $\theta \to \theta_F$ indicates, as suggested in [PVC05], that a tendency towards the nematic ordering is enhanced as the dimer order parameter goes to zero. We conclude this chapter by remarking that our results indicate that the Mott insulator is *always* in a dimerized phase.

Chapter 7

A scheme for entanglement extraction from a solid

It was a common belief that entanglement cannot exist on a macroscopic scale. This is because decoherence effects from many particles interaction would destroy all quantum correlations. However it has been predicted that macroscopic entanglement can exist in solids in the thermodynamical limit [GRAC03] even at high temperature [Ved04]. In a typical magnetic solid the orbitals of electrons in different atoms overlap and because of the Coulomb interaction this gives rise to the exchange interaction between spins. The interaction between spin degrees of freedom is therefore described by a Heisenberg Hamiltonian whose thermal states are entangled [ABV01]. There are many works inferring the existence of macroscopic entanglement at various temperatures up to room temperature. The evidence comes from experiments measuring different thermodynamic properties such as magnetic susceptibility and heat capacity [BV04, BVZ04, VB05]. Until now however it was not clear whether this entanglement can be useful as a resource in quantum computation. The crucial question therefore is: can this macroscopic entanglement in solids be extracted? In particular, can this entanglement be transferred to a pair of particles and subsequently used for quantum computation or to violate Bells's inequalities? Here we propose an experimental setup to demonstrate entanglement extraction with present-day technology

using optical lattices. In this chapter we show that this entanglement can be extracted and therefore used for quantum information processing. This makes macroscopic entanglement a physical resource extractable from solids in the same way as heat can be exchanged between different systems and used for work in thermodynamics.

In the next two paragraphs we outline the basic idea behind our proposal which is then elaborated in the remaining part of the chapter.

The entanglement of a pair of spins inside a solid can be transferred to another pair of probe particles using only local swap operations. We need to send simultaneously two probes toward entangled spins in a chain such that each probe interacts with different sets of spins (cf. Fig.7.1). We emphasize that the two probes will not interact with each other nor will they experience an interaction mediated by the solid (cf. [Bra02]). The entanglement between the probes has been transferred from the spin chain and cannot exist without entanglement in the chain. This is a genuine non local process between the two probes like in the case of entanglement swapping [ZZHE93]. We mention that in the continuum limit our procedure can be used to extract entanglement from vacuum (some steps in this direction have been taken by [RCR05]). The scattering interaction between probes and spins must be capable of (at least partially) swapping their state. This is the case of very common interactions like Heisenberg or XY. It could happen that after one scattering event entanglement swapping is only partial. In this case it is interesting to investigate whether by repeating this collision procedure many times the entanglement between the two probes can increase.

7.1 The model

Let us now introduce the detailed description of the interaction between the probes and the spins in the solid. All aspects of this analysis can be implemented with different quantum systems: it is necessary that individual

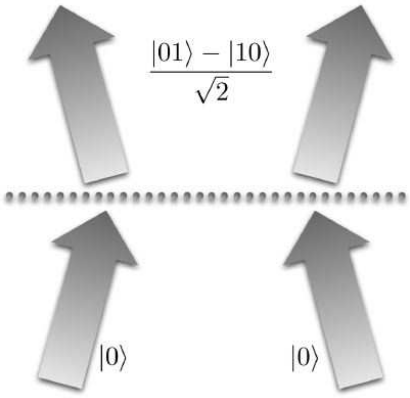

Figure 7.1: Schematic drawing of the entanglement extraction process. Two probe particles initially prepared in a product state are sent toward a solid whose spins are entangled. Each probe interacts with only one spin in the solid. During the collision, due to the exchange interaction between probe and spin, their state is swapped. The two probes come out from the solid in an entangled state.

probe particles can be coherently sent to interact with the spin chain. In Sec. 7.3 we propose to simulate the extraction process with optical lattices. Two probes are sent toward a spin chain in a solid. We assume initially that each of the probes interact with a single spin in the chain as shown in Fig. 7.1. We suppose that the interaction Hamiltonian is given by an anisotropic XXZ model between probe $i = L, R$ and spin $j = 1, 2$:

$$H(\lambda)_{ij} = J\left(\sigma_x^i \sigma_x^j + \sigma_y^i \sigma_y^j + \lambda \sigma_z^i \sigma_z^j\right) \tag{7.1}$$

where $\sigma_{x,y,z}$ are the Pauli matrices. We assume that the coupling J is constant during the collision that lasts for a time τ. The total Hamiltonian is therefore $H_T = H(\lambda)_{1L} + H(\lambda)_{2R}$. This Hamiltonian comes from the same exchange mechanism that gives rise to the interaction between spins in the solid. We will concentrate on two important limits: $\lambda = 1$, which is the Heisenberg (exchange) interaction; $\lambda = 0$, the XY interaction. The initial state of the pair of spins in the solid is assumed to be a mixed state. We consider two possibilities for the form of the density matrix of the two spins.

The first possibility is to consider a Werner state, often encountered in many situations in quantum information theory [Wer89]. The second is to consider the reduced density matrix of two spins of a XXZ chain in terms of the spin-spin correlation functions.

7.1.1 Werner state

Here we suppose that the entangled pair of spins in the solid is in a Werner state described by the density matrix:

$$\rho_W = \frac{\eta}{4}\mathbb{1} + (1-\eta)|\psi^-\rangle\langle\psi^-| \tag{7.2}$$

where $|\psi^-\rangle = 2^{-1/2}(|01\rangle - |10\rangle)$ is the singlet state and $0 \leq \eta \leq 1$. This state is entangled when the mixedness parameter $0 \leq \eta < 2/3$. Werner states are mixtures of symmetric and antisymmetric subspaces and naturally arises in systems of indistinguishable particles, i.e. solids.

Let us first consider what happens in a collision between the probes in a pure product state e.g. $|00\rangle$ and the spins in a maximally entangled state $\eta = 0$ when $\lambda = 1, 0$. After the collision the global state of the four particle reads (apart from a global phase factor):

$$|\Psi(t)\rangle = \cos 2J\tau|00\rangle_{LR}|\psi^-\rangle_{12} - i\sin 2J\tau|\psi^-\rangle_{LR}|00\rangle_{12}. \tag{7.3}$$

This state is a superposition of the initial state and of the swapped state. By tracing out the two spins one obtains the reduced density matrix ρ_{LR} of the two probes. We use the concurrence [Woo98] to measure the extracted entanglement. The concurrence for the two probes is simply $C = \sin^2 2J\tau$ and is equal to 1 when $J\tau = \pi/4$. Thus no matter how small τ is, it is still possible to extract some entanglement from the singlet state.

When $\eta > 0$ the global state is mixed and the concurrence for $\lambda = 0, 1$ is plotted in Fig. 7.2. As it is shown in the plot the entanglement between probes decays with η which represents the mixedness of the initial state of the spins. This is an intuitively expected result because the higher mixedness

of the spins implies that there is less entanglement and this in turn means that less can be transferred to the probes. The full SWAP transformation between spins and the probes is obtained when $J\tau = \pi/4$ and the entanglement extracted is maximum. We also note that entanglement oscillates with τ which reflects the fidelity of the SWAP operation. The state is always entangled for $\eta < (3 - \sqrt{5})/2 \simeq 0.38$ no matter how small τ is. However when $(3 - \sqrt{5})/2 < \eta < 2/3$, τ must be chosen appropriately as shown in Fig. 7.2 in order to obtain some entanglement. Notice that no entanglement can be extracted for $\eta \geq 2/3$ when the two spins are not entangled. This result for entanglement has been maximized among product states of the two qubits. We can infer from Fig. 7.2 that whenever the state of the spins is entangled ($\eta < 2/3$) our procedure is capable of transferring entanglement to the probes.

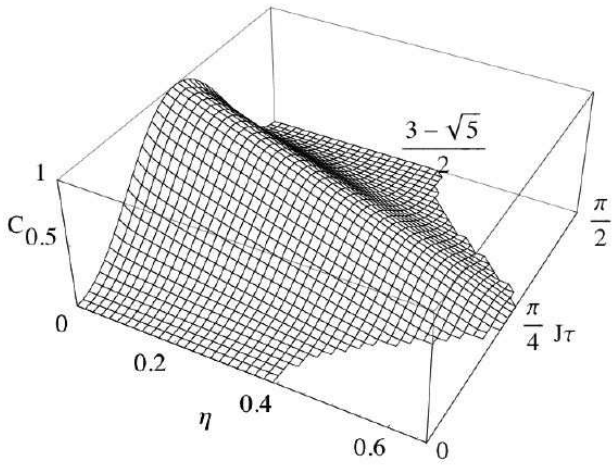

Figure 7.2: Entanglement, measured by the concurrence C, of the two probes after one collision as a function of η and τ. Notice how C decays with the mixedness η and oscillates with the time of interaction τ.

7.1.2 Ground state of the XXZ model

Since Werner state is not the most general mixed entangled state for two spins, here we suppose that the global state of the chain is the ground state of the XXZ spin chain. The reduced density matrix of the entangled pair can be written in terms of spin-spin correlation functions by using translational invariance and conservation of angular momentum. The full derivation is presented in [AOP+04] and the result is:

$$\rho = \begin{pmatrix} \frac{1}{4}+g_{zz} & 0 & 0 & 0 \\ 0 & \frac{1}{4}-g_{zz} & 2g_{xx} & 0 \\ 0 & 2g_{xx} & \frac{1}{4}-g_{zz} & 0 \\ 0 & 0 & 0 & \frac{1}{4}+g_{zz} \end{pmatrix} \tag{7.4}$$

where $g_{zz} = \langle\sigma_z\sigma_z\rangle/4$ and $g_{xx} = \langle\sigma_x\sigma_x\rangle/4$ are spin-spin correlation functions and can be numerically estimated for the Heisenberg model. The concurrence of ρ, assuming $|g_{xx}| \geq g_{zz}$, is:

$$C = \mathrm{Max}[0, -\frac{1}{2} + 4\,|g_{xx}| - 2g_{zz}] \tag{7.5}$$

We numerically evaluated the concurrence for $\lambda = 1$ and $g_{xx} = g_{zz}$ which is plotted in Fig. 7.3. The correlation function g gives a direct physical information on the entanglement stored in the chain even at temperature different from zero. As it is shown in the plot the entanglement between probes decays when g_{zz} decreases, i.e. when the initial entanglement of the spin pair is less. As before the full SWAP is obtained when $J\tau = \pi/4$ and the entanglement extracted is maximum. Again the entanglement oscillates with τ. The state is always entangled for $g_{zz} \lesssim -0.16$ no matter how small τ is. However when $-0.16 < g_{zz} < -1/12$, τ must be chosen appropriately as shown in Fig. 7.3 in order to obtain some entanglement. This result for entanglement has been maximized among product states of the two qubits. We can infer from Fig. 7.3 that whenever the state of the spins is entangled ($g_{zz} < -1/12$) our procedure is capable of transferring entanglement to the probes. Similar results applies also to the XY model $\lambda = 0$.

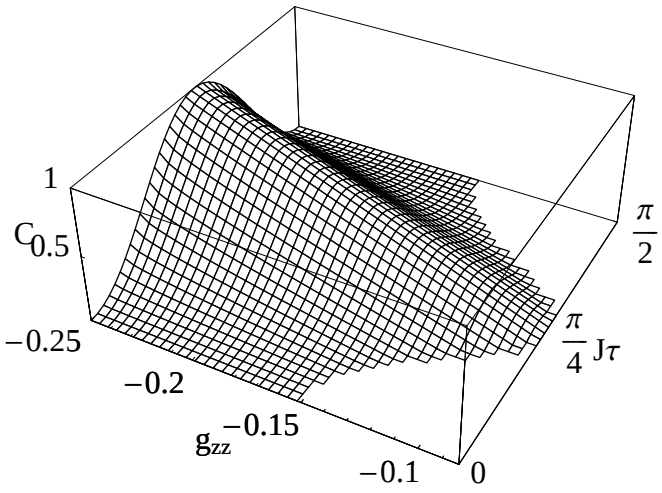

Figure 7.3: Entanglement, measured by the concurrence C, of the two probes after one collision as a function of g_{zz} and τ. Notice how C increases with the correlation g_{zz} and oscillates with the time of interaction τ.

7.2 Repeated collisions

Once τ is fixed for a specific experimental setup the amount of entanglement extracted is less than the entanglement in the pair of spins as long as $J\tau < \pi/4$. Is it possible to extract *more* entanglement by repeating the collision process *many* times [SZS+02]? At first sight it seems that this is related to the homogenization process [SZS+02], however we cannot use their results because the transformation induced by the interaction Hamiltonian (7.1) is not a global partial SWAP transformation. Indeed with a local interaction generated by the spin Hamiltonian ($\lambda = 1$) the full transformation of the four spins is:

$$U_{12LR} = PSW_{1L} \otimes PSW_{2R}, \quad \text{where} \tag{7.6}$$

$$PSW = e^{iJt}\left(\cos 2Jt\, \mathbb{1} - i \sin 2Jt\, SWAP\right), \quad \text{and} \tag{7.7}$$

$$SWAP = |00\rangle\langle 00| + |01\rangle\langle 10| + |10\rangle\langle 01| + |11\rangle\langle 11| \quad \text{swaps two qubits.} \tag{7.8}$$

The transformation PSW is called *partial swap* and has been analyzed in [SZS+02]. Here the authors are interested in modeling the decoherence process induced by a bath with a collision setup. The environment is constituted by a set of spins all in a state $|\chi\rangle$ and they want to study the decoherence process of a qubit initially prepared in a different state $|\psi\rangle$. At each collision the qubit interact for a time τ with a single spin and its reduced density matrix ρ_n after n collisions is:

$$\rho_n = \mathrm{Tr}\left(U\rho_{n-1}|\chi\rangle\langle\chi|U^\dagger\right) \tag{7.9}$$

Using the Banach-Caccioppoli theorem about the fixed point of the contractive map U, in [SZS+02] it can be shown that for each initial state $|\psi\rangle$ the state of the qubit approaches that of the bath: $\rho_n \to |\chi\rangle\langle\chi|$ for $n \to \infty$. The theorem applies not just to qubits but to arbitrary finite dimension systems as for example two qubits. In our case however the theorem does not apply because the transformation considered (7.6) is the tensor product of two swap operations and not a swap operation of the systems $\{12\} \leftrightarrow \{LR\}$. For this reason it is not expected in general that the fixed point, if any, of U_{12LR} will be the initial state of LR.

It is easy to demonstrate that the state $|\psi^+\rangle_{LR}|\psi^-\rangle_{12}$ is an eigenstate of H_T with $\lambda = 0$ (XY model). It is thus a fixed point of the evolution transformation and the state of the probes will approach the state $|\psi^+\rangle$ as the number of collisions goes to infinity, independently of the input state and of how small τ is. This is a counter-intuitive result: the state of the probes do not converge to the state of the bath but to an orthogonal state. The reason is that XY interaction does not generate a partial SWAP operation but something similar to a partial iSWAP operation:

$$iSWAP = |00\rangle\langle 00| + i|01\rangle\langle 10| + i|10\rangle\langle 01| + |11\rangle\langle 11| \tag{7.10}$$

that swaps the state of the two qubits but with a i factor. The composition of two of these transformation produces a minus sign that transform ψ^+ in ψ^-. The same holds for the pair $\phi^\pm$. In Fig. 7.4 we show how the concurrence

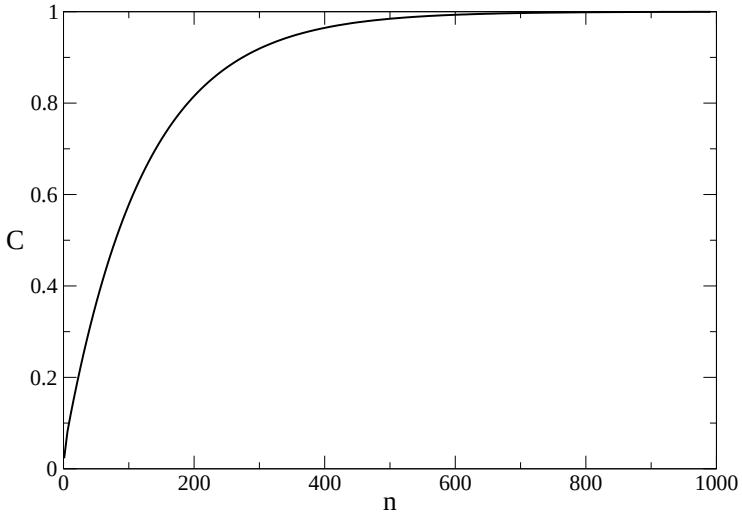

Figure 7.4: Concurrence between the probes as a function of the number of collisions. We supposed the initial state (7.2) with $\eta = 0$ and $J\tau = 0.2$. The data are well described by the fit function $C(n) = 1 - \exp(-\kappa n)$ where $\kappa = -8.3\ 10^{-3}$.

grows increasing the number of collision with the spins. For $\lambda = 1$ (Heisenberg model) there is not an eigenstate of the total Hamiltonian that is the tensor product of a maximal entangled state of the probes times a maximal entangled state of the two spins.

Let us come back to $\lambda = 0$. When $\eta > 0$ the transformation has still a fixed point whose entanglement depends on η and τ. We want to emphasize that even if the maximum entanglement can not be achieved, the many-collision scheme is capable of extracting some entanglement. This is illustrated in Fig 7.5.

We can modify the interaction between the four spins $1, 2, L, R$ in order to fulfill the hypothesis of Banach-Caccioppoli theorem: it is sufficient to build a Hamiltonian that generates a global SWAP transformation:

$$PSW_{1L,2R} = e^{iJt}\left(\cos 2Jt\, \mathbb{1}_{1L} \otimes \mathbb{1}_{2R} - i \sin 2Jt\, SWAP_{1L} \otimes SWAP_{2R}\right) \tag{7.11}$$

This can be found by inspection and reads in the computational basis of

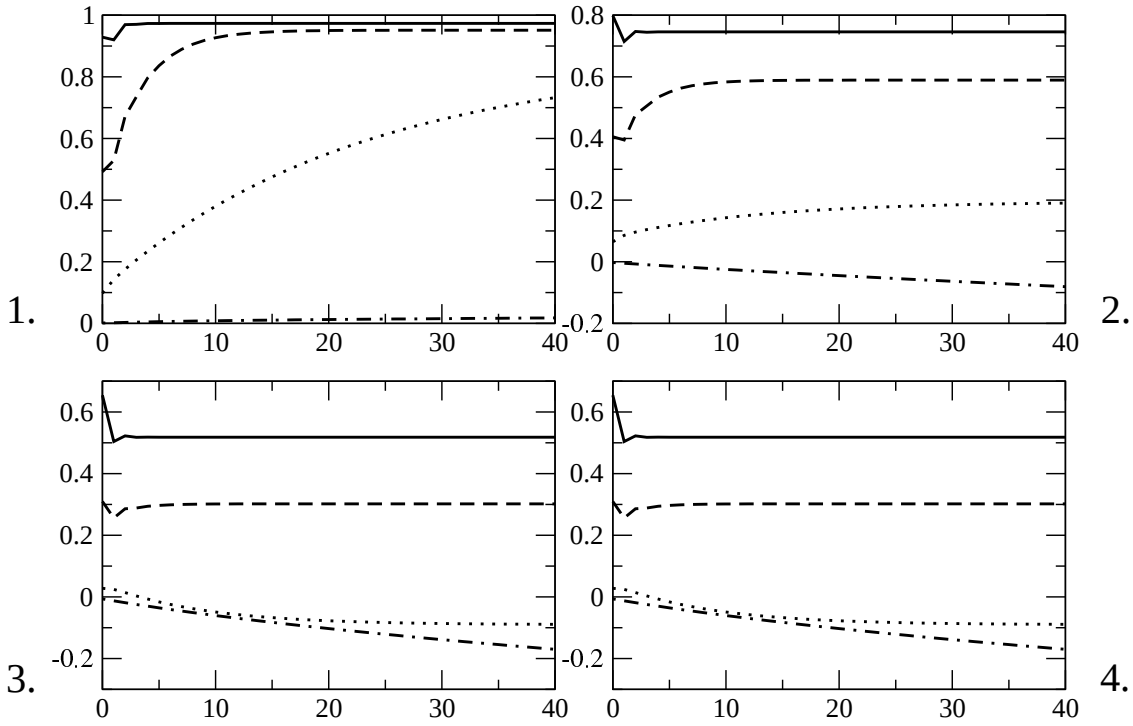

Figure 7.5: Concurrence between the probes as a function of the number of collisions n for various values of $\eta = 0.01, 0.1, 0.2, 0.4$ (plots 1., 2., 3. ,4. respectively) and $\tau = 0.1$ (dot-dashed), 0.3 (dotted), 0.5 (dashed), 0.7 (solid).

$12LR$:

$$\begin{aligned} H_{12LR} &= |0000\rangle\langle 0000| + |0101\rangle\langle 0101| + |1010\rangle\langle 1010| + |1111\rangle\langle 1111| \\ &+ |0001\rangle\langle 0100| + |0010\rangle\langle 1000| + |1011\rangle\langle 1110| + |1101\rangle\langle 0111| \\ &+ |0011\rangle\langle 1100| + |1001\rangle\langle 0110| + h.c. \end{aligned} \tag{7.12}$$

Notice that the elements of the first two rows can be generated by pairwise interactions as in (7.1). The elements of the third row instead are four spin processes. With this interaction it is possible to demonstrate that the probes state will approach the state of the spins no matter the initial state.

7.3 Extraction of entanglement in optical lattices

The most natural way to extract entanglement from entangled spins in solids would be to scatter pairs of neutrons off the solid. We will present a proposal for simulation of this process of entanglement extraction with optical lattices [GME$^+$02] that we hope can be implemented in the near future. Optical lattices are a very useful tool for simulating many quantum effects in solids and have been employed in demonstrating quantum phase transition [GME$^+$02], Bose-Einstein condensation [GMHB02] and quantum gates [MGW$^+$03] (see also chapter 6). For our purposes we need to simulate both the interaction in the solid system as well as the interaction with the external probes. Hamiltonians of entangled spin chains or ladders can be realized using cold neutral atoms trapped in potential wells generated by counter-propagating lasers [GRMDC04, DDL03, GRC03]. Bosonic atoms (black in Fig. 7.6), loaded onto the lattice, can be described by means of the Bose-Hubbard model (see Chapter 6). For our proposal we assume that the system is in the Mott insulator phase with only one atom per lattice site. This ensures that the number of atoms per site is fixed because hopping of atoms between different sites is inhibited. In order to simulate the electronic spin degrees of freedom of a typical solid we use longlived atomic states. These are usually chosen among hyperfine levels, as in the case of ^{87}Rb or ^{23}Na which have nuclear spin 3/2. In this case the states can be chosen as $|0\rangle = |F = 1, m_f = 1\rangle$ and $|1\rangle = |F = 2, m_f = 2\rangle$ [JBC$^+$99]. These two states are the simulated spin 1/2 states that we need for the simulation.

The interaction between different spins can be simulated by changing the interaction between atoms. This in turn is varied by adjusting the laser parameters and by means of electric and magnetic fields. In this way we can produce a variety of common spin Hamiltonians for solids [GRC03]. For probe particles we use different atoms (white in Fig. 7.6), called marker qubits [CDJ$^+$04]. The main idea is first to construct the optical lattice,

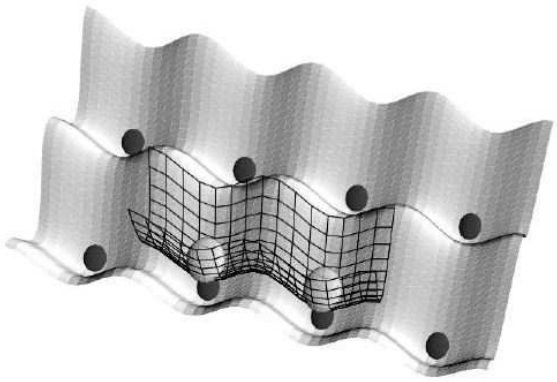

Figure 7.6: Simulation of the entanglement extraction using optical lattices. Cold neutral atoms (black) are loaded onto an optical lattice generated by counter-propagating lasers in such a way that each potential well is occupied by only one atom. These atoms represent the spins degrees of freedom in a typical solid. To the first potential a second one is superimposed (wireframe) onto which different atoms (white), called markers, are loaded. It is possible to move the markers across the solid by moving adiabatically the second potential.

loading the atoms in a register that constitutes the simulated solid (black in Fig. 7.6) and then to superimpose a second optical lattice (wireframe in Fig. 7.6) loading auxiliary atoms onto it as shown in Fig. 7.6. The auxiliary marker atoms need not to be of the same atomic species as the atoms in the solid. The marker atoms can be moved through the solid by varying adiabatically laser parameters of the second optical lattice. These operations do not affect the register atoms that remain confined in their potential wells. In this way collisions between the probes and the spins in the solid can be simulated by moving a marker atom close to a register atom letting their orbitals overlap which realizes swap operations needed for our protocol.

Two marker atoms are moved using the superimposed potential to collide with the register atoms as shown in Fig. 7.6. This we believe can be performed with high precision and efficiency as in the case of cold controlled collisions [MGW$^+$03]. Such an operation can be repeated many times moving the markers forward to collide with other register atoms.

In the model discussed above we supposed that the probes interact each with one spin in the chain. This is in certain cases, such as neutron scattering, very unrealistic. It is difficult with present day technology to address a single spin in a solid. What happens in neutron scattering experiments is that the spin of the incoming neutron interacts with the total angular momentum of a bunch of spins in the solid [RW00]. It is thus more realistic to analyze a model in which two probes interact with many spins. Let us consider a chain of L spins and that each neutron, being a wavepacket of a certain width, interacts with a different subset of N spins. We will assume that the spin of the probe is coupled to the total angular momentum of the N spins, which is equivalent to assume that each probe is equally coupled to each of the N spins in the chain. This model is equivalent to the ones considered in others contexts [HB02] (see chapter 4), and for $\lambda = 0, 1$ its eigenstates are known. Let the initial state of the chain be a W state (see Sec. 1.2):

$$|W_L\rangle = \frac{1}{\sqrt{L}} \left(|100\cdots0\rangle + |010\cdots0\rangle + \cdots + |000\cdots1\rangle \right) \tag{7.13}$$

W states can be ground states of some Hubbard related Hamiltonians [dBKS95], critical spin chains [OAFF02, BDE+04] and fermionic lattice models of high T_c superconductivity [Ved04]. The concurrence for $\lambda = 0$ is $C = \frac{2N}{L} \sin^2 2J\sqrt{N}\tau$ and reaches the maximum value $\frac{2N}{L}$ for $J\tau = \pi/(4\sqrt{N})$ (the entanglement for the Heisenberg model $\lambda = 1$ is greater than zero but is always less than that of the XY model). We note that these results have been obtained only for a W state of the chain. This state contains long range correlations. However for Heisenberg and XY chain models long range correlations are very small and the entanglement extracted should decrease with N and with the distance between the two beams of neutrons.

7.4 The extraction of multipartite entanglement and interaction with many spins

Until now we concentrated on extracting entanglement between only two spins. But our scheme can also be adapted to the extraction of genuine multipartite entanglement. Let us consider n spins in a chain and scatter off of each spin only one probe. Let us suppose that the initial state of the chain be a W state and the probes be in state $|\mathbf{0}\rangle = |00\cdots0\rangle$. The state of the system at time τ is the analogue for n spins of eq.(7.3) with $|W_n\rangle$ instead of $|\psi^-\rangle$. Thus the reduced density matrix for the n probes reads:

$$\rho = \cos^2 2J\tau|\mathbf{0}\rangle\langle\mathbf{0}| + \sin^2 2J\tau|W_n\rangle\langle W_n| \tag{7.14}$$

Notice that when $J\tau = \pi/4$ the state of the chain is fully swapped onto that of the probes as in the case with $n = 2$. For any value of $J\tau \neq k\pi/2$ where k is an integer it can be shown that the above state contains genuine multipartite entanglement [BDE$^+$04] (i.e. it cannot be written as a mixture of biseparable state).

Chapter 8

Entanglement Entropy dynamics in Heisenberg chains

Applications of quantum information theory in condensed matter [Pre00] have produced many interesting results for both disciplines. It is hard to list all the numerous problems addressed so far. Here we only mention the study of entanglement in quantum critical systems (see for example [OAFF02, ON02, VLRK03, LRV04, VMDC04, VPC04a, JK04, VPM04, CZWZ04, CC04, LEB04, Kor04, FKR04, WSL04, IJK05, SOB$^+$04, DHH$^+$05, RVF$^+$04, EC05, OLEC05, KM05, KM04, PZ05, AGMT05, GT05, WDM$^+$05, HRP05] and references therein).

Among all the various ways to quantify entanglement here we consider the block entropy which has recently analyzed in several different situations (see e.g. [VLRK03,CC04,Kor04,EC05,KM05,PZ05,PEDC05,Lev04,ZBFS05, LORV05]). It has been demonstrated [HLW94, VLRK03, CC04] that the entropy of a block of spins S_ℓ in the ground state of a spin chains is very sensitive to its critical properties. In the case of a block with one boundary with the rest of the chain S_ℓ, for $\ell \gg 1$, diverges at the critical point as $S_\ell = (c/6)\log_2 \ell$ where c is the central charge of the corresponding conformal field theory (CFT) of the model considered. In contrast in non critical systems the entropy saturates to the finite value $S_\ell = (c/6)\log_2 \xi$, with $\xi \gg 1$ the

correlation length [CC04]. In the presence of quenched disorder the properties of the block entropy for critical chains remain remarkably universal. For the models analyzed in Ref. [RM04] using real-space renormalization group, it still diverges logarithmically with a "renormalized" central charge $c_{\text{eff}} = c \ln 2$ [RM04], where c is the central charge of the corresponding pure model. It has been conjectured that such an effective central charge characterizes generically the critical systems with quenched disorder [RM04, Laf05].

The interest in the properties of entanglement in condensed matter has also extended to understand its dynamical behaviour. Like for the case of propagation of excitations in condensed media, it recently became of interest to know how entanglement could propagate through spin chains. This question was studied by looking at two-particle [MBF03, AOP+04, Kcz04, SSL05] and many-particle entanglement [CC05, MV05]. The dynamics of entanglement was studied either by preparing the system in a state (not an eigenstate) with all the entanglement localized in a given part of the chain or after a sudden quench of some of the couplings of the model Hamiltonian.

In this chapter we consider static and dynamical properties of the entropy of a block of spins for an anisotropic Heisenberg chain both in the clean and in the disordered case. We investigate the problem by means of DMRG [Sch05a] for the static part and its time-dependent version [DKSV04, WF04] for the dynamical evolution (for an introduction to DMRG and t-DMRG see appendix B). The static entropy of the Heisenberg model was considered numerically in Ref. [VLRK03, PZ05, ZPW06, ZBFS05, LSCA05] and some exact results are known in the isotropic ferromagnetic limit [PS04, PSS05] and in the XX and Ising limits [JK04, IJK05, PZ05, KM05]. In this work we consider again this case for completeness. In addition it serves as an important check for the other cases considered (see Sections 8.2.1, 8.2.2, 8.3.1, 8.3.2) for which these are, to the best of our knowledge, the first numerical calculations available for the Heisenberg model. The results of the dynamics of an ordered chains are compared with the CFT results of Ref. [CC05]. In the static disordered case we confirm the prediction of [RM04]. Section 8.3.2 is devoted to the

dynamics of a disordered Heisenberg chain. Here we predict a slow evolution for the dynamics of entanglement which hints at some sort of entanglement localization.

8.1 The model

The model that we consider is a spin chain of length N with *open* boundary conditions described by the Heisenberg Hamiltonian [LM66]

$$H = \sum_{i=1}^{N-1} J_i(\sigma_x^i \sigma_x^{i+1} + \sigma_y^i \sigma_y^{i+1} + \Delta \sigma_z^i \sigma_z^{i+1}) \tag{8.1}$$

where $\sigma_{x,y,z}^i$ are the Pauli matrix operators relative to the ith spin; J_i are the coupling constants that we assume time independent but possibly space-dependent in the random case; finally Δ is the anisotropy parameter. The homogeneous chain is critical for $-1 \leq \Delta \leq 1$. The corresponding Conformal Field Theory (CFT) is described using a central charge $c = 1$.

We study the properties of the Von Neumann entropy S_ℓ of a block containing the first ℓ spins. The block is described by the reduced density matrix $\rho_\ell = \mathrm{Tr}_{i>\ell}\rho$ and S_ℓ is defined as:

$$S_\ell = -\mathrm{Tr}_\ell \left(\rho_\ell \log_2 \rho_\ell\right) \tag{8.2}$$

We used the t-DMRG algorithm with a second order Trotter expansion of H as described in Refs. [DKSV04, WF04]. We checked the precision of the numerics by comparing the results with the case $\Delta = 0$ where Eq. (8.1) is mapped onto a free fermion model [LM66].

We first present the result for the homogeneous case and then that for the disordered one.

8.2 Homogeneous chain

8.2.1 Ground state properties

The CFT prediction for a block of length ℓ in an open chain of total length N is [CC04]

$$S_\ell = \frac{c}{6} \log_2 \left[\frac{N}{\pi} \sin \left(\frac{\pi}{N} \ell \right) \right] + A \tag{8.3}$$

where A is a non-universal constant related to the analogous one in the system with periodic boundary condition [CC04, ZBFS05]. As already mentioned the static properties of the Heisenberg model was considered numerically in Ref. [VLRK03, PZ05, ZPW06, ZBFS05] and here for completeness we present the result of our DMRG calculations. They are shown in Fig. 8.1. The main plot shows the difference in the entropy for a critical and a non critical value of Δ and the comparison to the CFT prediction. For large ℓ (i.e. $\ell > 10$) where Eq. (8.3) is expected to work, the agreement is very good. In the lower inset we show our results for the central charge, obtained through a fit of numerical data with Eq. (8.3), for different values of Δ in the critical interval. The fitted c shows small non-universal variations with Δ which decrease increasing N and are expected to vanish in the thermodynamic limit. This is shown in the top inset for the worst case $\Delta = 0.5$. The extrapolated value of the central charge (upper inset) has been obtained fitting $c(1/N)$ with a quadratic polynomial and taking the limit $1/N \to 0$. The result is $c = 1.01 \pm 0.05$. Note that since we are using open boundary conditions the entropy oscillates with the parity of the block. This can be explained with a simple argument. Because of the XXZ interaction, neighbor spins tend to form spin singlets, so the oscillations in the entropy of block reflect the breaking or not of one of these singlets. Such an alternating behaviour has been observed also in Ref. [LSCA05]. Though this behavior disappears increasing N we fitted numerical data for even ℓ because the convergence is faster.

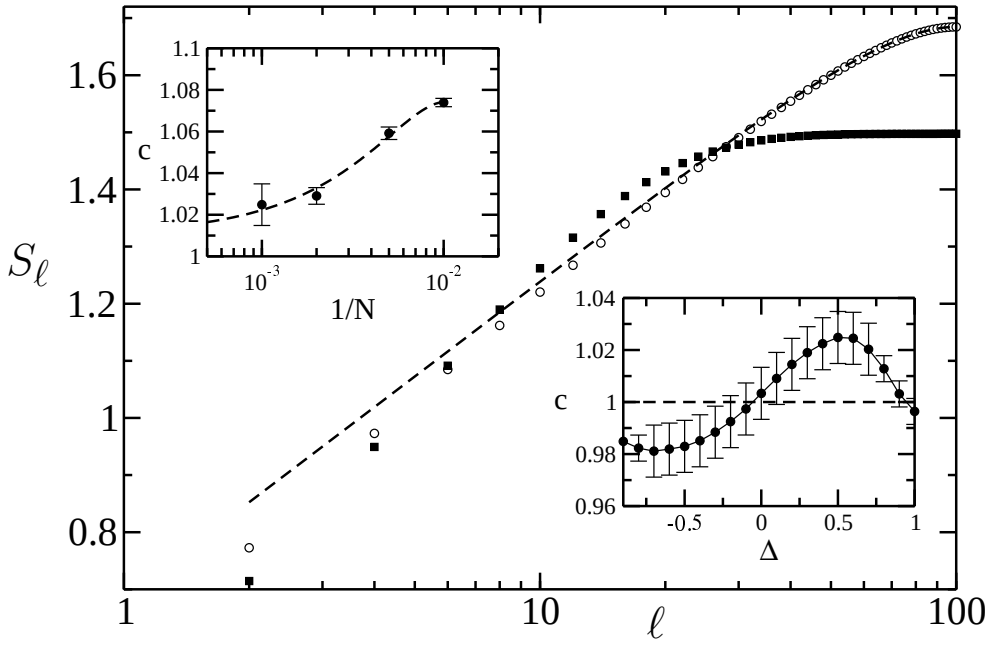

Figure 8.1: The Block entropy S_ℓ for $N = 200$ for a critical value $\Delta = 0.0$ (circles) and non-critical value $\Delta = 1.8$ (squares) and $m = 120$. The critical data compared with the CFT prediction Eq. (8.3) (dashed line). Lower inset: central charge extrapolated by fitting the numerical data S_ℓ with Eq. (8.3) for different values of Δ. The data are for $N = 1000$ and $m = 120$. Upper inset: scaling of c extrapolated as a function of $1/N$ for the worst case $\Delta = 0.5$ and compared to a quadratic fit (dashed line).

8.2.2 Dynamical behaviour

To date the only results obtained for the evolution of block entropy after a quench have been obtained in Ref. [CC05]. By means of CFT it was shown that a quench of the system from a non critical to a critical point leads the block entropy to increase in time until a saturation point is obtained. For periodic boundary conditions, the time at which the entropy saturates is given by $t^* = \ell/(2v)$ where v is the spin wave velocity: $v = \partial E_k/\partial k|_{k=0}$. This phenomenon has a simple interpretation in terms of quasiparticles excitations emitted from the initial state at $t = 0$ and freely propagating with velocity v. This explanation holds even for non critical systems, as it has been confirmed

by the exact solution of the Ising chain dynamics [CC05]. However, since in lattice models there are particles moving slower than v, after t^* the entropy does not saturate abruptly, but is a slowly increasing function of the time. We now consider the dynamics of the Heisenberg model with open boundary conditions, and we will find that $t^* = \ell/v$. At the end of this section we will interpret this result in terms of quasiparticles and we will derive it within CFT.

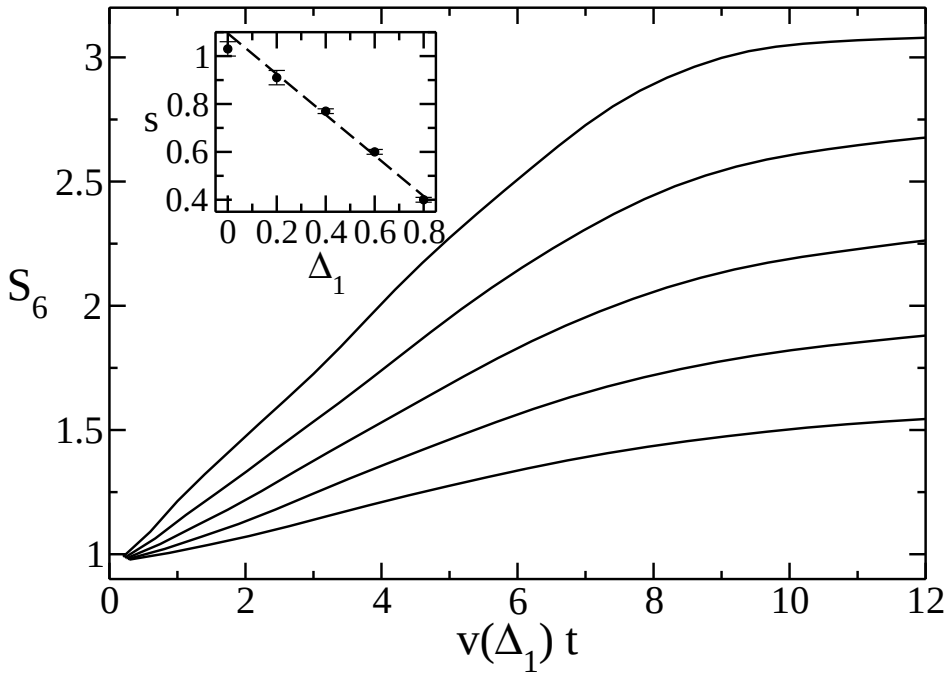

Figure 8.2: Evolution of the entropy S_6 with various quenches. $\Delta_0 = 1.5$ while $\Delta_1 = 0.0, 0.2, 0.4, 0.6, 0.8$ as a function of $v(\Delta_1)t$. Inset: initial slope value of S_6 as a function of Δ_1 and comparison to a linear fit with slope -0.85 ± 0.02 (dashed line).

In the case of the Heisenberg Hamiltonian in the critical regime the spin wave phase velocity is given by $v(\Delta) = 2J\pi \sin\theta/\theta$ with $\cos\theta = \Delta$ [VEKI93]. The initial state of the system is chosen as the ground state of Hamiltonian Eq. (8.1) with $\Delta = \Delta_0 > 1$, after a quench the system evolves with same Hamiltonian but with a different anisotropy $\Delta = \Delta_1 \in [0; 1]$. In the simu-

lations we considered chains with $N = 50$, a Trotter slicing $J\delta t = 5 \cdot 10^{-2}$ and a truncated Hilbert space of $m = 200$. The block was chosen to be of 6 sites which is large enough, as we show, to confirm the CFT prediction. We have checked convergence with m and δt. For the special case $\Delta_0 = +\infty$ and $\Delta_1 = 0$ we compare our data with the exact result obtained diagonalizing the XX model as shown in C.

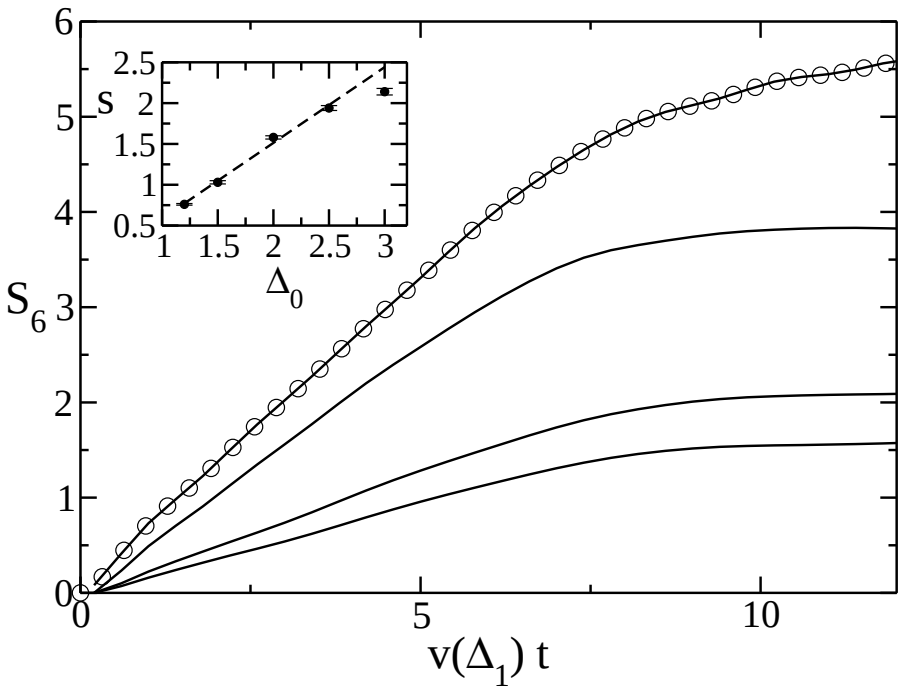

Figure 8.3: Evolution of the entropy S_6 with various quenches. $\Delta_0 = 1.2, 1.5, 3.0, \infty$ while $\Delta_1 = 0.0$ as a function of $v(\Delta_1)t$ and shifted so to coincide in $t = 0$. For $\Delta_0 = \infty$ we show also the exact result obtained by diagonalization (circles). Inset: initial slope value of S_6 as a function of Δ_1.

Various quenches have been considered. First of all we present the results with Δ_0 fixed and Δ_1 variable shown in Fig. 8.2. As in Ref. [CC05] the entropy grows linearly in time $S \sim sJt$ and finally saturates. At $t = t^* = \ell/v$, the entropy does not saturate abruptly. As discussed for the Ising model, this is due to slow quasiparticles [CC05]. The inset of Fig. 8.2 shows the initial slope as a function of Δ_1. The dashed line is a linear fit with slope 0.85 on

the data except $\Delta_1 = 0$. In Fig. 8.3 the time evolution of the entropy is shown for quenches starting from different values of Δ_0 and ending with the same $\Delta_1 = 0$. The case in which both Δ_0 and Δ_1 are varied (keeping their difference fixed, $\Delta_0 - \Delta_1 = 1.5$) is shown in Fig. 8.4.

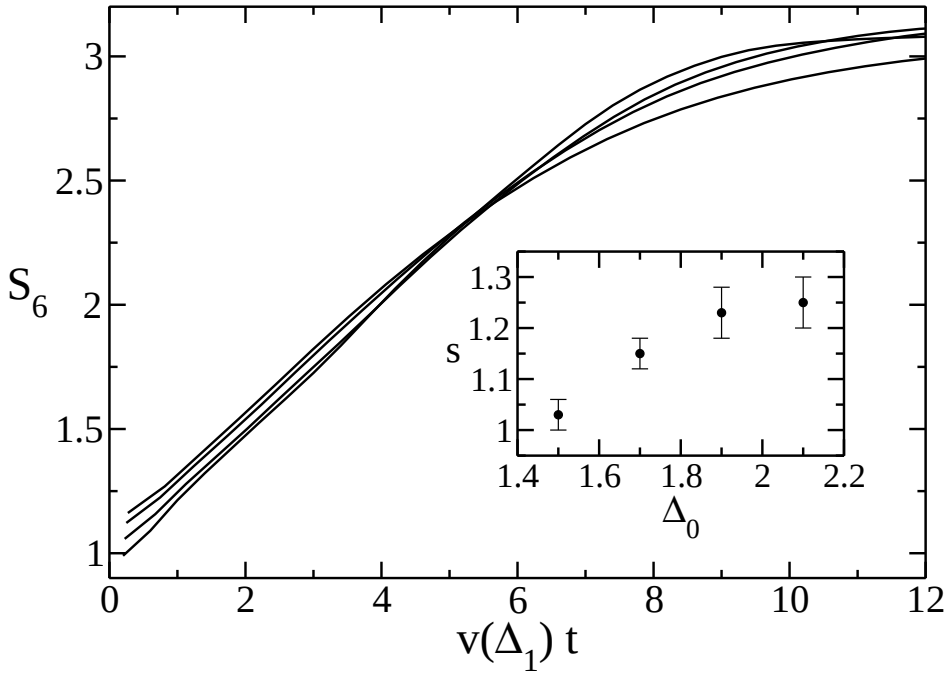

Figure 8.4: Evolution of the entropy S_6 with fixed quench as a function of $v(\Delta_1)t$. Fixed quench $\Delta_0 - \Delta_1 = 1.5$ for $\Delta_0 = 1.5, 1.7, 1.9, 2.1$. Inset: initial slope value of S_6 as a function of Δ_0.

The behaviour of the slope s (the entropy for $t \leq t^*$ goes as $S \sim sJt$) for $\ell = 20$ as a function of Δ_0 and Δ_1 can be fitted for a large portion of values by the law

$$s = 1.50\Delta_0 - 0.84\Delta_1 - 0.90 \quad .$$

In Fig. 8.5 the fit and the numerical data are compared. Following the simple model introduced in [CC05], the initial slope of the entropy increase is a non-trivial function of both Δ_0 and Δ_1 as it depends both on the crossection for producing the quasiparticles and their velocity.

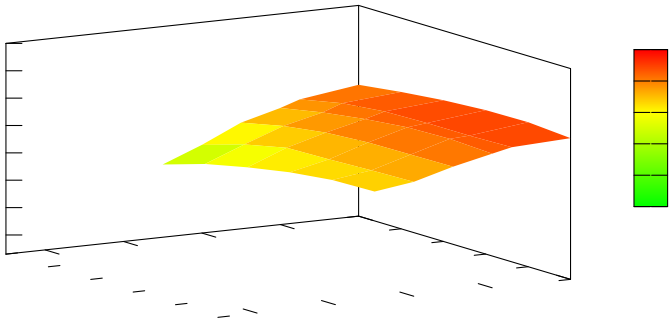

8.3 Disordered chain

8.3.1 Ground state properties

The striking prediction of Refael and Moore [RM04] that the block entropy of random chains has a logarithmic divergence with an effective (universal) central charge has been confirmed by numerical calculations on the XX model [Laf05]. Here we extend these results to the model defined in Eq. (8.1) where the randomness is introduced through the couplings J_i chosen to be random numbers with a uniform distribution in the interval $[0;1]J$. According to Ref. [RM04], the block entropy should scale with an effective central charge $c_{\text{eff}} = \ln 2 \simeq 0.69$. In Fig. 8.6 we show for $N = 50$ the entropy of a block of length ℓ for the random model for $\Delta = 1$ averaged over 10^4 different configurations of disorder. From the scaling of the entropy as a

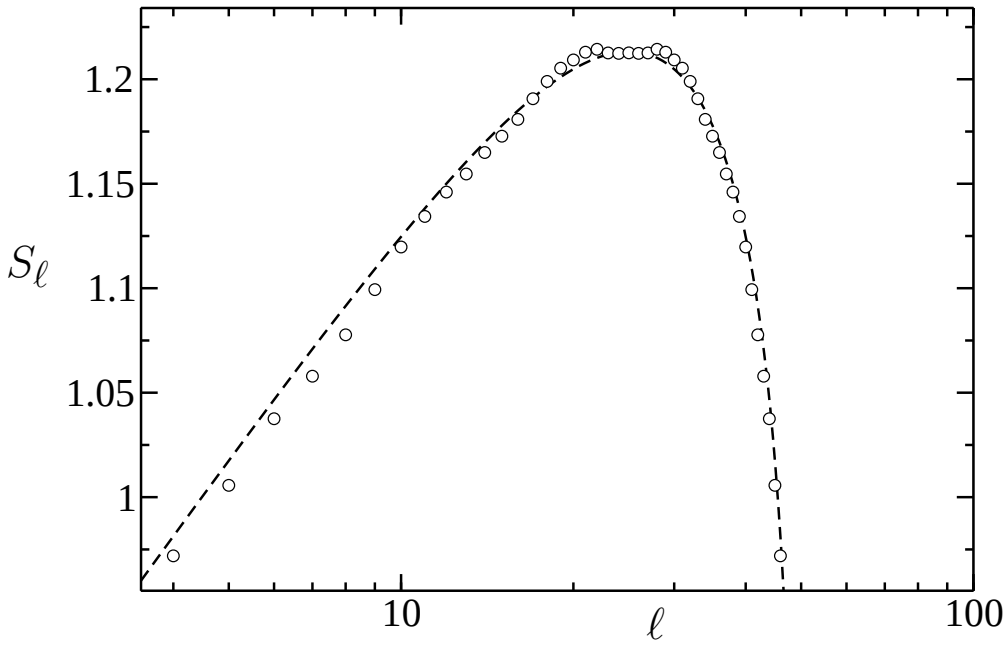

Figure 8.6: The Block entropy S_ℓ for the random model for a critical value $\Delta = 1.0$ (circles) for $N = 50$ and $m = 50$. These are compared with the Refael and Moore prediction Eq. (8.3) (dashed line). The data have been averaged over 10^4 realizations.

function of ℓ we can extract the effective central charge for this model. The result is $c_{\rm fit} = 0.67 \pm 0.05$ in very good agreement with Refael and Moore proposal.

8.3.2 Dynamical behaviour

No analytic results are known so far for the dynamics of block entropy in the case of disordered systems. This, in our opinion may be an interesting question as it is well known that in the presence of disorder the ballistic propagation of quasiparticles turns into diffusion and, in certain circumstances, into localization. It is therefore to be expected that entanglement itself will be affected by the presence of static randomness. At the level of the ground state properties the effect of disorder manifests in a "renormalization" of the central charge. As we will show below the dynamical behaviour, instead, is strikingly different in the clean and disordered cases.

As in the clean case we analyzed the evolution of a random chain with a quench in the anisotropy from a non-critical Δ_0 to a critical value Δ_1 for various cases. Interestingly now the entropy does not grow linearly as in the non-random case. Although it is very difficult, in the absence of any analytic result, to ascertain the exact time dependence of the entropy, our data clearly indicate that the entropy grows logarithmically as a function of time. This is shown in Fig. 8.7 where we report the t-DMRG results for several quenches. After a transient behaviour, all the curves in Fig. 8.7 behave like

$$S_\ell \sim \kappa \ln Jt \,, \tag{8.4}$$

where κ depends on the details of the quench. For example we find $\kappa \sim 0.5$ for $\Delta_0 = \infty$ and $\Delta_1 = 0$, and $\kappa \sim 0.22$ for $\Delta_0 = 2$ and $\Delta_1 = 0$ (with ln the natural logarithm). Clearly such logarithmic growth cannot continue indefinitely, but with t-DMRG it is hard to investigate times larger than those reported.

To shed some light on the long time behaviour of S_ℓ, we consider extensively

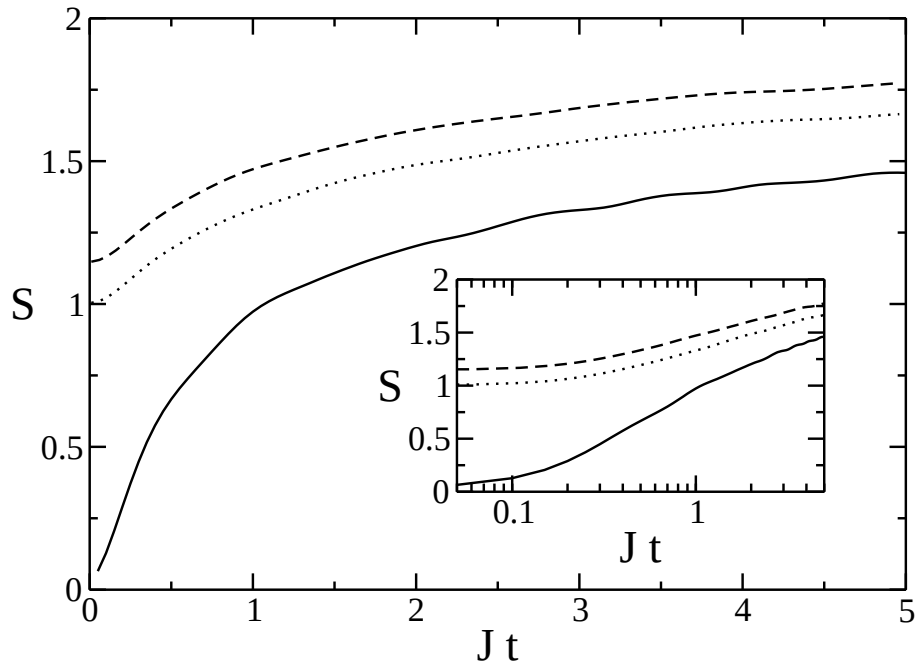

Figure 8.7: Dynamics of the entropy for the random Heisenberg model obtained using the t-DMRG for various quenches. The solid line is a quench from $\Delta_0 = \infty$ to $\Delta_1 = 0$ for a block of $\ell = 10$. The dotted and dashed lines are quenches from $\Delta_0 = 2$ to $\Delta_1 = 0$ for two block sizes $\ell = 10$, $\ell = 20$ respectively. In the three cases we considered $N = 50$. Inset: the same plot but in semi-logarithmic scale. The parameters of the DMRG calculation are $m = 60$ and $J\delta t = 5 \cdot 10^{-2}$. The data have been averaged over 10^3 for the quench from $\Delta_0 = +\infty$ and 400 for those with $\Delta_0 = 2$.

the diagonalization of the XX model starting from $\Delta_0 = \infty$, as described in appendix C. The exact diagonalization of the XX model allows us to consider chain up to 120 sites, blocks of up to 50 sites and to follow the dynamical evolution to longer times as presented in Fig. 8.8. The analysis on the XX model was used furthermore to check the accuracy of the t-DMRG data. This is shown in the inset of Fig. 8.8 where the discrepancy is below 3%.

Interestingly, Fig. 8.8 shows the end of the logarithmic growth of S_ℓ, even if the complete saturation is not yet reached. All the data of Fig. 8.8 are

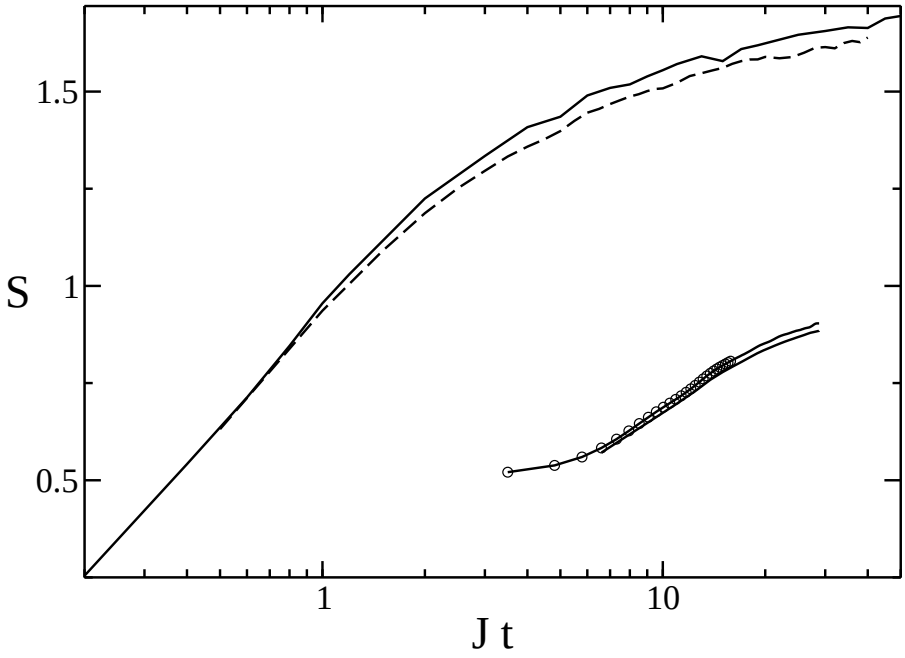
1.5
1
0.5
S
1
10
J t

$t \to \infty$ the entanglement entropy saturates to $\nu/2 \ln \ell$. Thus for infinitely large times the entanglement entropy saturates to a value that is reminiscent of the one in the ground state, but the prefactor of the logarithm seems to be different (if our fit holds for large times it is exactly the half).

Several considerations are in order at this stage. As compared to the clean case (Figs. 8.2, 8.3, 8.4) the increase of the entropy as a function of time is much slower. The logarithmic behaviour does not follow from an extension of the argument for the clean case [CC05] assuming that pair of particles that are emitted diffuse rather than moving ballistically. At this stage we cannot present arguments to derive the logarithmic increase of entropy in disordered chain. This behaviour is probably associated with a sort of entanglement localization.

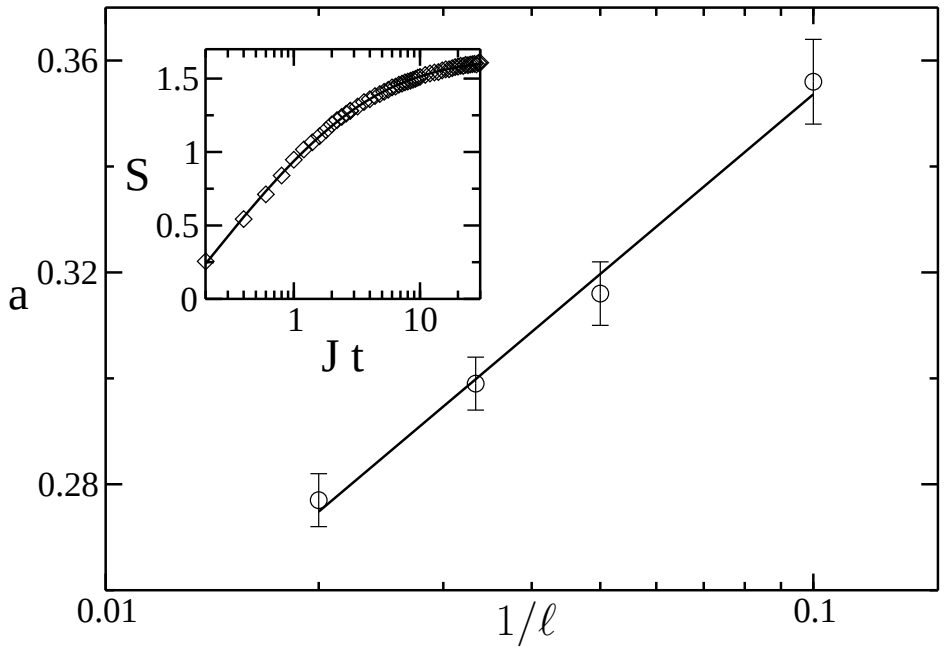

Figure 8.9: Scaling of the coefficient $a(\ell)$ of Eq.(8.5) with the dependence of the length of the block. A power law behaviour $a(\ell) \sim \ell^{-\nu}$ (with $\nu = 0.16 \pm 0.01$) fits well all the range considered. In the inset we show an example of a fit with the logarithmic behaviour suggested in Eq. (8.5); the accuracy shown in the figure is obtained for all the cases analyzed in this work

Summary

My research during the three years of PhD was twofold: on one hand we analyzed methods for protecting quantum information from environmental noise and on the other hand we studied ground state properties, like entanglement, in critical systems.

Protecting quantum information is of crucial importance in QIT especially when dealing with noisy implementation. This is the case in solid state systems, where decoherence is the main drawback to the realization of a quantum computer. We analyzed different areas of QIT. First, in the context of QEC, we analyzed the evolution of a quantum register interacting with a correlated environment. We showed how information stored in the register can be better protected against decoherence induced by the environment. Furthermore when the time between two subsequent corrections is large enough, the correction procedure is able to amplify the entanglement produced. The entanglement creation rate with QEC is larger, in certain regimes, than the case in which no QEC is performed. In this scenario we are in a situation in which the entanglement induced by the unitary dynamics generated by the correlated bath is enhanced by the QEC protocol which prevents the dephasing effects of the coupling with the bath. Note that such enhancement in the production rate of entanglement is achieved by means of local measurements and conditional local unitary operations on the logical qubits, in other words the entanglement is not induced by joint measurements on the pair of logical qubits.

The second issue we studied was the possibility to achieve certain compu-

tational tasks, such as quantum communication or quantum cloning, using a network of interacting spins. With this setup the free evolution of the network is sufficient to perform the desired protocol. In the case of quantum communication we analyzed a protocol capable of perfect state transfer between two distant parties. Even if decoherence can be kept under a sufficient level, static imperfections in the system parameters cannot be avoided. This kind of errors seems to represent a serious problem for quantum computation because of the appearance of quantum chaos. This is not the only change in the presence of disorder: the temporal dependence of the output fidelity becomes fractal.

In the context of quantum cloning, we demonstrated how to realize PCC using a spin network and that for the $1 \rightarrow 2$ PCC our protocol saturates the optimal bound. Comparing the noise effect in the network and in a quantum circuit that realizes PCC we found that our protocol is more efficient because the time needed to perform it is greatly reduced. In addition we expect that the system in the SNC is better isolated from the external environment because no gate pulses are needed. Finally we proposed a possible implementation of our scheme using superconducting devices available with present day technology. This would be the first experimental realization of quantum cloning in solid state systems. We want to stress that our results on cloning together with others on communication and computation open new perspectives in the realization of a quantum processor, reducing the effect of noise on the system. It would be interesting to consider if it is possible to realize other quantum information protocols or quantum algorithms, using time independent spin networks.

Spin chains are not only a working tool for quantum communication in solid state systems, but also a useful benchmark for studying quantum physics: foundations of quantum mechanics and quantum phase transitions. Entanglement plays a remarkable role in quantum mechanics, apart from its practical use in QIT. It is thus interesting to study under which conditions entanglement can be found in but even extracted from solid state systems.

We studied a general scheme to extract entanglement from spin chains by means of a scattering process in which two incoming particles get entangled by extracting it from the entangled state of a chain. In this way macroscopic thermal entanglement of solids can be extracted and used for quantum computation. We have proposed an optical lattice implementation where all aspects of our procedure can be realized with present-day technology. In this context optical lattices offer only a simulation of entanglement extraction. This is why we have discussed how neutron scattering can be used to achieve entanglement extraction from a real solid as well as the physical limitations of this process. We hope that our ideas in the long run will lead to an entangling procedure for neutrons in the same way as parametric down conversion is for creating entangled photons.

Quantum phase transition can have an effect on the ground state entanglement of one dimensional spin chains. It was known that the entanglement entropy of a block of ℓ sites diverges logarithmically with ℓ. Remarkably the prefactor is proportional to the central charge of the corresponding conformal field theory. We studied the production of entanglement in the XXZ model after a quench of the system from a non-critical to a critical point. In the homogeneous case the block entropy grows linearly until saturating at a particular time, which has a simple interpretation in terms of emission of quasi particles. In the disordered model the block entropy grows only logarithmically in time signaling the onset of entanglement localization. Most of the calculations have been performed using the density matrix renormalization group (DMRG) and its time dependent version, developed during my PhD.

DMRG was used also in the study of the ground state properties of the spin-1 Bose Hubbard model. Apart from the quantitative calculation of the phase diagram of this model, we studied also the magnetic properties of the ground state. Our results indicate that the Mott insulator is always in a dimerized phase.

Finally we also analyzed the effect of quantum noise on Berry phase, this

made us understand what is the geometrical contribution to the dephasing rate and on the Lamb shift. We approached the problem using the quantum Langevin equations. In our opinion this is a simple straightforward method for the calculation of physical quantities such as decays and shifts. We showed that the decay rate is only slightly modified with the adiabatic evolution. Furthermore we gave a geometrical interpretation to the correction of the Berry phase induced by the environment.

Appendix A

Calculus of the fidelity using perturbation theory

We are interested in evaluating the fidelity (3.9) averaged over different disorder realizations. Equation (3.6) shows that it depends on the matrix element

$$\begin{aligned} f_N(t) &= \langle \boldsymbol{N}|e^{-\imath(H+H_I)t}|\mathbf{1}\rangle \\ &= \langle \boldsymbol{N}|e^{-\imath Ht}\mathcal{T}\left[\exp\left(-\imath\int_0^t dt\, e^{\imath Ht}H_I e^{-\imath Ht}\right)\right]|\mathbf{1}\rangle \\ &= 1+\mathcal{O}(H_I)+\mathcal{O}(H_I^2) \end{aligned} \tag{A.1}$$

where $\mathcal{T}$ is the time ordered product, $\hbar = 1$, and H_I is the part of the Hamiltonian that describes the static imperfections b_k, δ_k. We first consider the case where $\delta_k = 0$, that is, only random local magnetic fields are present. We develop the time ordered product up to the second order in H_I. The first order term reads

$$\begin{aligned} \mathcal{O}(H_I) &= -\imath\int_0^t dt\langle \mathbf{1}|e^{\imath Ht}H_I e^{-\imath Ht}|\mathbf{1}\rangle \\ &= -\imath\sum_{\ell=1}^N b_\ell\int_0^t dt(1-2|U_\ell^1(t)|^2) \equiv -\imath\sum_{\ell=1}^N b_\ell C_\ell(t), \end{aligned} \tag{A.2}$$

where $U_\ell^k(t) \equiv \langle \boldsymbol{\ell}|e^{-\imath Ht}|\boldsymbol{k}\rangle$ [FLS65]. The second order is given by

$$\mathcal{O}(H_I^2) = -\int_0^t\int_0^t dtdt'\langle \mathbf{1}|e^{\imath Ht}H_I e^{-\imath H(t-t')}H_I e^{-\imath Ht'}|\mathbf{1}\rangle$$

$$
\begin{aligned}
&= -\sum_{\ell=1}^{N}\sum_{m=1}^{N} b_\ell b_m \int_0^t \int_0^t dt\, dt' \Big[1 - 2\left|U_m^1(t)\right|^2 \\
&- 2\left|U_\ell^1(t')\right|^2 + 4U_m^{1*}(t)U_\ell^1(t')\sum_{k=1}^{N} U_m^k(t)U_k^{\ell *}(t')\Big] \\
&\equiv -\sum_{\ell=1}^{N}\sum_{m=1}^{N} b_\ell b_m D_{\ell,m}(t). \qquad \text{(A.3)}
\end{aligned}
$$

The fidelity (3.9

Appendix B

Brief introduction to DMRG

The advent of information era has been opening the possibility to perform numerical simulations of quantum many-body systems, thus revealing completely new perspectives in the field of condensed matter theory. Indeed, together with the analytic approaches, numerical techniques provide lot of information and details otherwise inaccessible. However, the simulation of a quantum mechanical system is generally a very hard task; one of the main reasons is related to the number of parameters required to represent a quantum state. This value usually grows exponentially with the number of constituents of the system [Fey82], due to the corresponding exponential growth of the Hilbert space. This exponential scaling drastically reduces the possibility of a direct simulation of many-body quantum systems. In order to overcome this limitation, many numerical tools have been developed, as Monte Carlo techniques [LB00, SK91] or efficient Hamiltonian diagonalization methods as Lanczos and Davidson procedures [vdV02].

The Density Matrix Renormalization Group (DMRG) method has been introduced by White in 1992 [Whi92, Whi93]. It was originally devised as a numerical algorithm useful for simulating ground state properties of one-dimensional quantum lattices, such as the Heisenberg model or Bose-Hubbard models; then it has also been adapted in order to simulate small two-dimensional systems [PWKH99, Sch05a]. DMRG traces its roots to Wil-

son's numerical Renormalization Group [Wil75] (RG), which represents the simplest way to perform a real-space renormalization of Hamiltonians. Starting from a numerical representation of some microscopic Hamiltonian in a particular basis, degrees of freedom are iteratively added, typically by increasing the size of the finite system. Then less important ones are integrated out and accounted for by modifying the original Hamiltonian. The new Hamiltonian will thus exhibit modified as well as new couplings; renormalization group approximations consist in physically motivated truncations of the set of couplings newly generated by the elimination of degrees of freedom. In this way one obtains a simplified effective Hamiltonian that should catch the essential physics of the system under study. Very recently, influence from the quantum information community leads to a DMRG-like algorithm which is able to simulate the temporal evolution of one-dimensional quantum systems [Vid03, Vid04, DKSV04, WF04, FW05, MMN05, GR06].

Quantum information theory has also allowed to clarify the situations in which this method can be applied efficiently. Indeed, it has been shown [Vid03] that the efficiency in simulating a quantum many-body system is strictly connected to its entanglement behavior. More precisely, if the entanglement of a subsystem with respect to the whole is bounded (or grows logarithmically with its size) an efficient simulation with DMRG is possible. Up to now, it is known that ground states of one dimensional lattices (whether critical or not) satisfy this requirement, whereas in higher dimensionality it is not fulfilled as the entanglement is subject to an area law [VLRK03, LRV04]. On the other hand, the simulation of the time evolution of critical systems may not be efficient even in one dimensional systems as the block entanglement can grow linearly with time and block size (see [CC05] and chapter 8. In a different context, it has also been shown that in a quantum computer performing an efficient quantum algorithm (Shor's algorithm and the simulation of a quantum chaotic system) the entanglement between qubits grows faster than logarithmically [OL04a, Mon04]. Thus, t-DMRG cannot efficiently simulate every quantum one dimensional system; nonetheless, its

range of applicability is very broad and embraces very different subjects.

In this appendix we introduce the last development of DMRG codes, briefly but in a comprehensive way. In Sec. B.1 we describe the basics of time independent DMRG algorithm, in Sec. B.2 we introduce the measurement procedure (a more detailed exposition is given in Ref. [Sch05a] and references therein). In Sec. B.3 the time dependent DMRG algorithm is explained. Finally, in Sec. B.4 we provide some numerical examples, and in Sec. B.5 we discuss some technical issues regarding the implementation of a DMRG program code. In the last section we include the schemes of the DMRG algorithms, both for the static and time dependent case.

B.1 The static DMRG algorithm

As yet pointed out in the introduction, the tensorial structure of the Hilbert space of a composite system leads to an exponential growth of the resources needed for the simulation with the number of the system constituents. However, if one is interested in the ground state properties of a one-dimensional system, the number of parameters is limited for non critical systems or grows polynomially for a critical one [VLRK03]. This implies that it is possible to rewrite the state of the system in an more efficient way, i.e. it can be described by using a number of coefficients which is much smaller than the dimension of the Hilbert space. Equivalently, a strategy to simulate ground state properties of a system is to consider only a relevant subset of states of the full Hilbert space. This idea is reminiscent of the renormalization group (RG) introduced by Wilson [Wil75].

In the RG procedure one typically begins with a small part of a quantum system (a block $\mathcal{B}$ of size L, living on an m-dimensional Hilbert space), and a Hamiltonian which describes the interaction between two identical blocks. Then one projects the composite 2-block system (of size $2L$) representation (dimension m^2) onto the subspace spanned by the m lowest-lying energy

eigenstates, thus obtaining a new truncated representation for it. Each operator is consequently projected onto the new $m-$dimensional basis. This procedure is then iteratively repeated, until the desired system size is reached. RG was successfully applied for the Kondo problem, but fails in the description of strongly interacting systems. This failure is due to the procedure followed to increase the system size and to the criterion used to select the representative states of the renormalized block: indeed the decimation procedure of the Hilbert space is based on the assumption that the ground state of the entire system will essentially be composed of energetically low-lying states living on smaller subsystems (the forming blocks) which is not always true. A simple counter-example is given by a free particle in a box: the ground state with length $2l$ has no nodes, whereas any combination of two grounds in l boxes will have a node in the middle, thus resulting in higher energy.

A convenient strategy to solve the RG breakdown is the following: before choosing the states to be retained for a finite-size block, it is first embedded in some environment that mimics the thermodynamic limit of the system. This is the new key ingredient of the DMRG algorithm; the price one has to pay is a slowdown of the system growth with number of iterations of the algorithm: from the exponentially fast growth Wilson's procedure to the DMRG linear growth (very recently there has been a proposal to recover the exponential growth [Vid05]). In the following, we introduce the working principles of the DMRG, and provide a detailed description to implement it in practice (for a pedagogical introduction see for example [Mal03, NM05]).

B.1.1 Infinite-system DMRG

Keeping in mind the main ideas of the DMRG depicted above, we now formulate the basis structure of the so called *infinite-system* DMRG for one-dimensional lattice systems.The typical scenario where DMRG can be used is the search for an approximate ground state of a 1D chain of neighbor in-

teracting *sites*, each of them living in a Hilbert space of dimension D. As in Wilson's RG, DMRG is an iterative procedure in which the system is progressively enlarged. In the infinite system algorithm we keep enlarging the system until the ground state properties we are interested in (e.g. the ground state energy per site) have converged.

The system Hamiltonian is written as:

$$\hat{H} = \sum_i \sum_q J(q)\hat{S}_i(q)\hat{T}_{i+1}(q) + \hat{B}(q)\hat{V}_i(q) \tag{B.1}$$

where $J(q)$ and $B(q)$ are coupling constants, and $\{\hat{S}_i(q)\}_q$, $\{\hat{T}_i(q)\}_q$ and $\{\hat{V}_i(q)\}_q$ are sets of operators acting on the ith site. The index q refers to the various elements of these sets. For example, in a magnetic chain these can be angular momentum operators. For simplicity we will not describe the case of position dependent couplings, since it can be easily reduced to the uniform case.

The algorithm starts with a *block* composed of one site $\mathcal{B}(1, D)$ (see Fig. B.1a); the arguments of $\mathcal{B}$ refer to the number of sites it embodies, and to the number of states used to describe it. From the computational point of view, a generic block $\mathcal{B}(L, m_L)$ is a portion of memory which contains all the information about the block: the block Hamiltonian, its basis and other operators that we will introduce later. The block Hamiltonian $\hat{H}_B$ for $\mathcal{B}(L, m_L)$ includes only the local terms (i.e. local and interaction terms where only sites belonging to the block are involved). The next step consists in building the so called left *enlarged block*, by adding a site to the right of the previously created block. The corresponding Hamiltonian $\hat{H}_E$ is composed by the local Hamiltonians of the block and the site, plus the interaction term:

$$\hat{H}_E = \hat{H}_B + \hat{H}_S + \hat{H}_{BS} \ . \tag{B.2}$$

The enlarged block is then coupled to a similarly constructed right enlarged block. If the system has global reflection symmetry, the right enlarged block

Hamiltonian $\hat{H}_{E'}$ can be obtained just by reflecting the left enlarged block [1]. By adding the interaction of the two enlarged blocks, a *super-block* Hamiltonian $\hat{H}_{supB}$ is then built, which describes the global system:

$$\hat{H}_{supB} = \hat{H}_E + \hat{H}_{E'} + \hat{H}_{SS'} \ . \tag{B.3}$$

From now on, we refer to the sites S and S' as the *free sites*. The matrix $\hat{H}_{supB}$ should finally be diagonalized in order to find the ground state ψ_G, which can be rewritten in ket notation as:

$$|\psi_G\rangle = \psi_{a\alpha\beta b}|a\alpha\beta b\rangle. \tag{B.4}$$

Hereafter Latin indexes refer to blocks, while Greek indexes indicate free sites; implicit summation convention is assumed. From $|\psi_G\rangle$ one evaluates the reduced density matrix $\hat{\rho}_L$ of the left enlarged block, by tracing out the right enlarged block:

$$\hat{\rho}_L = \mathrm{Tr}_R|\psi_G\rangle\langle\psi_G| = \psi_{a\alpha\beta b}\,\psi^*_{a'\alpha'\beta b}|a\,\alpha\rangle\langle a'\alpha'| \tag{B.5}$$

The core of the DMRG algorithm stands in the renormalization procedure of the enlarged block, which eventually consists in finding a representation in terms of a reduced basis with at most m (fixed *a priori*) elements. This corresponds to a truncation of the Hilbert space of the enlarged block, since $m_{L+1} = \min(m_L D, m)$. If m is bigger than D^2 we do not truncate the basis at the first step. The truncation starts when $m < D^L$ and L is the number of spins in the enlarged block. These states are chosen to be the first m_{L+1} eigenstates of ρ_L, corresponding to the largest eigenvalues. This truncated change of basis is performed by using the $m_L D \times m_{L+1}$ rectangular matrix $\hat{O}_{L\to L+1}$ (where the subscripts stand for the number of sites enclosed in the input block and in the output renormalized block), whose columns, in matrix representation, are the m_{L+1} selected eigenstates. To simplify notations, let us introduce the function $g(a,\alpha) = D(a-1)+\alpha$, which acts on a block index

[1] If mirror symmetry does not hold the right enlarged block must be built up independently.

a and on the next free site index α and gives an index of the enlarged block running from 1 to $m_L D$. The output of the full renormalization procedure is a truncated enlarged block $\mathcal{B}(L+1, m_{L+1})$, which coincides with the new starting block for the next DMRG iteration. This consists in the new block Hamiltonian:

$$\hat{H}'_B = \hat{O}^{\dagger}_{L\to L+1}\, \hat{H}_E\, \hat{O}_{L\to L+1} = \tag{B.6}$$

$$= O^{* g(a,\alpha)\, c}_{L\to L+1}\, H_E^{g(a,\alpha)\, g(a',\alpha')} O^{g(a',\alpha')\, c'}_{L\to L+1}\, |c\rangle\langle c'| \tag{B.7}$$

and in the local operators:

$$\hat{S}'_{L+1}(q) = \hat{O}^{\dagger}_{L\to L+1}\, \hat{S}_{L+1}(q)\, \hat{O}_{L\to L+1} \tag{B.8}$$

written in the new basis. These are necessary in the next step, for the construction of the interaction between the rightmost block site and the free site. The output block $\mathcal{B}(L+1, m_{L+1})$ includes also the matrix $\hat{O}_{L\to L+1}$ which identifies the basis states of the new block.

It is worth to emphasize that we can increase the size of our system without increasing the number of states describing it, by iteratively operating the previously described procedure.

We now summarize the key operations needed to perform a single DMRG step. For each DMRG step the dimension of the super-block Hamiltonian goes from $2L$ to $2L+2$, thus the simulated system size increases by 2 sites. The infinite-system DMRG, with reflection symmetry, consists in iterating these operations:

1. Start from left block $\mathcal{B}(L, m_L)$, and enlarge it by adding the interaction with a single site.
2. Reflect such enlarged block, in order to form the right enlarged block.
3. Build the super-block from the interaction of the two enlarged blocks.
4. Find the ground state of the super-block and the $m_{L+1} = \min(m_L D, m)$ eigenstates of the reduced density matrix of the left enlarged block with largest eigenvalues.

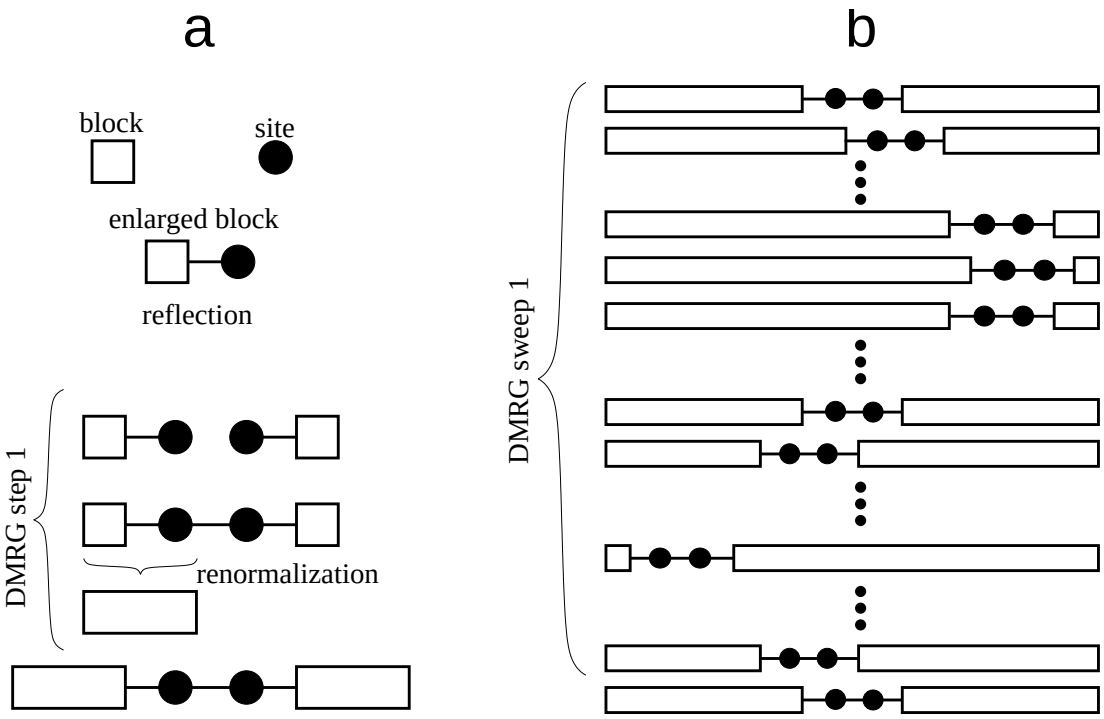

Figure B.1: Schematic procedure for the DMRG algorithm. On the left part (a) one iteration of the infinite-system DMRG algorithm is shown: starting from the system block $\mathcal{B}(L, m_L)$ and adding one free site to it, the enlarged block $\mathcal{B}(L, m_L) \bullet$ is formed. Here for simplicity we assume that the system is reflection-symmetric, thus the environmental right block is taken equal to the left block. Then, after having created the super-block $\mathcal{B}(L, m_L) \bullet \bullet \mathcal{B}(L, m_L)$, a renormalization procedure is applied in order to get the new block for the next DMRG iteration.
On the right part (b) the scheme of a complete finite-system DMRG sweep is depicted.

5. Renormalize all the relevant operators with the matrix $\hat{O}_{L \to L+1}$, thus obtaining $\mathcal{B}(L+1, m_{L+1})$.

Notice that at each DMRG step the ground state of a chain whose length grows by two sites is found. By contrast, the number of states describing a block is always m, regardless of how many sites it includes. This means that the complexity of the problem is a priori fixed by m and D (while D is imposed by the structure of the simulated system, $m \geq D$ is a parameter

which has to be appropriately set up by the user, in order to get the desired precision for the simulation; see also Sec. B.4). In Sec. B.5 we will discuss how it is possible to extract the ground state of the super-block Hamiltonian without finding its entire spectrum, by means of efficient numerical diagonalization methods like Davidson or Lanczos algorithms. We stress that at each DMRG step a truncation error $\epsilon_{\rm tr}$ is introduced:

$$\epsilon_{\rm tr} = \sum_{i>m} \lambda_i \tag{B.9}$$

where λ_i are the eigenvalues of the reduced density matrix ρ_L in decreasing order. The error $\epsilon_{\rm tr}$ is the weight of the eigenstates of ρ_L not selected for the new block basis. In order to perform a reliable DMRG simulation, the parameter m should be chosen such that $\epsilon_{\rm tr}$ remains small, as one further increases the system size. Usually one should keep $\epsilon_{\rm tr} < 10^{-6}$. For critical 1D systems $\epsilon_{\rm tr}$ decays as a function of m with a power law, while for 1D systems away from criticality it decays exponentially, thus reflecting the entanglement properties of the system in the two regimes: a critical system is more entangled, therefore more states have to be taken into account.

B.1.2 Finite-system DMRG

The output of the infinite-system algorithm described before is the (approximate) ground state of an "infinite" 1D chain. In other words, one increases the length of the chain by iterating DMRG steps, until a satisfactory convergence is reached. However, for many problems, infinite-system DMRG does not yield results accurate up to the wanted precision. For example, the strong physical effects of impurities or randomness in the Hamiltonian cannot be properly accounted for by infinite-system DMRG, as the total Hamiltonian is not yet known at intermediate steps. Moreover, in systems with strong magnetic fields, or close to a first order transition, one may be trapped in a metastable state favoured for small sizes (e.g. by edge effects).

Finite-system DMRG manages to eliminate such effects to a very large

degree, and to reduce the error almost to the truncation error [Whi92]. The idea of the finite-system DMRG algorithm is to stop the infinite-system algorithm at some preselected super-block length $L_{\max}$, which is subsequently kept fixed. In the following DMRG steps one applies the steps of infinite-system DMRG, but only one block is increased in size while the other is shrunk, thus keeping the super-block size constant. Reduced basis transformations are carried out only for the growing block.

When the infinite-system algorithm reaches the desired system size, the system is formed by two blocks $\mathcal{B}(L_{\max}/2-1,m)$ and two free sites, as shown in the first row of Fig. B.1b. The convergence is then enhanced by the so called "sweep procedure". This procedure is illustrated in the sequent rows of Fig. B.1b. It consists in enlarging the left block with one site and reducing the right block correspondingly in order to keep the length fixed. In other words, after one finite-system step the system configuration is $\mathcal{B}(L_{\max}/2,m)\bullet\bullet\mathcal{B}(L_{\max}/2-2,m)$ (where $\bullet$ represents the free site). While the left block is constructed by enlarging $\mathcal{B}(L_{\max}/2-1,m)$ with the usual procedure, the right block is taken from memory, as it has been built in a previous step of the infinite procedure and saved. Indeed, during the initial infinite-system algorithm one should save the matrices $\hat{O}_{i\to i+1}$, the block Hamiltonians $\hat{H}_B(i)$ and the interaction operators $\hat{S}_i(q)$ for $i=1,L_{\max}/2-1$. The finite-system procedure goes on increasing the size of the left block until the length $L_{\max}-4$ is reached. At this stage a right block $\mathcal{B}(1,D)$ with one site is constructed from scratch and the left block $\mathcal{B}(L_{\max}-3,m)$ is obtained through the renormalization procedure. Then, the role of the left and right block are switched and the free sites start to sweep from right to left. Notice that at each step the renormalized block $\mathcal{B}(i,m_i)$ has to be stored in memory. During these sweeps the length of the chain does not change, but the approximation of the ground state improves. Usually two or three sweeps are sufficient to reach convergence in the energy output.

Up to now we concentrated on a single quantum state, namely the ground state. It is also possible to find an approximation to a few number of states

(typically less than 5): for example, the ground state and some low-excited state [Whi92]. These states are called *target states*. At each DMRG step, after the diagonalization, for each target state ψ_k one has to calculate the corresponding reduced density matrix ρ_k, by tracing the right enlarged block. Then a convex sum of these matrices with equal weights [Sch05a] is performed:

$$\rho = \frac{1}{n_k} \sum_{k=1}^{n_k} \rho_k \tag{B.10}$$

Finally ρ has to be diagonalized in order to find the eigenbasis and the transformation matrices $\hat{O}$. In this way the DMRG algorithm is capable of efficiently representing not only the Hilbert space "around" the ground state, but also the surroundings of the other target states. It is worth noting that targeting many states reduces the efficiency of the algorithm because a larger m has to be used for obtaining the same accuracy. An alternative way could be to run as many iterations of DMRG with a single target state as many states are required.

B.1.3 Boundary conditions

The DMRG algorithm, as it has been depicted above, describes a system with open boundary conditions. However, from a physical point of view, periodic boundary conditions are normally highly preferable to the open ones, as surface effects are eliminated and finite-size extrapolation gives better results for smaller system sizes. In the presented form, the DMRG algorithm gives results much less precise in the case of periodic boundary conditions than for open boundary conditions [CP00, VPC04b, Sch05a]. Nonetheless, periodic boundary conditions can be implemented by using the super-block configuration $\mathcal{B} \bullet \mathcal{B} \bullet$. This configuration is preferred over $\mathcal{B} \bullet \bullet \mathcal{B}$ because the two blocks are not contiguous.

B.2 Measure of observables

Besides the energy, DMRG is also capable to extract other characteristic features of the target states, namely to measure the expectation values of a generic quantum observable $\hat{M}$. Properties of the $L_{\max}$-site system can be obtained from the wave functions $|\psi\rangle$ of the super-block at any point of the algorithm, although heymmetric configuration (wi0.649399(h)1.97448.942(f)-1.94207(r)-0.649399
.95024(e)-327477.436(m)2.92434(o)-2.26269(s)4.79289(t)-281.672(a)-2.26269(c)3.56352(c)3.56148(u)1.9482(r)-0.64735

B.1.1, step 4), in order to evaluat327477.436(e)3.56148(x)4.86232(p)-28.124
in which i is one of the two ase is the a simple averh ge:

$$\langle\psi|\hat{M}(i)|\psi\rangle = \psi^*_{a\alpha\beta b}\, M(i)_{\alpha\alpha'}\, \psi_{a\alpha'\beta b} \tag{B.11}$$

where i is the first free site. In the special cases in whiche ables refer to the extreme sites ($i = 1$ or $i = L_{\max}$), the measurement is perhorhed when the shortest block is $\mathcal{B}(1, D)$, following the same procedure.

It is also possible to measure an observableexpectation val ue while perh forming the infinite-system algorithm. In this case therh are two possibilities: either i is one of the two cent he measurement is perforhed as the latter, while hould express $\hat{M}$ in the truncat323.5625(d)-429.639(D)-5.02365(M)3.87393(R)27.9895(G)-426.159(b)1.9482(a)-2.26269(s)
upda$\hat{M}(i)$ in ts the new basis using the $\hat{O}$ matrix, as in Eq. (B.8):

$\hat{M}(i) \longrightarrow \hat{O}^\dagger \hat{M}(i) \hat{O}$. The measurement is then computed as:

$$\langle\hat{M}(i)\rangle = \psi^*_{a\alpha\beta b}\, M_{aa'}\, \psi_{a'\alpha\beta b} \tag{B.12}$$

if site i belongs to the left block and analogously if i belongs to the right block.

For non local observables, like a correlation function $\hat{P}(i)\,\hat{Q}(j)$, the evaluation of expectation values depends on whether i and j are on the same block or not. The most convenient way in order to perform such type of measurements is to use the finite-system algorithm. Let us first consider the case of nearest neighbor observables $\hat{P}(i)$ and $\hat{Q}(i+1)$. We can measure the expectation value $\langle \hat{P}(i)\,\hat{Q}(i+1)\rangle$ when i and $i+1$ are the two free sites. In this case the dimensions of the matrices $\hat{P}$ and $\hat{Q}$ are simply $(D \times D)$ and we do not have to store these operators in block representation. The explicit calculation of this observable is then simply:

$$\langle \hat{P}(i)\,\hat{Q}(i+1)\rangle = \psi^*_{a\alpha\beta b}\, P_{\alpha\alpha'}\, Q_{\beta\beta'}\, \psi_{a\alpha'\beta' b}\,. \tag{B.13}$$

In general, measures like $\langle \hat{P}(i)\,\hat{Q}(j)\rangle$ (where i and j are not nearest neighbor sites) can also be evaluated. This task can be accomplished by firstly storing the block representation of $\hat{P}(i)$ and $\hat{Q}(j)$, and then by performing the measure when i belongs to a block and j is a free site or vice-versa. Analogously, it is possible to evaluate measures in the case when i belongs to the left block, while j to the right one. What should be avoided is the measure of $\langle \hat{P}(i)\,\hat{Q}(j)\rangle$ when i and j belong to the *same* block. The reason is that, due to the truncation, the representation of the product $\hat{P}(i)\,\hat{Q}(j)$ is imprecise. To overcome this difficulty one can use the compound operators as described in [Whi92, Sch05a].

Finally, we stress that usually the convergence of measurements is slower than that of energy, since more finite-system DMRG sweeps are required in order to have reliable measurement outcomes (typically between five and ten).

B.3 Time dependent DMRG

In this section we describe an extension of the static DMRG, which incorporates real time evolution into the algorithm. Various different time-dependent simulation methods have been recently proposed [WF04, Vid03, DKSV04,

CM02, CM03], but here we restrict our attention to the algorithm introduced by White and Feiguin [WF04].

The aim of the time-dependent DMRG algorithm (t-DMRG) is to simulate the evolution of the ground state of a nearest-neighbor one dimensional system described by a Hamiltonian $\hat{H}$, following the dynamics of a different Hamiltonian $\hat{H}_1$. In few words, the algorithm starts with a finite-system DMRG, in order to find an accurate approximation of the ground state $|\psi\rangle_G$ of $\hat{H}$. Then the time evolution of $|\psi\rangle_G$ is implemented, by using a Suzuki-Trotter decomposition [Suz76, Tro59] for the time evolution operator $\hat{U} = e^{-i\hat{H}_1 t}$.

The DMRG algorithm gives an approximation to the Hilbert subspace that better describes the state of the system. However, during the evolution the wave function changes and explores different parts of the Hilbert space. Thus, the truncated basis chosen to represent the initial state will be eventually no more accurate. This problem is solved by updating the truncated bases during the evolution. The first effort, due to Cazalilla and Marston, consists in enlarging the effective Hilbert space, by increasing m, during the evolution [CM02, CM03]. However, this method is not very efficient because if the state of the system travels sufficiently far from the initial subspace, its representation becomes not accurate, or m grows too much to be handled. Another solution has been proposed in [WF04]: the block basis should be updated at each temporal step, by adapting it to the instantaneous state. This can be done by repeating the DMRG renormalization procedure using the instantaneous state as the target state for the reduced density matrix.

In order to approximately evaluate the evolution operator $\hat{U} = e^{-i\hat{H}_1 t}$ we use a Suzuki-Trotter decomposition [Suz76, Tro59]. The first order expansion in time is given by the formula:

$$e^{-i\hat{H}_1 t} \approx \left(\prod_{L=1}^{L_{\max}-1} e^{-i\hat{H}_1(L,L+1)dt} \right)^n , \tag{B.14}$$

where $n = t/dt$ gives the discretization of time t in small intervals dt, and

$\hat{H}_{L,L+1}$ is the interaction Hamiltonian (plus the local terms) between site L and $L+1$. Further decompositions at higher orders can be obtained by observing that the Hamiltonian can be divided in two addends: the first, $\hat{F} = \sum_{L\,\mathrm{even}} \hat{H}_1(L, L+1)$, containing only even bonds, and the second $\hat{G} = \sum_{L\,\mathrm{odd}} \hat{H}_1(L, L+1)$, containing only odd bonds. Since the terms in $\hat{F}$ and $\hat{G}$ commute, an even-odd expansion can be performed:

$$e^{-i\hat{H}_1 t} \approx \left(e^{-i\hat{F}\frac{dt}{2}}\, e^{-i\hat{G}dt}\, e^{-i\hat{F}\frac{dt}{2}}\right)^n . \tag{B.15}$$

This coincides with a second order Trotter expansion, in which the error is proportional to dt^3. Of course, one can enhance the precision of the algorithm by using a fourth order expansion with error dt^5 [Sch05b]:

$$e^{-i\hat{H}t} = \prod_{i=1}^{5} \left(e^{-ip_i\,\hat{F}\,\frac{dt}{2}}\, e^{-ip_i\,\hat{G}\,dt}\, e^{-i\,p_i\,\hat{F}\,\frac{dt}{2}}\right)^n + O(dt^5)\,, \tag{B.16}$$

where all $p_i = 1/(4 - 4^{1/3})$, except $p_3 = 1 - 4p_1 < 0$, corresponding to evolution backward in time.

Nonetheless, the most serious error in a t-DMRG program remains the truncation error. A nearly perfect time evolution with a negligible Trotter error is completely worthless if the wave function is affected by a relevant truncation error. It is worth to mention that t-DMRG precision becomes poorer and poorer as time grows larger and larger, due to the accumulated truncation error at each DMRG step. This depends on $L_{\max}$, on the number of Trotter steps and, of course, on m. At a certain instant of time, called the *runaway time*, the t-DMRG precision decreases by several order of magnitude. The runaway time increases with m, but decreases with the number of Trotter steps and with $L_{\max}$. For a more detailed discussion on the t-DMRG errors and on the runaway time, see Gobert et al. [GKSS05].

The initial wave function $|\psi\rangle_G$ can be chosen from a great variety of states. As an example, for a spin 1/2 chain, a factorized state can be prepared by means of space dependent magnetic fields. In general, it is also possible to start with an initial state built up by transforming the ground state as

$|\psi\rangle_A = \sum_{i=1}^{L_{\max}} \hat{A}_i |\psi\rangle_G$, where $\hat{A}_i$ are local operators. The state $|\psi\rangle_A$ can be obtained by simply performing a preliminary sweep, just after the finite-system procedure, in which the operators $\hat{A}_i$ are subsequently applied to the transforming wave function, when i is a free site [WF04].

In summary, the t-DMRG algorithm is composed by the following steps:

1. Run the finite-system algorithm, in order to obtain the ground state $|\psi\rangle_G$ of H.

2. If applicable, perform an initial transformation in order to set up the initial state $|\psi\rangle_A$.

3. Keep on the finite-system procedure by performing sweeps in which at each step the operator $e^{-i\hat{H}_1(L,L+1)dt}$ is applied to the system state (L and $L+1$ are the two free sites for the current step).

4. Perform the renormalization, following the finite-system algorithm, and store the matrices $\hat{O}$ for the following steps.

5. At each step change the state representation to the new DMRG basis using White's state prediction transformation [Whi96] (see below).

6. Repeat points 3 to 5, until a complete dt time evolution has been computed.

White's prediction transformation is computed as follows: at any DMRG, one has the left block $\mathcal{B}(L-1,m)$ and right block $\mathcal{B}(L_{\max}-L-1,m)$ description. To transform a quantum state $|\psi\rangle$ of the system in the new basis for the next step (corresponding to the blocks $\mathcal{B}(L,m)$ and $\mathcal{B}(L_{\max}-L-2,m)$) one uses the matrices $\hat{O}$: $\hat{O}_{L-1\to L}$ and $\hat{O}^{\dagger}_{L_{\max}-L-2\to L_{\max}-L-1}$. The first matrix transforms a block of length $L-1$ in a block of length L and it has been computed in the current renormalization. The second one transforms a block of length $L_{\max}-L-1$ in a block of length $L_{\max}-L-2$; this matrix is recovered from memory, since it has been computed at a previous step. The

transformed wave function then reads:

$$\tilde{\psi}_{a\alpha\beta b} = O^{*\,g(a',\alpha')\,a}_{L-1\to L}\; O^{g(\beta,b)\,b'}_{L_{\max}-L-2\to L_{\max}-L-1}\; \psi_{a'\alpha'\alpha b'}\,. \tag{B.17}$$

To compute the system time evolution using the second order Trotter expansion of Eq. (B.15), one should perform 3/2 sweeps for each time interval dt: in the first $e^{-i\hat{F}\frac{dt}{2}}$ is applied, in the second $e^{-i\hat{G}dt}$, finally a third half sweep is needed to apply $e^{-i\hat{F}\frac{dt}{2}}$ again. Since at each step the operator $e^{-i\hat{H}_1(L,L+1)dt}$ is computed on the two current free sites L and $L+1$, its representation is given in terms of a $D^2 \times D^2$ matrix, and most remarkably it is exact. As stated before, to increase the simulation precision, one can expand the time evolution operator to the fourth order as in Eq. (B.16). The implementation of this expansion requires $5 \cdot \frac{3}{2}$ sweeps; thus the computational time is five times longer than the one needed using Eq. (B.15).

Finally, we remark that this algorithm for the time evolution is a small modification of the finite-system algorithm: the main difference is the computation of a factor of the Trotter expansion instead of performing the diagonalization procedure at each step. Notice that the measurements are performed in the same way as in the finite-system algorithm.

B.4 Numerical examples

In this section we report some numerical examples on the convergence of the DMRG outputs with respect to the user fixed parameters m, and (t, dt). Let us first focus on the static DMRG algorithm. The main source of error is due to the step-by-step truncation of the Hilbert space dimension of the system block from $m \times D$ to m. The parameter m then must be set up very carefully, since it represents the maximum number of states used to describe the system block. It is clear that, by increasing m, the output becomes closer and closer to the exact solution, which is eventually reached in the limit of $m \sim D^L$ (in that case the algorithm would no longer perform truncation, and the only source of error would be due to inevitable numerical roundoffs).

As an example of the output convergence with m, in Fig. B.2 we plotted the behavior of the ground state energy in the one-dimensional spin 1 Bose-Hubbard model as a function of m (see chapter 6 for a detailed description of the physical system). The convergence is exponential with m as can be seen in the figure. In the inset the CPU-time dependence with m is shown and the dashed line shows a power law fit of data, m^{α} with $\alpha \sim 3.2$.

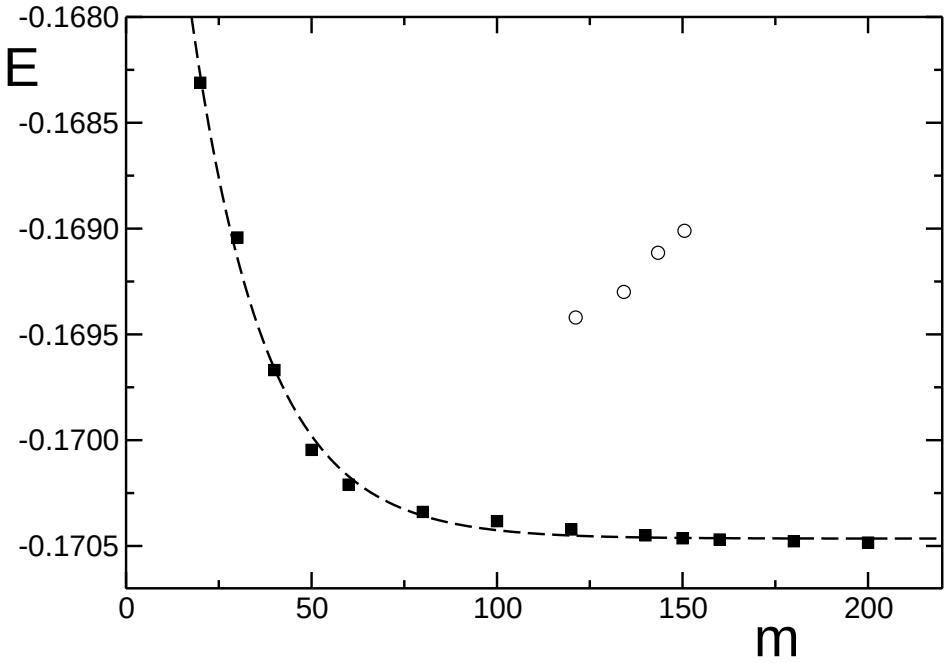

with the Hamiltonian of the XX model from an initial product state to an entangled one. This entanglement can be measured by the von Neumann entropy of the reduced density matrix of the block $\rho(t)$:

$$S(t) = -\mathrm{Tr}\rho(t)\log_2\rho(t) \tag{B.18}$$

In the example we calculate $S(t)$ for a block of size 6 in a chain of length 50. The time evolution has been calculated form $t = 0$ to $t = 3$ with a fixed Trotter time step $dt = 5 \cdot 10^{-2}$ that ensures that the Trotter error is negligible with respect to the truncation error. Since the XX model can be

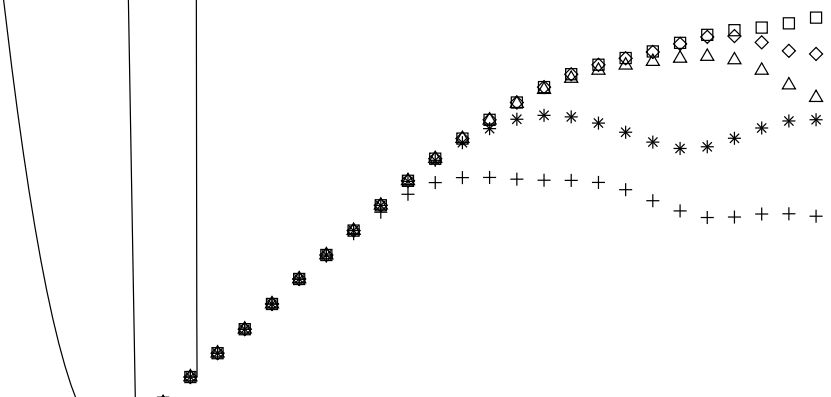

the CPU-time as a function of m, which behaves as a power-law m^{α} with $\alpha \sim 3.14$, confirming the estimate given in the inset of Fig. B.2. The deviation $\varepsilon = |S_{\text{exact}} - S_m|/S_m$ as a function of m and of time is shown in Fig. B.4. The typical fast convergence of the DMRG result with m is recovered only when m is greater than a critical value m_c (two distinct regimes are clear in Fig. B.4). This is due to the amount of entanglement present in the system: an estimate of the number of states needed for an accurate description is given by $m_c \propto 2^{S(t)}$. Thus, it is always convenient to keep track of entropy to have an initial guess for the number of states needed to describe the system [GKSS05]. On the other hand, if m is increased too much, the Trotter error will dominate and smaller dt is needed to improve accuracy.

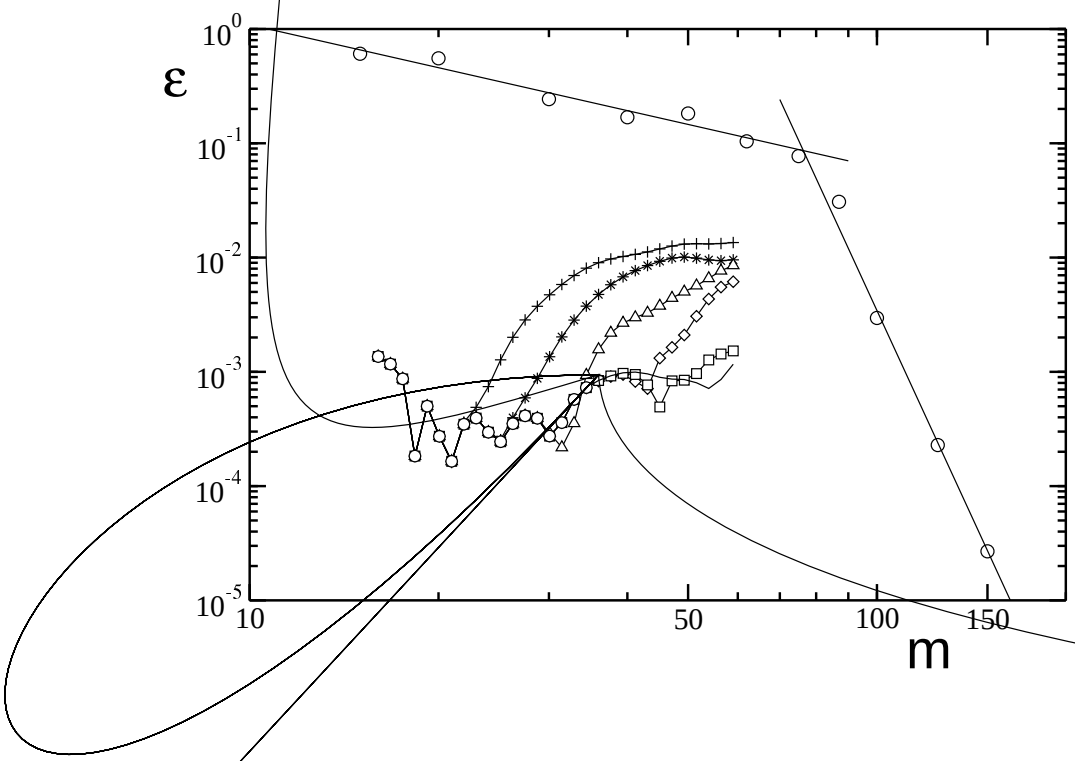

B.5 Technical issues

In this section we explain some technicalities regarding the implementation of DMRG and t-DMRG code. They are not essential in order to understand the algorithm, but they can be useful to anyone who wants to write a code from scratch, or to modify the existing ones. Some of these parts can be differently implemented, in part or completely skipped, depending on the computational complexity of the physical system under investigation.

B.5.1 Hamiltonian diagonalization

The ground state of the Hamiltonian is typically found by diagonalizing a matrix of dimensions $(m\,D)^2 \times (m\,D)^2$. Typically the DMRG algorithm is used when one is only interested in the the ground state properties (at most in few low-energy eigenstates). The diagonalization can thus be greatly optimized by using Lanczos or Davidson methods: these are capable to give a small number ($\lesssim 10$) of eigenstates close to a previously chosen target energy in much less time than exact diagonalization routines. Moreover they are optimized for large sparse matrices, (that is the case of typical super-block Hamiltonians) and they do not require as input the full matrix. What is needed is just the effect of it on a generic state ψ, which lives in a $(mD)^2$ dimensional Hilbert space. The Hamiltonian Eq. (B.1) can be written as:

$$\hat{H} = \sum_p \hat{A}(p) \otimes \hat{B}(p)\,, \tag{B.19}$$

where $\hat{A}(p)$ and $\hat{B}(p)$ act respectively on the left and on the right enlarged block. Thus, only this matrix multiplication has to be implemented:

$$\psi^{\text{out}}_{a\alpha\beta b} = \sum_p \hat{A}(p)^{\,g(a,\alpha)\,g(a',\alpha')}\ \hat{B}(p)^{\,g(b,\beta)\,g(b',\beta')}\ \psi^{\text{in}}_{a'\alpha'\beta'b'} \tag{B.20}$$

In this way it is possible to save a great amount of memory and number of operations, since the dimensions of $\hat{A}(p)$ and $\hat{B}(p)$ are $(m\,D) \times (m\,D)$, and not $(m\,D)^2 \times (m\,D)^2$. As an example, the typical m value for simulating the

evolution of a $L_{\max} = 50$ spin 1/2 chain ($D = 2$) is $m \sim 50$. This means that, in order to store all the $\sim 10^8$ complex numbers of $\hat{H}_{supB}$ in double precision, ~ 1.6 Gbytes of RAM is needed. Instead, each of the two matrices $\hat{A}$ and $\hat{B}$ requires less than 200 kbytes of RAM.

B.5.2 Guess for the wave function

Even by using the tools described in the previous paragraph, the most time consuming part of a DMRG step remains the diagonalization procedure. The step-to-step wave function transformation required for the t-DMRG algorithm, which has been described in the previous section, can also be used in the finite-system DMRG, in order to speed up the super-block diagonalization [Whi96]. Indeed the Davidson or Lanczos diagonalization methods are iterative algorithms which start from a generic wave function, and then recursively modify it, until the eigenstate closest to the target eigenvalue is reached (up to some tolerance value, fixed from the user). If a very good initial guess is available for the diagonalization procedure, the number of steps required to converge to the solution can be drastically reduced and the time needed for the diagonalization can be reduced up to an order of magnitude.

In the finite-system algorithm the system is changing much less than in the infinite algorithm, and an excellent initial guess is found to be the final wave function from the previous DMRG step, after it has been written in the new basis for the current step. White's prediction is used in order to change the basis of the previous ground state with the correct operators $\hat{O}$, as in Eq. (B.17). It is also possible to speed up the diagonalization in the infinite-system algorithm, but here the search for a state prediction is slightly more complicated (see e.g. [Sch98, SZQL02]).

B.5.3 Symmetries

If the system has a global reflection symmetry, it is possible to take the environment block equal to the system block, in the infinite-system procedure. Namely, the right enlarged block is simply the reflection of the left one. To avoid the complication of the reflection we can consider an alternative labelling of the sites, as shown in Fig. B.5. In this case left and right enlarged blocks are represented by exactly the same matrix.

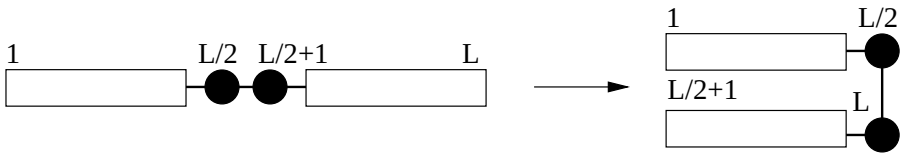

Figure B.5: Alternative labelling of sites, to be used in the environment reflection procedure (in case of globally reflection-symmetric systems).

If other symmetries hold, for example conservation of angular momentum or particle number, it is possible to take advantage of them, such to considerably reduce the CPU-time for diagonalization. The idea is to rewrite the total Hamiltonian in a block diagonal form, and then separately diagonalize each of them. If one is interested in the ground state, he simply has to compare the ground state energies inside each block, in order to find the eigenstate corresponding to the lowest energy level. One may also be interested only in the ground state with given quantum numbers (for example in the Bose-Hubbard model one can search for the system ground state with a given number of particles), in this case the diagonalization of the block Hamiltonian corresponding to the wanted quantum numbers is sufficient. In order to write the Hamiltonian in block diagonal form the eigenstates of the reduced density matrix have to be labelled according to the various quantum numbers. Attention must be paid when truncating to the reduced basis: it is of crucial importance to retain whole blocks of eigenstates with the same weight, inside a region with given quantum numbers. This helps in avoiding unwanted artificial symmetry breaking, apart from numerical roundoff errors.

B.5.4 Sparse Matrices

Operators typically involved in DMRG-like algorithms (like block Hamiltonians, updating matrices, observables) are usually represented by sparse matrices. A well written programming code takes advantage of this fact, thus saving large amounts of CPU-time and memory. Namely, there are standard subroutines which list the position (row and column) and the value of each non null element for a given sparse matrix.

B.5.5 Storage

Both the static and the time dependent DMRG require to store a great number of operators: the block Hamiltonian, the updating matrices, and if necessary the observables for each possible block length. One useful way to handle all these operators is to group each of them in a register, in which one index represents the length of the block. Operatively, we store all these operators in the fast-access RAM memory. However, for very large problems one can require more than the available RAM, therefore it is necessary to store these data in the hard disk. The read/write operations from hard disk dramatically slow down a program performance, thus they should be avoided, if possible.

B.5.6 Algorithm Schemes

Figures B.6-B.7 show a schematic representation of DMRG and t-DMRG code.

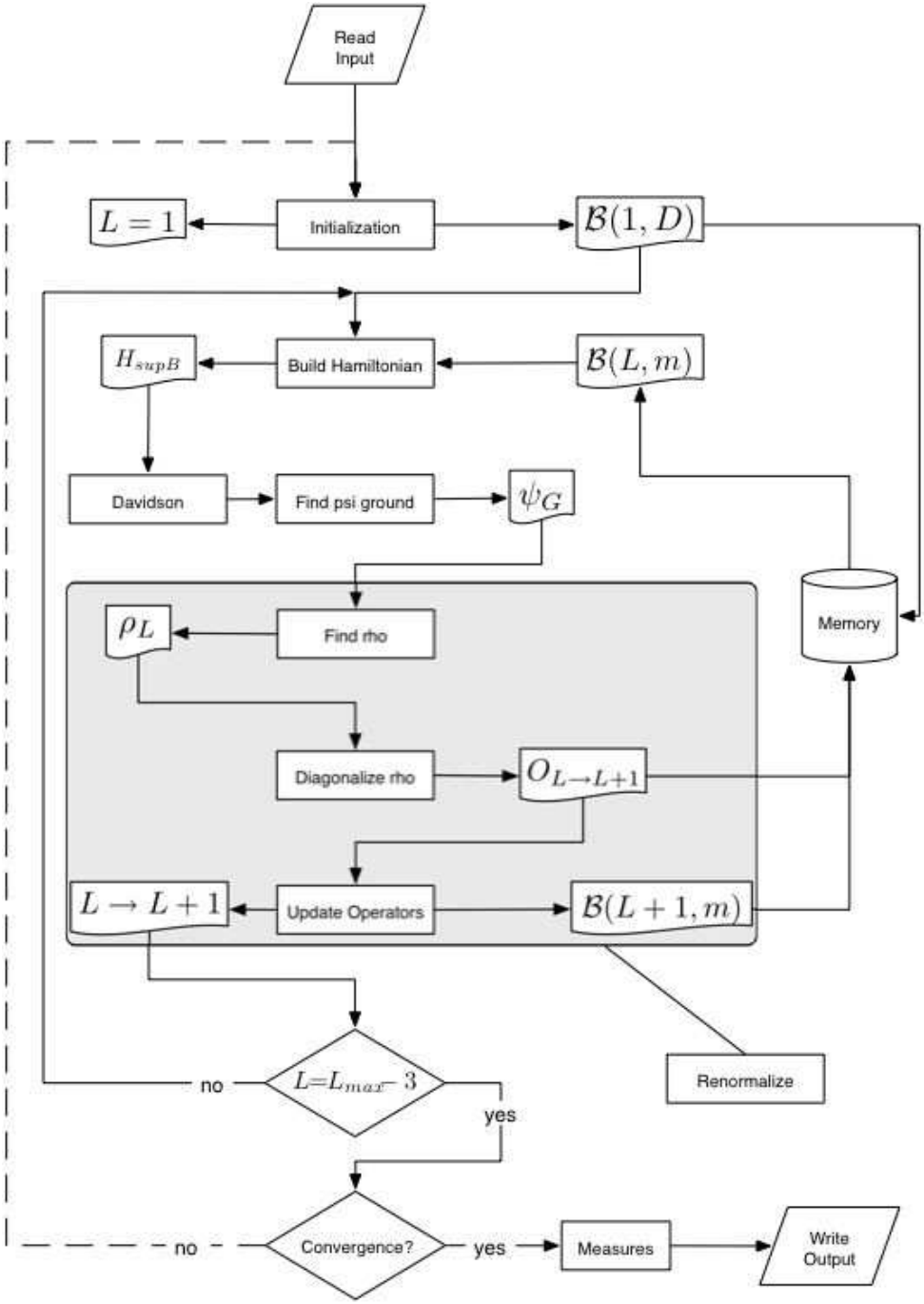

Figure B.6: Basic scheme of the infinite/finite DMRG algorithm. Here we have supposed, for simplicity, that the system is globally reflection symmetric (thus the environment block is taken equal to the system block). The shadowed rectangle is the basic renormalization stage that will be used also in the t-DMRG algorithm (see Fig. B.7).

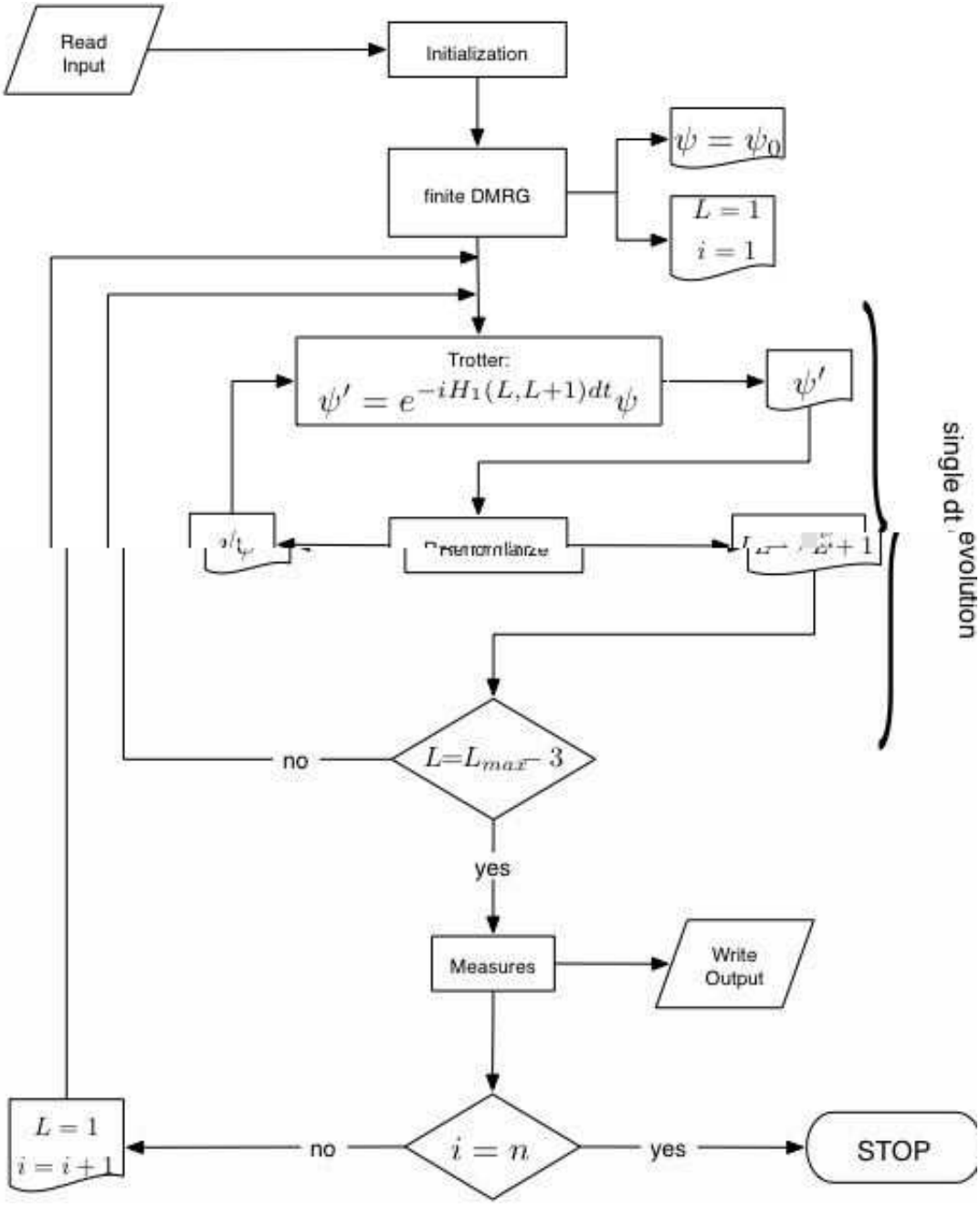

Figure B.7: Basic scheme of the time-dependent DMRG algorithm. The index i refers to the discretized time and $n = t/dt$.

Appendix C

Calculus of the entropy for the XX model

For completeness in this appendix we sketch how to calculate the entropy for the XX model with *open* boundary conditions. For $\Delta = 0$ the Hamiltonian Eq. (8.1) can be rewritten, using the Jordan-Wigner transformation [LM66], as:

$$H = 2\sum_{j=1}^{N-1} J_j \left(c_j^\dagger c_{j+1} + h.c. \right) \tag{C.1}$$

where $c_j^\dagger = (\sigma_x^j - i\sigma_y^j)$. It is possible to rewrite Hamiltonian Eq. (C.1) in diagonal form

$$H = \sum_{k=1}^{N} E_k b_k^\dagger b_k \tag{C.2}$$

where the new ladder operators are connected to the old ones with an orthonormal transformation:

$$b_k = \sum_{j=1}^{N} a_{kj} c_j \tag{C.3}$$

The matrix $\{a_{kj}\}$ contains the normalized eigenvectors of the $N \times N$ adjacency matrix $\{J_{kj}\}$ whose elements are defined as $J_{1j} = 2J_1\delta_{j,2}$, $J_{Nj} = 2J_{N-1}\delta_{j,N-1}$ $J_{kj} = 2J_k\delta_{k,j+1} + 2J_{k-1}\delta_{k,j-1}$ for $k = 2, \ldots, N-1$.

To calculate the entropy of a block of size ℓ we use [Laf05]:

$$S = -\sum_{\alpha=1}^{\ell} \lambda_\alpha \log_2 \lambda_\alpha + (1-\lambda_\alpha)\log_2(1-\lambda_\alpha) \tag{C.4}$$

where λ_α are the eigenvalues of the correlation matrix $C_{ij} = \langle c_i^\dagger c_j \rangle, \quad i,j = 1,\ell$.

As an example we consider the time dependence of the block entropy after a quench from $\Delta_0 = \infty$ to $\Delta_1 = 0$. The initial state is the antiferromagnetic state:

$$|\psi_0\rangle = c_1^\dagger c_3^\dagger \cdots c_{N-1}^\dagger |0\rangle \tag{C.5}$$

The correlations are easily evaluated using the transformation $\{a_{kj}\}$ with the result

$$\begin{aligned}
\langle c_i^\dagger(t) c_j(t)\rangle &= \sum_{k,k'} a_{ik} a_{jk'} e^{-i(E_k - E'_k)t} \langle \psi_0 | b_k^\dagger b_{k'} | \psi_0 \rangle = \\
&= \sum_{k,k'} \sum_{i'j'} a_{ik} a_{jk'} a^*_{i'k} a^*_{j'k'} e^{-i(E_k - E'_k)t} \langle \psi_0 | c_{i'}^\dagger c_{j'} | \psi_0 \rangle = \\
&= \sum_{k,k'} \sum_{i'=1,3}^{N-1} a_{ik} a_{jk'} a^*_{i'k} a^*_{i'k'} e^{-i(E_k - E'_k)t}
\end{aligned} \tag{C.6}$$

By using Eq.(C.6) to calculate the eigenvalues of the correlation matrix, the block entropy in readily evaluated from Eq.(C.4). For example when the chain is homogeneous $J_i = J$ we obtain:

$$a_{kj} = \sqrt{\frac{2}{N+1}} \sum_{j=1}^{N} \sin kj \tag{C.7}$$

and the corresponding energy levels are $E_k = 4J\cos k_n$ where $k_n = (\pi n)/(N+1), \quad n = 1,2,\ldots,N$.

Bibliography

[ABV01] M. C. Arnesen, S. Bose, and V. Vedral, Phys. Rev. Lett. **87** (2001), 017901.

[ACDE04] C. Albanese, M. Christandl, N. Datta, and A. Ekert, Phys. Rev. Lett. **93** (2004), 230502.

[AE74] J. R. Ackeralt and J. H. Eberly, Phys. Rev. D **10** (1974), 3350.

[AF03] D.V. Averin and R. Fazio, JETP Lett. **78** (2003), 664.

[AGMT05] A. Anfossi, P. Giorda, A. Montorsi, and F. Traversa, Phys. Rev. Lett. **95** (2005), 056402.

[AK98] B.P. Anderson and M.A. Kasevich, Science **281** (1998), 1686.

[AKE04] E. J. Amanatidis, D. E. Katsanos, and S. N. Evangelou, Phys. Rev. B **69** (2004), 195107.

[AOP+04] L. Amico, A. Osterloh, F. Plastina, R. Fazio, and G. M. Palma, Phys. Rev. A **69** (2004), 022304.

[Ave00] D. V. Averin, Fortsch. Physik **48** (2000), 1055.

[BB84] C. H. Bennett and G. Brassard, Proceedings of IEEE International Conference on Computers Systems and Signal Processing, IEEE Press, New York, California, 1984, p. 175.

[BB03] S. C. Benjamin and S. Bose, Phys. Rev. Lett. **90** (2003), 0247901.

[BB05] D. Burgarth and S. Bose, Phys. Rev. A **71** (2005), 052315.

[BBC+93] C. H. Bennett, G. Brassard, C. Crépau, R. Jozsa, A. Peres, and W. Wootters, Phys. Rev. Lett. **70** (1993), 1895.

[BBC+95] A. Barenco, C.H. Bennett, R. Cleve, D.P. DiVicenzo, N. Margolus, P. Shor, T. Sleator, J. Smolin, and H. Weinfurter, Phys. Rev. A **52** (1995), 3457.

[BBHB97] V. Bužek, S.L. Braunstein, M. Hillery, and D. Bruß, Phys. Rev. A **56** (1997), 3446.

[BCDM00] D. Bruß, M. Cinchetti, G. M. D'Ariano, and C. Macchiavello, Phys. Rev. A **62** (2000), 012302.

[BCF+01] S. Burger, F. S. Cataliotti, C. Fort, F. Minardi, M. Inguscio, M. L. Chiofalo, and M. P. Tosi, Phys. Rev. Lett. **86** (2001), 4447.

[BCMS01a] G. Benenti, G. Casati, S. Montangero, and D. L. Shepelyansky, Phys. Rev. Lett. **87** (2001), 227901.

[BCMS01b] G. Benenti, G. Casati, S. Montangero, and D. L. Shepelyansky, Phys. Rev. Lett. **87** (2001), 227901.

[BCS04] G. Benenti, G. Casati, and G. Strini, *Principles of quantum computation and information*, World Scientific, 2004.

[BDE+98] D. Bruß, D. P. DiVincenzo, A. Ekert, C. A. Fuchs, C. Macchiavello, and J. A. Smolin, Phys. Rev. A **57** (1998), 2368.

[BDE+04] D. Bruß, N. Datta, A. K. Erkert, L. C. Kwek, and C. Macchiavello, http://www.arxiv.org/abs/quant-ph/0411080, 2004.

[BDM05] F. Buscemi, G. M. D'Ariano, and C. Macchiavello, Phys. Rev. A **71** (2005), 042327.

[BEM98] D. Bruß, A. Ekert, and C. Macchiavello, Phys. Rev. Lett. **81** (1998), 2598.

[Ber84] M. V. Berry, Proc. Roy. Soc. A **392** (1984), 47, Reprinted in [SW89].

[Ber96] M. V. Berry, J. Phys. A **29** (1996), 6617.

[BEZ00] D. Bouwmeester, A. Ekert, and A. Zeilinger, *The physics of quantum information*, Springer, 2000.

[BFP03] F. Benatti, R. Floreanini, and M. Piani, Phys. Rev. Lett. **91** (2003), 070402.

[BGB04] D. Burgarth, V. Giovannetti, and S. Bose, http://www.arxiv.org/abs/quant-ph/0410175, 2004.

[BH96] V. Bužek and M. Hillery, Phys. Rev. A **54** (1996), 1844.

[BL85] C.H. Bennett and R. Landauer, Scientific American **253** (1985), 48.

[Bos03] S. Bose, Phys. Rev. Lett. **91** (2003), 207901.

[BP94] Y. Brihaye and P.Kosiński, Phys. Lett. A **195** (1994), 296.

[Bra02] D. Braun, Phys. Rev. Lett. **89** (2002), 277901.

[Bru02] D. Bruß, J. Math. Phys. **43** (2002), 4237, http://www.arxiv.org/abs/quant-ph/0110078.

[BT03] A. Blais and A.-M.S. Tremblay, Phys. Rev. A **67** (2003), 012308.

[BV04] C. Brukner and V. Vedral , http://www.arxiv.org/abs/quant-ph/0406040, 2004.

[BVZ04] C. Brukner, V. Vedral, and A. Zeilinger , http://www.arxiv.org/abs/quant-ph/0410138, 2004.

[CBF+01] F. S. Cataliotti, S. Burger, C. Fort, P. Maddaloni, F. Minardi, A. Trombettoni, A. Smerzi, and M. Inguscio, Science **293** (2001), 843.

[CC04] P. Calabrese and J. Cardy, J. Stat. Mech.: Theor. Exp. **0406** (2004), P002.

[CC05] P. Calabrese and J. Cardy, J. Stat. Mech.: Theor. Exp. **0504** (2005), P010.

[CCWD05] Qing Chen, Jianhua Cheng, Ke-Lin Wang, and Jiangfeng Du, http://www.arxiv.org/abs/quant-ph/0510147, 2005.

[CDD+05] M. Christandl, N. Datta, T. C. Dorlas, A. Ekert, A. Kay, and A. J. Landahl, Phys. Rev. A **71** (2005), 032312.

[CDEL04] M. Christandl, N. Datta, A. Ekert, and A. J. Landahl, Phys. Rev. Lett. **92** (2004), 187902.

[CDG02] N.J. Cerf, T. Durt, and N. Gisin, J. Mod. Opt. **49** (2002), 1355.

[CDJ+04] T. Calarco, U. Dorner, P. S. Julienne, C. J. Williams, and P. Zoller, Phys. Rev. A **70** (2004), 012306.

[CFGSV02] A. Carollo, I. Fuentes-Guridi, M. Franca Santos, and V. Vedral, Phys. Rev. Lett. **89** (2002), 220404, *ibid* **92**, 160402 (2003).

[Chu91] A.V. Chubukov, Phys. Rev. B **43** (1991), 3337.

[CJF+02] H. K. Cummins, C. Jones, A. Furze, N. F. Soffe, M. Mosca, J. M. Peach, and J. A. Jones, Phys. Rev. Lett. **88** (2002), 187901.

[CM02] M. A. Cazalilla and J. B. Marston, Phys. Rev. Lett. **88** (2002), 256403.

[CM03] M. A. Cazalilla and J. B. Marston, Phys. Rev. Lett. **91** (2003), 049702.

[CP00] M.C. Chung and I. Peschel, Phys. Rev. B **62** (2000), 4191.

[CTDRG92] C. Cohen-Tannoudji, J. Dupont-Rac, and G. Grynberg, *Atom-photon interactions*, John Wiley & Sons, New York, 1992.

[CZWZ04] Y. Chen, P. Zanardi, Z.D. Wang, and F.C. Zhang, http://www.arxiv.org/abs/quant-ph/0407228, 2004.

[dBKS95] J. de Boer, V. E. Korepin, and A. Schadschneider, Phys. Rev. Lett. **74** (1995), 789.

[DCZ01] M.-M Duan, I. Cirac, and P. Zoller, Science **292** (2001), 1695.

[DCP03] G. De Chiara and G. M. Palma, Phys. Rev. Lett. **91** (2003), 090404.

[DDL03] L.-M. Duan, E. Demler, and M. D. Lukin, Phys. Rev. Lett. **91** (2003), 090402.

[DDZ+03] J. Du, T. Durt, P. Zou, L.C. Kwek, C.H. Lai, C.H. Oh, and A. Ekert, http://www.arxiv.org/abs/quant-ph/0311010, 2003.

[DDZ+04] J. Du, T. Durt, P. Zou, L.C. Kwek, C.H. Lai, C.H. Oh, and A. Ekert, Phys. Rev. Lett. **92** (2004), 187902.

[Deu85] D. Deutsch, Proc. R. Soc. London A **400** (1985), 97.

[DHH+05] W. Dür, L. Hartmann, M. Hein, M. Lewenstein, and H.-J. Briegel, Phys. Rev. Lett. **94** (2005), 097203.

[DiV97] D. DiVincenzo, Mesoscopic electron transport, Kluwer, 1997, http://www.arxiv.org/abs/cond-mat/9612126, p. 657.

[DiV00] D. DiVincenzo, Fort. der Phys. **48** (2000), 771.

[DKSV04] A. J. Daley, C. Kollath, U. Schollwöck, and G. Vidal, J. Stat. Mech.: Theor. Exp. (2004), P04005.

[DL03] L.M. Duan E. Demler and M. Lukin, Phys. Rev. Lett. **91** (2003), 090402.

[DLP01] G. M. D'Ariano and P. Lo Presti, Phys. Rev. A **64** (2001), 042308.

[DM03] G. M. D'Ariano and C. Macchiavello, Phys. Rev. A **67** (2003), 042306.

[DVC00] W. Dür, G. Vidal, and J. I. Cirac, Phys. Rev. A **62** (2000), 062314.

[DVC+01] W. Dür, G. Vidal, J. I. Cirac, N. Linden, and S. Popescu, Phys. Rev. Lett. **87** (2001), 137901.

[DZ02] E. Demler and F. Zhou, Phys. Rev. Lett. **88** (2002), 163001.

[EC05] J. Eisert and M. Cramer, Phys. Rev. A **72** (2005), 042112.

[EEH+00] A. Ekert, M. Ericsson, P. Hayden, H. Inamori, J. A. Jones, D. K. L. Oi, and V. Vedral, J. Mod. Opt. **47** (2000), 2501.

[Fey82] R. Feynman, Int. J. Theor. Phys. **21** (1982), 467.

[FFP+00] G. Falci, R. Fazio, G.M. Palma, J. Siewert, and V. Vedral, Nature **403** (2000), 869.

[FIMW03] H. Fan, H. Imai, K. Matsumoto, and X.-B. Wang, Phys. Rev. A **67** (2003), 022317.

[Fiu03] J. Fiurášek, Phys. Rev. A **67** (2003), 052314.

[FKR04] H. Fan, V.E. Korepin, and V. Roychowdhury, Phys. Rev. Lett. **93** (2004), 227203.

[FLS65] R. P. Feynman, R. B. Leighton, and M. Sands, *Feynman lectures on physics*, vol. 3, Addison-Wesley, Reading, MA, 1965.

[FM96] J. K. Freericks and H. Monien, Phys. Rev. B **53** (1996), 2691.

[FMWW02] H. Fan, K. Matsumoto, X.-B. Wang, and M. Wadati, Phys. Rev. A **65** (2002), 012304.

[FP02] P. Facchi and S. Pascazio, Phys. Rev . Lett. **89** (2002), 080401.

[FS95] G. Fàth and J. Sòlyom, Phys. Rev. B **51** (1995), 3620.

[FSF03] L. Faoro, J. Siewert, and R. Fazio, Phys. Rev. Lett. **90** (2003), 028301.

[FT82] E. Fredkin and T. Toffoli, Int. J. of Theor. Phys. **21** (1982), 219.

[FW05] A. E. Feiguin and S. R. White, Phys. Rev. B **72** (2005), 020404.

[FWGF89] M.P.A. Fisher, P.B. Weichman, G. Grinstein, and D.S. Fisher, Phys. Rev. B **40** (1989), 546.

[GF05] V. Giovannetti and R. Fazio, Phys. Rev. A **71** (2005), 032314.

[GHZ89] D. M. Greenberger, M. A. Horne, and A. Zeilinger, *Bell's theorem, quantum theory, and conceptions of the universe*, Kluwer, Dordrecht, 1989, p. 69.

[GKSS05] D. Gobert, C. Kollath, U. Schollwöck, and G. Schütz, Phys. Rev. E **71** (2005), 036102.

[GM97] N. Gisin and S. Massar, Phys. Rev. Lett. **79** (1997), 2153.

[GME+02] M. Greiner, O. Mandel, T. Esslinger, T.W. H'ansch, and I. Bloch, Nature **415** (2002), 39.

[GMGW98] T. Guhr, A. Müller-Groeling, and H. A. Weidenmüller, Phys. Rep. **299** (1998), 190.

[GMHB02] M. Greiner, O. Mandel, T. W. Hanscha, and I. Bloch, Nature **419** (2002), 51.

[GR06] J. J. Garcia-Ripoll, http://www.arxiv.org/abs/cond-mat/0602305, 2006.

[GRAC03] S. Ghosh, T. F. Rosenbaum, G. Aeppli, and S. N. Coppersmith, Nature **425** (2003), 48.

[GRC03] J. J. Garcia-Ripoll and J. I. Cirac, New J. Phys. **5** (2003), 74.

[GRMDC04] J. J. Garcia-Ripoll, M. A. Martin-Delgado, and J. I. Cirac, Phys. Rev. Lett. **93** (2004), 250405.

[GRTZ02] N. Gisin, G. Ribordy, W. Tittel, and H. Zbinden, Rev. Mod. Phys. **74** (2002), 145.

[GS00] B. Georgeot and D. L. Shepelyansky, Phys. Rev. E **62** (2000), 6366.

[GT05] O. Gühne and G. Toth, http://www.arxiv.org/abs/quant-ph/0510185, 2005.

[Haa91] F. Haake, *Quantum signature of chaos*, Springer-Verlag, New York, 1991.

[HB02] A. Hutton and S. Bose, Phys. Rev. A **69** (2002), 042312.

[HHH96] M. Horodecki, P. Horodecki, and R. Horodecki, Phys. Lett. A **223** (1996), 1.

[HLW94] C Holzhey, F Larsen, and F Wilczek, Nuclear Physics B **424** (1994), 443.

[HRP05] M. J. Hartmann, M. E. Reuter, and M. B. Plenio, http://www.arxiv.org/abs/quant-ph/0511185, 2005.

[HW97] S. Hill and W. K. Wootters, Phys. Rev. Lett. **78** (1997), 5022.

[IBM] See for example: http://www-03.ibm.com/servers/eserver/bladecenter/tours/js20.html.

[IJK05] A. R. Its, B.-Q. Jin, and V. E. Korepin, J. Phys. A **38** (2005), 2975.

[ILD03] A. Imambekov, M. Lukin, and E. Demler, Phys. Rev. A **68** (2003), 063602.

[ILD04] A. Imambekov, M. Lukin, and E. Demler, Phys. Rev. Lett. **93** (2004), 120405.

[Izr90] F. Izrailev, Phys. Rep. **196** (1990), 299.

[JBC+98] D. Jaksch, C. Bruder, J.I. Cirac, C.W. Gardiner, and P. Zoller, Phys. Rev. Lett. **81** (1998), 3108.

[JBC+99] D. Jaksch, H.-J. Briegel, J.I. Cirac, C. W. Gardiner, and P. Zoller, Phys. Rev. Lett. **82** (1999), 1975.

[JK04] B Q Jin and V E Korepin, J. Stat. Mech.: Theor. Exp. **116** (2004), 79.

[JVEC00] J. Jones, V. Vedral, A.K. Ekert, and C. Castagnoli, Nature **403** (2000), 869.

[JZ05] D. Jaksch and P. Zoller, Ann. Phys. **315** (2005), 52.

[Kan98] B. E. Kane, Nature **393** (1998), 133.

[Kaw02] N. Kawashima, Prog. Theor. Phys. **145** (2002), 138.

[KBDW01] J. Kempe, D. Bacon, D. P. DiVincenzo, and K.B. Whaley, Quantum Information and Computation, vol. 1, Rinton Press, New Jersey, 2001, p. 33.

[Kcz04] M. Koniorczyk, P. Rapčan, and V. Bužek, Phys. Rev. A **72** (2004), 022321.

[KM98] T. D. Kühner and H. Monien, Phys. Rev. B **58** (1998), R14741.

[KM04] J.P. Keating and F. Mezzadri, Commun. Math. Phys. **252** (2004), 543.

[KM05] J.P. Keating and F. Mezzadri, Phys. Rev. Lett. **94** (2005), 050501.

[Kor04] V. E. Korepin, Phys. Rev. Lett. **92** (2004), 096402.

[KW02] J. Kempe and K.B. Whaley, Phys. Rev. A **65** (2002), 052330.

[KWM00] T.D. Kühner, S.R. White, and H. Monien, Phys. Rev. B **61** (2000), 12474.

[Laf05] N. Laflorencie, Phys. Rev. B **72** (2005), 140408(R).

[Lan61] R. Landauer, IBM Jl. Res. Develop. **5** (1961), 183.

[LB00] D.P. Landau and K. Binder, *A guide to monte carlo simulations in statistical physics*, Cambridge University Press, 2000.

[LBMW03] D. Leibfried, R. Blatt, C. Monroe, and D. Wineland, Rev. Mod. Phys. **75** (2003), 281.

[LEB04] N. Lambert, C. Emary, and T. Brandes, Phys. Rev. Lett. **92** (2004), 073602.

[Lev04] G. Levine, Phys. Rev. Lett. **93** (2004), 266402.

[LLSHB02] A. Lama-Linares, C. Simon, J.-C. Howell, and D. Bouwmeester, Science **296** (2002), 712.

[LM66] E. Lieb and D.C. Mattis, *Mathematical physics in one dimension: Exactly soluble models of interacting particles*, Academic press, New York, 1966.

[LORV05] J. I. Latorre, R. Orus, E. Rico, and J. Vidal, Phys. Rev. A **71** (2005), 064101.

[LRV04] J I Latorre, E Rico, and G Vidal, Quant. Inf. and Comp. **4** (2004), 048, http://www.arxiv.org/abs/quant-ph/0304098.

[LSC+05] Y. Li, T. Shi, B. Chen, Z. Song, and C. P. Sun, Phys. Rev. A **71** (2005), 022301.

[LSCA05] N. Laflorencie, E. Sorensen, M.-S. Chang, and I. Affleck, http://www.arxiv.org/abs/cond-mat/0512475, 2005.

[LST03] A. Läuchli, G. Schmid, and S. Trebst , http://www.arxiv.org/abs/cond-mat/0311082, 2003.

[Mal03] A. L. Malvezzi, Braz. J. of Phys. **33** (2003), 55.

[MBF03] S. Montangero, G. Benenti, and R. Fazio, Phys. Rev. Lett. **91** (2003), 187901.

[Mes61] A. Messiah, *Quantum mechanics*, vol. 2, North-Holland, Amsterdam, 1961.

[MGW+03] O. Mandel, M. Greiner, A. Widera, Tim Rom, T. W. Hansch, and I. Bloch, Nature **425** (2003), 937.

[MMC+01] O. Morsch, J. H. M´uller, M. Cristiani, D. Ciampini, and E. Arimondo, Phys. Rev. Lett. **87** (2001), 140402.

[MMN05] S. R. Manmana, A. Muramatsu, and R. M. Noack, AIP Conf. Proc. **789** (2005), 269.

[Mon04] S. Montangero, Phys. Rev. A **70** (2004), 032311.

[Moo65] G. E. Moore, Electronics **38** (1965).

[MS77a] F. J. MacWilliams and N. J. A. Sloane, *The theory of error correcting codes*, North-Holland, Amsterdam, 1977.

[MS77b] B. Misra and E.C.G. Sudarshan, J. Math. Phys. **18** (1977), 756.

[MSS01] Yu. Makhlin, G. Schön, and A. Shnirman, Rev. Mod. Phys. **73** (2001), 357.

[MST+04] A. Minguzzi, S. Succi, F. Toschi, M.P. Tosi, and P. Vignolo, Phys. Rep. **395** (2004), 223.

[MV05] S. Montangero and L. Viola , http://www.arxiv.org/abs/quant-ph/0507099, 2005.

[NC00] M. Nielsen and I. Chuang, *Quantum computation and quantum information*, Cambridge University Press, 2000.

[NG99] C.-S. Niu and R.B. Griffiths, Phys. Rev. A **60** (1999), 2764.

[NM05] R. M. Noack and S. R. Manmana, AIP Conf. Proc. **789** (2005), 93.

[NSM02] A. Nazir, T. P. Spiller, and W. J. Munro, Phys. Rev. A **65** (2002), 042303.

[OAFF02] A. Osterloh, Luigi Amico, G. Falci, and R. Fazio, Nature **416** (2002), 608.

[OCJQ05] A. Olaya-Castro, N. F. Johnson, and L. Quiroga, Phys. Rev. Lett. **94** (2005), 110502.

[OL04a] R. Orus and J. I. Latorre, Phys. Rev. A **69** (2004), 052308.

[OL04b] T. J. Osborne and N. Linden, Phys. Rev. A **69** (2004), 052315.

[OLEC05] R. Orus, J. I. Latorre, J. Eisert, and M. Cramer, http://www.arxiv.org/abs/quant-ph/0509023, 2005.

[ON02] T. J. Osborne and M. A. Nielsen, Phys. Rev. A **66** (2002), 032110.

[PEDC05] M.B. Plenio, J. Eisert, J. Dreissig, and M. Cramer, Phys. Rev. Lett. **94** (2005), 060503.

[Per96] A. Peres, Phys. Rev. Lett. **77** (1996), 1413.

[PPKF05] M. Paternostro, G. M. Palma, M. S. Kim, and G. Falci, Phys. Rev. A **71** (2005), 042311.

[Pre98] J. Preskill, *Physics 229: Advanced mathematical methods of physics – quantum computation and information*, http://www.theory.caltech.edu/people/preskill/ph229/.

[Pre00] J. Preskill, J. Mod. Optics **47** (2000), 127.

[PS04] V. Popkov and M. Salerno, Phys. Rev. A **71** (2004), 012301.

[PS05] M. B. Plenio and F. L. Semião, New J. Phys. **7** (2005), 73.

[PSE96] G. M. Palma, K. A. Suominen, and A. K. Ekert, Proc. R. Soc. London **452** (1996), 567.

[PSS+03] D. Pelliccia, V. Schettini, F. Sciarrino, C. Sias, and F. De Martini, Phys. Rev. A **68** (2003), 042306, F. De Martini, D. Pelliccia and F. Sciarrino, Phys. Rev. Lett. **92**, 067901 (2004).

[PSS05] V. Popkov, M. Salerno, and G. Schʹutz, Phys. Rev. A **72** (2005), 032327.

[PVC05] D. Porras, F. Verstraete, and J.I. Cirac , http://www.arxiv.org/abs/cond-mat/0504717, 2005.

[PWKH99] I. Peschel, X. Wang, M. Kaulke, and K. Hallberg (eds.), *Density-matrix renormalization*, Berlin, Springer Verlag, 1999.

[PZ05] I. Peschel and J. Zhao, J. Stat. Mech.: Theor. Exp. (2005), P11002.

[RBH01] J. M. Raimond, M. Brune, and S. Haroche, Rev. Mod. Phys. **73** (2001), 565.

[RCR05] A. Retzker, J. I. Cirac, and B. Reznik, Phys. Rev. Lett. **94** (2005), 050504.

[RFB05] A. Romito, R. Fazio, and C. Bruder, Phys. Rev. B **71** (2005), 100501(R).

[RM04] G. Refael and J. E. Moore, Phys. Rev. Lett. **93** (2004), 260602.

[RVF+04] T. Roscilde, P. Verrucchi, A. Fubini, S. Haas, and V. Tognetti, Phys. Rev. Lett. **93** (2004), 167203.

[RW00] H. Rauch and S. A. Werner, *Neutron interferometry*, Clarendon Press, Oxford, 2000.

[Sac99] S. Sachdev, *Quantum phase transitions*, Cambridge University Press, 1999.

[SC03] A.A. Svidzinsky and S.T. Chui, Phys. Rev. A **68** (2003), 043612.

[Sch98] U. Schollwöck, Phys. Rev. B **58** (1998), 8194.

[Sch05a] U. Schollwöck, Rev. Mod. Phys. **77** (2005), 259.

[Sch05b] U. Schollwöck, J. Phys. Soc. Jpn. **74** (2005), 246.

[SFPS00] J. Siewert, R. Fazio, G.M. Palma, and E. Sciacca, J. Low Temp. Phys. **118** (2000), 795.

[Sho94] P. Shor, Proceedings, 35^{th} Annual Symposium on Foundations of Computer Science, IEEE Press, Los Alamitos, California, 1994, p. 116.

[Sho95] P. Shor, Phys. Rev. A **52** (1995), R2493.

[Sho96] P. Shor, Proceedings, 37^{th} Annual Symposium on Fundamentals of Computer Science, IEEE Press, Los Alamitos, California, 1996, p. 56.

[SIGA05] V. Scarani, S. Iblisdir, N. Gisin, and A. Acín, Rev. Mod. Phys. **77** (2005), 1225.

[Sin00] S. Singh, *The code book*, Anchor Books, 2000.

[SK91] A.W. Sandvik and J. Kurkijärvi, Phys. Rev. B **43** (1991), 5950.

[SKG+98] A. S. Sachrajda, R. Ketzmerick, C. Gould, Y. Feng, P. J. Kelly, A. Delage, and Z. Wasilewski, Phys. Rev. Lett. **80** (1998), 1948.

[SKK99] D.M. Stamper-Kurn and W. Ketterle, Proceedings of Les Houches 1999 Summer School, Session LXXII, 1999, http://www.arxiv.org/abs/cond-mat/0005001.

[SOB+04] R. Somma, G. Ortiz, H. Barnum, E. Knill, and L. Viola, Phys. Rev. A **70** (2004), 0423111.

[SS03] N. Schuch and J. Siewert, Phys. Rev. A **67** (2003), 032301.

[SSL05] A. Sen(De), U. Sen, and M. Lewenstein , http://www.arxiv.org/abs/quant-ph/0505006, 2005.

[Ste96] A. M. Steane, Phys. Rev. Lett. **77** (1996), 793.

[Sub04] V. Subrahmanyan, Phys. Rev. A **69** (2004), 034304.

[Suz76] M. Suzuki, Prog. Theor. Phys. **56** (1976), 1454.

[SW89] A. Shapere and F. Wilczek, *Geometric phases in physics*, World Scientific, Singapore, 1989.

[SZ04] M. Snoek and F. Zhou, Phys. Rev. B **69** (2004), 094410.

[SZQL02] L. Sun, J. Zhang, S. Qin, and Y. Lei, Phys. Rev. B **65** (2002), 132412.

[SZS+02] V. Scarani, M. Ziman, P. Stelmachovic, N. Gisin, and V. Buzek, Phys. Rev. Lett. **88** (2002), 097905.

[TKK04] S. Tsuchiya, S. Kurihara, and T. Kimura, Phys. Rev. A **70** (2004), 043628.

[TRBZ04] L. Tian, P. Rabl, R. Blatt, and P. Zoller, Phys. Rev. Lett. **92** (2004), 247902.

[Tro59] H. F. Trotter, Proc. Am. Math. Soc. **10** (1959), 545.

[VB05] T. Vertesi and E. Bene, http://www.arxiv.org/abs/cond-mat/0503726, 2005.

[VC04] L. M. K. Vandersypen and I. L. Chuang, Rev. Mod. Phys. **76** (2004), 1037.

[vdV02] H.A. van der Vorst, *Computational methods for large eigenvalue problems*, Handbook of Numerical Analysis (P.G. Ciarlet and J.L. Lions, eds.), vol. VIII, North-Holland (Elsevier), Amsterdam, 2002.

[Ved04] V. Vedral, New J. Phys. **6** (2004), 102.

[VEKI93] N. M. Bogoliubov V. E. Korepin and A. G. Izergin, *Quantum inverse scattering method and correlation functions*, Cambridge University Press, 1993.

[Vid03] G. Vidal, Phys. Rev. Lett. **91** (2003), 147902.

[Vid04] G. Vidal, Phys. Rev. Lett. **93** (2004), 040502.

[Vid05] G. Vidal, http://www.arxiv.org/abs/cond-mat/0512165, 2005.

[VL02] L. Viola and S. Lloyd, Phys. Rev. A **58** (2002), 2733.

[VLRK03] G. Vidal, J. I. Latorre, E. Rico, and A. Kitaev, Phys.Rev.Lett. **90** (2003), 227902.

[VMDC04] F. Verstraete, M. A. Martín-Delgado, and J. I. Cirac, Phys. Rev. Lett. **92** (2004), 087201.

[VPC04a] F. Verstraete, M. Popp, and J. I. Cirac, Phys. Rev. Lett. **92** (2004), 027901.

[VPC04b] F. Verstraete, D. Porras, and J. I. Cirac, Phys. Rev. Lett. **93** (2004), 227205.

[VPM04] J. Vidal, G. Palacios, and R. Mosseri, Phys. Rev. A **69** (2004), 022107.

[VW91] J. Vidal and J. Wudka, Phys. Rev. A **44** (1991), 5383.

[WDM+05] T.-C. Wei, D. Das, S. Mukhopadyay, S. Vishveshwara, and P. M. Goldbart, Phys. Rev. A **71** (2005), 060305.

[Wer89] R. Werner, Phys. Rev. A **40** (1989), 4277.

[Wer98a] R. Werner, Phys. Rev. A **58** (1998), 1827.

[Wer98b] R. F. Werner, Phys. Rev. A **58** (1998), 1827.

[WF04] S. R. White and A. E. Feiguin, Phys. Rev. Lett. **93** (2004), 076401.

[WG03] R. S. Whitney and Y. Gefen, Phys. Rev. Lett. **90** (2003), 190402.

[Whi92] S. R. White, Phys. Rev. Lett. **69** (1992), 2863.

[Whi93] S. R. White, Phys. Rev. B **48** (1993), 10345.

[Whi96] S. R. White, Phys. Rev. Lett. **77** (1996), 3633.

[Wil75] K. G. Wilson, Rev. Mod. Phys. **47** (1975), 773.

[WMSG05] R. S. Whitney, Y. Makhlin, A. Shnirman, and Y. Gefen, Phys. Rev. Lett. **94** (2005), 070407.

[Woo98] W. K. Wootters, Phys. Rev. Lett. **80** (1998), 2245.

[WSL04] L.-A. Wu, M. S. Sarandy, and D. A. Lidar, Phys. Rev. Lett. **93** (2004), 250404.

[WZ82] W.K. Wootters and W.H. Zurek, Nature **299** (1982), 802.

[Xia93] Y. Xian, J. Phys. Condens. Matter **5** (1993), 7489.

[YCW03] X. X. Yi, H. T. Cui, and X. G. Wang, Phys. Lett. A **306** (2003), 285.

[Yip03] S.K. Yip, Phys. Rev. Lett. **90** (2003), 250402.

[YLB04] M.-H. Yung, D.W. Leung, and S. Bose, Q. Inf. Comp. **4** (2004), 174.

[ZBFS05] H.-Q. Zhou, T. Barthel, J. O. Fjaerestad, and U. Schollwöck, http://www.arxiv.org/abs/cond-mat/0511732, 2005.

[ZLZ+05] J. Zhang, G. L. Long, W. Zhang, Z. Deng, W. Liu, and Z. Lu, http://www.arxiv.org/abs/quant-ph/0503199, 2005.

[ZPW06] J. Zhao, I. Peschel, and X. Wang, Phys. Rev. B **73** (2006), 024417.

[ZR97] P. Zanardi and M. Rasetti, Phys. Rev. Lett. **79** (1997), 3306.

[ZS03] F. Zhou and M. Snoek, Annals of Physics **308** (2003), 692.

[Zur91] W. H. Zurek, Physics Today **44** (1991), 36.

[ZZHE93] M. Zukowski, A. Zeilinger, M. A. Horne, and A. K. Ekert, Phys. Rev. Lett. **71** (1993), 4287.